POLYPUBLIE

Crystal-Based Modeling of Machining Mechanics for Additively Manufactured Parts

Gabriel Dupoirieux

Document en libre accès dans PolyPublie
Open Access document in PolyPublie

Date	2025
Type	Mémoire ou thèse / Dissertation or Thesis Mémoire de maîtrise/Master's thesis
URL de PolyPublie PolyPublie URL	https://publications.polymtl.ca/68486/
Conditions d'utilisation Terms of use	© Tous droits réservés / All rights reserved
Référence Citation	Dupoirieux, G. (2025). Crystal-Based Modeling of Machining Mechanics for Additively Manufactured Parts [Mémoire de maîtrise, Polytechnique Montréal]. PolyPublie. https://publications.polymtl.ca/68486/

Détails de la thèse
Thesis details

Directeurs de recherche Advisors	Oguzhan Tuysuz
Programme Program	Génie mécanique

Ce fichier a été téléchargé à partir de PolyPublie, le dépôt institutionnel de Polytechnique Montréal
This file has been downloaded from PolyPublie, the institutional repository of Polytechnique Montréal
https://publications.polymtl.ca

POLYTECHNIQUE MONTRÉAL

affiliée à l'Université de Montréal

Crystal-Based Modeling of Machining Mechanics for Additively Manufactured Parts

GABRIEL DUPOIRIEUX

Département de génie mécanique

Mémoire présenté en vue de l'obtention du diplôme de *Maîtrise ès sciences appliquées*

Génie mécanique

Septembre 2025

© Gabriel Dupoirieux, 2025.

POLYTECHNIQUE MONTRÉAL

affiliée à l'Université de Montréal

Ce mémoire intitulé :

Crystal-Based Modeling of Machining Mechanics for Additively Manufactured Parts

présenté par **Gabriel DUPOIRIEUX**

en vue de l'obtention du diplôme de *Maîtrise ès sciences appliquées*

a été dûment accepté par le jury d'examen constitué de :

Aboulfazl SHIRAZI-ADL, président

Oguzhan TUYSUZ, membre et directeur de recherche

Étienne MARTIN, membre

ACKNOWLEDGEMENTS

I would like to express my sincere gratitude to my supervisor, Prof. Oguzhan Tuysuz, for his guidance and advice throughout my research project. I would also like to thank Eralp Demir, PhD for his support and for his clear explanations of crystal plasticity theory, which saved me a great deal of time at the beginning of my master's study.

I would also like to acknowledge Mr. Vincent Mayer, laboratory technician, for his help and the work he has done setting up the machining center and preparing the workpiece each time I needed to perform cutting tests.

I would like to thank my colleague Boris Becker Teukam for the experimental data he collected and shared with me to validate my model.

I would like to thank a lot of my research group colleagues, Mohammadreza, Mama, Jonathan and Julien who brought me motivation and encouragement through the discussions and meals we had together.

I would like to thank my roommates Jules, Gabriel, Elies and David for considering me as their friend as soon as I arrived in Canada.

Finally, I would like to thank my parents, Rachel and Cyriaque, my brother Joseph, and my sister Judith for their unwavering patience and support during the past two years I was away.

RÉSUMÉ

L'usinage de composants fabriqués à partir d'alliages difficiles à usiner est nettement plus coûteux et chronophage que l'usinage des métaux d'ingénierie conventionnels, en raison de délais de fabrication considérablement plus longs. En réponse à cela, les procédés de fabrication additive (AM, *additive manufacturing*) ont été développés pour fabriquer ces matériaux difficiles à usiner sous forme de pièces proches des dimensions finales, réduisant ainsi les délais et les pertes de matière tout en augmentant la productivité. Malgré cette fabrication proche de la forme finale, des opérations de finition par usinage restent indispensables pour satisfaire aux exigences de précision dimensionnelle et de qualité de surface. Le procédé combinant FA et usinage est appelé fabrication hybride. Les changements d'état du métal pendant la fabrication additive entraînent une croissance préférentielle des cristaux, alignés avec le gradient thermique, lui-même aligné avec la direction de construction (BD, *building direction*). Ce phénomène est particulièrement prononcé dans les procédés de dépôt direct d'énergie (DED, *Direct Energy Deposition*), qui produisent des microstructures similaires à celles issues de la solidification lors du soudage. Il en résulte une anisotropie induite par la microstructure dans la pièce finale, contrairement aux métaux forgés classiques qui restent isotropes, avec des grains de formes et d'orientations aléatoires. Ce phénomène conduit à des réponses d'usinage différentes en fonction de l'orientation cristallographique du matériau. Cette recherche vise à prendre en compte l'anisotropie induite par la microstructure dans l'usinage au cours de la fabrication hybride, en développant un modèle analytique et itératif de mécanique de coupe basé sur la plasticité cristalline. L'usinage orthogonal bidimensionnel de monocristaux à structure cubique à faces centrées (FCC, *face-centered cubic*) a d'abord été modélisé à l'aide d'une nouvelle loi d'écrouissage dérivée du modèle constitutif de Johnson-Cook et intégrée à la plasticité cristalline, permettant ainsi de considérer l'effet du taux de déformation de cisaillement et de la température sur l'écrouissage du matériau. Le modèle orthogonal a été validé en comparant les efforts de coupe et les angles de cisaillement prédits avec ceux mesurés expérimentalement lors d'essais de tournage orthogonal sur des monocristaux de cuivre et d'aluminium. Les simulations de tournage sur monocristaux ont montré que l'orientation cristallographique a un impact significatif sur l'amplitude des efforts de coupe. Le modèle développé est également capable de prendre en compte l'influence des paramètres d'usinage tels que la vitesse de coupe, l'épaisseur de copeau non coupé, l'angle de coupe et l'angle de frottement. Le modèle a été étendu à l'usinage oblique tridimensionnel en intégrant l'angle d'inclinaison dans

la géométrie de l'outil et la cinématique d'usinage. Il a également été adapté aux structures cristallines cubique centrée (BCC, *body-centered cubic*) et hexagonale compacte (HCP, hexagonal close-packed) en intégrant les systèmes de glissement correspondants, ce qui permet de simuler des opérations de fraisage industrielles viables et de prendre en compte des matériaux polycristallins via une méthode d'homogénéisation. Des essais de fraisage ont été utilisés pour valider le modèle étendu sur de l'acier inoxydable AISI 316L fabriqué par FA et par forgeage. Les efforts de coupe mesurées se révèlent être 20% plus élevés pour la pièce issue de la FA que pour celle forgée. Une bonne corrélation entre les forces de coupe expérimentales et les forces prédites a été obtenue, avec 15% d'erreur ce qui est acceptable dans le contexte de l'usinage. En conclusion, cette recherche a permis d'établir un modèle fiable de mécanique de coupe fondé sur la théorie de la plasticité cristalline, pouvant être appliqué pour améliorer la qualité de surface, la précision dimensionnelle et la stabilité statique, tout en réduisant les déflexions de l'outil et le risque de rupture de celui-ci lors de l'usinage de pièces issues de la fabrication additive.

ABSTRACT

Machining components made from difficult-to-cut alloys is significantly more costly and time-consuming than machining conventional engineering metals. As a result, additive manufacturing (AM) processes have been used to fabricate these hard-to-machine metals into near-net shape parts, reducing lead time and waste while boosting the productivity. Despite near-net shape fabrication, post-AM machining operations are still essential to satisfy the dimensional accuracy and surface finish demands. The process combining AM and machining is hybrid manufacturing. The changing state of the metal during the AM process causes the crystals to grow in a preferred direction, aligned with the thermal gradient which itself aligns with the building direction (BD). This is particularly evident in Directed Energy Deposition (DED) processes, which produce microstructures similar to those formed during weld solidification. Consequently, a microstructure induced anisotropy is introduced into the final part, while regular wrought metals remain isotropic with grains of random shapes and orientations. This phenomenon leads to different machining responses depending on the crystallographic orientation of the material. This research aims to account for the effect of microstructure induced anisotropy on machining within hybrid manufacturing by developing an analytical crystal plasticity-based cutting mechanics model. To achieve this, crystal plasticity theory has been incorporated into the machining mechanics equations to model cutting behavior in additively manufactured (AMed) materials. The model predicts the direction-dependent cutting force coefficients required to evaluate the machining loads. Two-dimensional (2D) orthogonal machining of face-centered cubic (FCC) single crystals has been first modeled using a newly proposed hardening law derived from the Johnson-Cook material constitutive model. This law has been integrated into the crystal plasticity framework, which allows the consideration of the shear strain rate and temperature effects on material hardening, and in turn, machining mechanics. The tool edge radius geometry is ignored, owing to the assumption of an infinitely sharp tool. The orthogonal model has been experimentally verified by comparing the predicted cutting forces and shear angles against the experimentally measured ones in plunge turning of copper and aluminum single crystals. Turning simulations on single crystals showed that the crystallographic orientation significantly impacts the amplitude of the cutting forces. The developed model is also capable of considering the effects of machining and geometric parameters such as the cutting speed, uncut chip thickness, rake and friction angles values. The model then has been extended to three-dimensional (3D) oblique cutting by incorporating the inclination angle into the tool geometry and

machining kinematics into the mechanics model. It has also been adapted for body-centered cubic (BCC) and hexagonal close-packed (HCP) lattice structures by including the respective slip systems, enabling simulation of industrially-viable milling operations and polycrystal materials through a mean-field based homogenization method. Milling tests have been used to validate the extended model on wrought and Wire Laser Additive Manufactured (WLAM) AISI 316L stainless steel. Cutting forces on the AMed part were measured to be 20% higher than those on its wrought counterpart. A good correlation between the experimental and predicted cutting forces has been found with 15% error, which is acceptable in the machining context. As a result, this research has developed a general cutting mechanics model for digital machining of AMed components grounded in crystal plasticity theory. The introduced model establishes the basis for mechanics-based federate and cycle time optimization in machining of AMed parts and also provides simulation-aided avoidance of excessive tool/part deflections and tool breakage.

TABLE OF CONTENTS

ACKNOWLEDGEMENTS III

RÉSUMÉ IV

ABSTRACT VI

LIST OF TABLES XI

LIST OF FIGURES XII

LISTE OF SYMBOLS AND ABBREVIATIONS XV

CHAPTER 1 INTRODUCTION 1

1.1 Basic concepts of metal cutting process 2

1.2 Research problem and objectives 3

CHAPTER 2 LITERATURE REVIEW 6

2.1 Notions of machining 6

2.1.1 Machining and its industrial significance 6

2.1.2 Machining mechanics modeling 7

2.2 Crystal plasticity basics 13

2.2.1 Lattice structures 14

2.2.2 Miller indices 16

2.2.3 Plastic deformation at the crystal level 19

2.2.4 Machining experiments on single crystals 20

2.2.5 Microstructure-level machining process modeling 23

2.3 Additive manufacturing 28

2.3.1 Classification and characteristics 28

2.3.2 Effect on the microstructure 28

2.3.3 Effect on the machining mechanics 30

2.4 Summary 32

CHAPTER 3 ARTICLE 1: A CRYSTAL PLASTICITY-BASED MODEL FOR ORTHOGONAL MACHINING MECHANICS OF SINGLE CRYSTAL MATERIALS 33

3.1 Abstract 33

3.2 Introduction 34

3.3 Orthogonal machining model 38

3.3.1 Orthogonal cutting 38

3.3.2 Orthogonal turning process 41

3.3.3 Shear strain and shear strain rate 42

3.3.4 Temperature rise in the shear zone 43

3.4 Proposed crystal plasticity-based machining model 44

3.4.1 Deformation kinematics 44

3.4.2 Constitutive law 47

3.5 Experimental verification 49

3.5.1 Crystal plasticity-based machining mechanics model validation 49

3.5.2 Effect of cutting and geometric parameters 55

3.5.3 Crystallographic orientation 58

3.6 Conclusion 61

CHAPTER 4 CRYSTAL-BASED MACHINING MODEL EXTENSIONS 63

4.1 Body-centered cubic (BCC) and hexagonal close-packed (HCP) lattice structures 63

4.2 Flat end-milling process modelling 68

4.2.1 Mechanics of helical end mills 68

4.2.2 Oblique cutting 69

4.2.3 Shear and shear strain rate 72

4.2.4 Temperature rise in the shear zone 74

4.2.5 Macro-scale deformation 74
4.3 Polycrystal materials 74
4.4 Experimental verification 76
4.4.1 Fabrication of the AISI 316L thin-walled part via WLAM 76
4.4.2 Microstructure characterization 77
4.4.3 Machining tests 78
4.5 Results 80
4.5.1 Microstructure analysis 81
4.5.2 Cutting forces 83
4.6 Summary 89
CHAPTER 5 CONCLUSION 91
5.1 Summary and contributions 91
5.2 Model limitations 92
5.3 Future work 93
REFERENCES 95

LIST OF TABLES

Table 2.1 Seven crystal systems and fourteen Bravais lattices 14

Table 3.1 Values of machining parameters in the experiments 49

Table 3.2 Model parameters 50

Table 3.3 Thermal properties of copper 57

Table 3.4 Slip systems for FCC crystals. $n0\alpha$ and $s0\alpha$ are respectively the slip normal and the slip direction of the slip system α in the crystal reference 61

Table 4.1 Deformation modes of BCC lattice structures 64

Table 4.2 Deformation modes of HCP lattice structures 66

Table 4.3 RCC-M code specifications for AISI 316L 77

Table 4.4 Geometric parameters of the tool 78

Table 4.5 Cutting conditions used in the milling tests 79

Table 4.6 Proposed crystal plasticity-based milling mechanics model parameters 83

Table 4.7 Effect of the feed rate on the average cutting forces 88

LIST OF FIGURES

Figure 1.1 Geometry of a. turning process b. milling process. V, h, fc, w and ae are respectively the cutting speed, the uncut chip thickness, the feed rate, the width of cut and the radial depth of cut 3

Figure 2.1 Comparison between machining, forging and casting in terms of dimensional accuracy, roughness, workpiece complexity and mass. 6

Figure 2.2 Illustration of the geometric relations between force components in the tool-workpiece-chip system 9

Figure 2.3 Schematics of three general types of solids 13

Figure 2.4 Crystal lattice and its parameters 14

Figure 2.5 Three common lattice structures (FCC, BCC, HCP) 16

Figure 2.6 Directions in cubic unit cells 17

Figure 2.7 Slip planes in a cubic cell 18

Figure 2.8 Illustration of Miller-Bravais indices on an HCP unit cell 18

Figure 2.9 Slip systems in FCC materials 19

Figure 2.10 (a) Side view of the chip formation in machining of single crystal. (b) Top view of a thick aluminum single crystal chip 20

Figure 2.11 Variation of the shear angle with the rotation angle of a β-brass single crystal orthogonal cutting. The rotation axis corresponds to the 101 crystallographic direction 22

Figure 2.12 (a) zig-zag scanning strategy and (b) cross-hatching strategy. 29

Figure 2.13 Three scanning strategies. 29

Figure 3.1 Representation of an orthogonal cutting process, (a) orthogonal cutting geometry, (b) sample, cutting, and shear frames 39

Figure 3.2 Some crystallographic directions for FCC metals in crystal frame 39

Figure 3.3 Representation of a plunge turning operation around the <010> crystallographic zone axis. $X0, Y0, Z0$ is the sample reference frame and Xc, Yc, Zc is the cutting reference frame. The workpiece rotates around $Y0 = Yc$, aligned with the <010> crystallographic direction41

Figure 3.4 (a) Geometry of the deformation in the shear zone, (b) Shearing geometry. Symbols Δs and Δd are respectively the shear increment and the shear zone thickness 43

Figure 3.5 Comparison of experimentally measured and predicted cutting force coefficients (MPa), (a) Ktc in T1 ($\alpha r = 20°$), (b) Kfc in T1 ($\alpha r = 20°$), (c) Ktc in T2 ($\alpha r = 40°$) and (d) Kfc in T2 ($\alpha r = 40°$) for 010 crystallographic orientation of single crystal copper 52

Figure 3.6 Comparison of experimentally measured and predicted Ktc (MPa), (a) in T3 ($\alpha r = 40°$) and (b) in T4 ($\alpha r = 20°$) for 010 crystallographic orientation of single crystal aluminum. 53

Figure 3.7 Comparison of the predicted and experimentally observed shear angles (°), (a) in T1 ($Cu - \alpha r = 20°$), (b) in T2 ($Cu - \alpha r = 40°$), (c) in T3 ($Al - \alpha r = 40°$) and (d) in T4 ($Al - \alpha r = 50°$) 54

Figure 3.8 Variation of total cutting power with the orientation and shear angles in T2. The solid line shows the minimum total cutting power 55

Figure 3.9 Influence of (a) the rake angle (αr), (b) the friction coefficient (μ), (c) the uncut chip thickness (h), on the tangential cutting force coefficient (Ktc) (MPa) 56

Figure 3.10 Influence of the cutting speed on (a) Ktc (MPa), (b) the temperature (K) in the shear zone 57

Figure 3.11 Influence of the crystallographic orientation on Ktc 58

Figure 3.12 Influence of the crystallographic orientation on the shear angle 59

Figure 3.13 Total number of active slip systems, average cumulative shear and average specific cutting pressure (Ktc) during a full rotation of the cutting tool, with respect to the studied crystallographic zone axes 60

Figure 3.14 Illustration of the 6 slip systems involved when turning around the <110> crystallographic zone axis. Slip systems (a) 3 and 6, (b) 7 and 8, (c) 10 and 11 61

Figure 4.1 Schematic representation of slip systems in BCC crystals 64

Figure 4.2 2D representation of the twinning effect. Lattice configuration, (a) before the shear load is applied, (b) after the shear with two new grain boundaries 65

Figure 4.3 Schematic representation of slip systems in HCP crystals. (a) Basal, (b) Prismatic <a>, (c) Pyramidal <a> and first order Pyramidal <c+a>, (d) second order Pyramidal <c+a> 66

Figure 4.4 Miller-Bravais coordinate system $a1, a2, a3, c$ against cubic coordinate system x', y', z' in an HCP lattice 67

Figure 4.5 Geometry of the milling tool and direction of cutting forces 68

Figure 4.6 Geometry of the oblique (3D) cutting process. 70

Figure 4.7 Geometry of the deformation in the shear zone in oblique cutting 73

Figure 4.8 Illustration of the homogenization method with two EBSD measurements along the axis of the tool 75

Figure 4.9 Illustration of the WLAM process 76

Figure 4.10 Dimensions of the WLAM produced thin-walled plate 77

Figure 4.11 Location of the samples for EBSD analyses in the AMed and wrought parts. Location of the EBSD orientation maps in the samples. BD, TD and SD stand for Building, Transverse and Scanning Direction respectively 78

Figure 4.12 Experimental milling setup 79

Figure 4.13 Illustration of the up-milling configuration of the milling tests 80

Figure 4.14 EBSD analysis of (a) the AMed thin-walled AISI 316L part, and (b) the wrought thin-walled AISI 316L part. (c) the crystallographic orientation IPF color legend. SD and TD respectively stand for scanning direction and transverse direction 82

Figure 4.15 Comparison of the experimentally measured and predicted cutting forces for AMed and wrought AISI 316L in down-milling (T1-T3) 86

Figure 4.16 Comparison of the experimentally measured and predicted cutting forces for AMed and wrought AISI 316L in up-milling (T4 and T5) 87

Figure 4.17 Effect of the helix and rake angles on the predicted cutting forces 89

LISTE OF SYMBOLS AND ABBREVIATIONS

The list of acronyms and abbreviations presents, in alphabetical order, the acronyms and abbreviations used in the thesis and their meaning. Examples:

AM Additive manufacturing

ALE Arbitrary Lagrangian-Eulerian

A Yield stress under quasi-static conditions

α Interaxial angle in a crystal system

α_r Rake angle in orthogonal cutting

α_n Normal rake angle in oblique cutting

a_p Axial depth of cut

a_e Radial depth of cut

A_s Shear plane area

B Hardening modulus

BCC Body-centered cubic

BD Building direction

b Burgers vector

β Interaxial angle in a crystal system

β_a Friction angle (between the tool and the chip)

$\boldsymbol{C}$ Elasticity matrix

C Strain rate coefficient / parameter considering the influence of the cutting conditions

CNC Computer Numerical Control

C_{11}, C_{12}, C_{33} Single crystal elastic constants

c_s Specific heat of the material

c_t Thermal conductivity

D Diameter of the tool

DED Direct Energy Deposition

$\boldsymbol{D}_p$ Plastic strain rate tensor

$d\varepsilon_{VM}$ Equivalent Von-Mises strain increment

$d\gamma^{\alpha}$ Slip increment of the α^{th} slip system

Δd Shear zone thickness

$\Delta\boldsymbol{\varepsilon}$ Total strain increment

$\Delta\boldsymbol{\varepsilon}^e$ Elastic strain increment

$\Delta\boldsymbol{\varepsilon}^p$ Plastic strain increment

ΔF_r, ΔF_t, ΔF_a Radial, tangential and axial force increment

ΔF_x, ΔF_y, ΔF_z Force increment in the global frame

$\Delta\phi$ Angle increment in the engagement zone

Δs Shear increment on the shear plane

Δt Time increment

E Hardening exponent

EBM Electron Beam Melting

EBSD Electron Backscatter Diffraction

ε Total strain

ε^e Elastic part of the total strain

ε^p Plastic part of the total strain

$\dot{\varepsilon}_p$ Plastic strain rate

$\dot{\varepsilon}_0$ Reference strain rate

FE Finite element

$\boldsymbol{F}$ Deformation gradient

$\boldsymbol{F}_i$ Deformation gradient of the i^{th} homogenization volume

$\boldsymbol{F}_{\varphi_{ij}}$ Deformation gradient of the phase φ_{ij}

$\dot{\boldsymbol{F}}$ Derivative of the deformation gradient with respect to the time

F_c Resultant force

F_u Friction force

F_v Normal force acting on the rake face

F_n Normal force acting on the shear plane

FCC Face-centered cubic

F_s Shear force

F_{tc}, F_{fc} Tangential and feed cutting force

F_x, F_y, F_z Force in the global frame

f_c Feed rate

φ_{ij} j^{th} phase of the i^{th} homogenization volume

ϕ_c Shear angle in orthogonal cutting

ϕ_{ex} Exit angle

ϕ_i Oblique shear angle

ϕ_n Normal shear angle

ϕ_p Pitch angle

ϕ_{st} Cutter entry angle

GMAAM Gas Metal Additive Manufacturing

γ Shear on the shear plane / interaxial angle in a crystal system

$\dot{\gamma}$ Shear strain rate on the shear plane

$\dot{\gamma}^{\alpha}$ Slip rate of the slip system α

$\dot{\gamma}_0$ Reference slip rate (flow rule) / Reference shear strain rate (hardening rule)

HCP Hexagonal close-packed

h Uncut chip thickness

h_c Chip thickness

h_0 Reference hardening rate

$\dot{h}^{\beta}$ Single slip hardening rate

η Chip flow angle

i Helix angle

K_{rc}, K_{tc}, K_{ac}, K_{fc} Radial, tangential axial and feed cutting force coefficient

K_{re}, K_{te}, K_{ae} Radial, tangential and axial edge force coefficient

LPBF Laser Powder Bed Fusion

$\boldsymbol{L}$ Velocity gradient

L_c Shear plane length

$\boldsymbol{L}_e$ Elastic part of the velocity gradient

$\boldsymbol{L}_p$ Plastic part of the velocity gradient

λ_h Proportion of plastic work occurring outside the shear zone

λ_s Proportion of heat transferred into the workpiece

M Taylor factor

m Thermal softening coefficient

m_c Material removal rate

μ Friction coefficient

N Number of flutes of the cutting tool

NC Numerical Control

n Spindle rotation speed / slip rate sensitivity parameter / empirical material constant

$\boldsymbol{n}^{\alpha}$ Slip plane normal of the slip system α

PBF	Powder Bed Fusion
q	Latent to self-hardening ratio
$\boldsymbol{R}$	Transformation matrix from crystal reference to shear plane / direction reference
R_T	Nondimensional thermal number
ρ	Density
ϱ_m^α	Mobile dislocation density of the slip system α
SD	Scanning direction
SEM	Scanning Electron Microscope
SLM	Selective Laser Melting
$\boldsymbol{s}^\alpha$	Slip direction of the slip system α
$\boldsymbol{\sigma}$	Stress state on the shear plane
$\boldsymbol{\sigma}_i$	Homogenized Cauchy stress in the i^{th} homogenization volume
$\boldsymbol{\sigma}_{\varphi_{ij}}$	Cauchy stress tensor of the phase φ_{ij}
$\boldsymbol{\sigma}_p$	Plastic stress corrector
$\boldsymbol{\sigma}_{tr}$	Trial stress tensor
σ_y	Yield stress
σ_0	Initial stress state on the shear plane
TD	Transverse direction
T	Temperature / tool life
T_m	Melting temperature
T_r	Room temperature
T_s	Temperature in the shear plane
t_s	Shear time
τ^α	Shear stress on the slip system α

τ_c^α Critical resolved shear stress or slip resistance of the slip system α

τ_c^0 Initial value of the critical resolved shear stress

τ_c^{sat} Saturation value of the critical resolved shear stress

τ_s Shear stress on the shear plane

θ Rotation angle of the tool / immersion angle

θ_n, θ_i Direction angles of the resultant force vector

V Cutting velocity

V_c Chip velocity

V_s Shear velocity

v^α Average glide velocity

v_i i^{th} homogenization volume

$v_{\varphi_{ij}}$ Volume fraction of the phase φ_{ij}

WLAM Wire Laser Additive Manufacturing

w Width of cut

$\boldsymbol{W}_e$ Elastic part of the spin tensor

$\boldsymbol{W}_p$ Plastic part of the spin tensor

$\dot{W}_f$ Friction power

$\dot{W}_s$ Shear power

$\dot{W}_{tot}$ Total cutting power

$\boldsymbol{X}_\alpha^\beta$ Dependency matrix

ψ Lag angle

CHAPTER 1 INTRODUCTION

Achieving high dimensional accuracy and surface quality is essential, particularly in the aerospace [1] industry. These objectives largely depend on the precise control of cutting forces during machining, which is the main manufacturing process used to produce structural and functional aerospace components. Cutting forces govern the mechanical interaction between the tool and the workpiece and directly affect parts' and tools' static deflections, vibrations, surface finish, geometric errors, and tool life. Accurate simulation and prediction of these forces allows engineers to detect and mitigate process abnormalities such as chatter instability, excessive tool wear, and deformation of thin-walled structures in the virtual environment before physical machining. As aerospace components become increasingly complex and performance requirements become more stringent, the ability to model and simulate cutting forces becomes critical for ensuring manufacturing reliability, minimizing costly trials-and-errors, which accelerates digital transformation of manufacturing. This need for precise control over machining forces becomes even more pronounced when machining additively manufactured (AMed) components, whose unique microstructural characteristics pose additional challenges as compared to conventional materials.

Hybrid manufacturing is a fabrication process that combines additive and subtractive manufacturing methods [2]. Additive manufacturing (AM) of metals is capable of building parts with complex geometries while reducing the material waste and lead times [3], especially for the aerospace industry dealing with difficult-to-machine metals such as nickel- and titanium-based superalloys [4]. In addition, AM allows to regroup several manufacturing steps at once, reducing the number of parts and then, assembly time. In most of AM processes, a three-dimensional (3D) computer aided design (CAD) model is used to fabricate the designed workpiece by layer by layer metal deposition [5]. The metal is generally provided in the form of powder or wire and melted using a thermal energy source, typically a laser or electron beam. Industry interest in AM has continued to grow with sales of metal AM systems increasing by 24.4% and rise in the overall valuation of the AM industry by 11.1% between 2022 and 2023, surpassing the $20 billion mark for the first time. [6].

However, additively manufactured (AMed) parts are not directly usable notably in aerospace industry due to their poor surface quality and limited dimensional accuracy. AM, and in particular

DED processes, are constrained by the thickness of the deposited layers, which prevents them from achieving the tight tolerances that are often required in the aerospace industry. Moreover, the layer-by-layer deposition results in wavy surfaces, making post-process machining necessary to improve surface finish and meet the quality standards [7]. Depending on the workpiece material, machining engineers often use conservative tables to choose the appropriate cutting conditions for the post-AM operations. The challenge is that such tables are created for isotropic materials and do not consider the microstructural changes resulting from the metal melting and solidification during AM. In fact, the heat flow generated in AM introduces anisotropy in the part, giving a preferential orientation to the grains [8]. This has a considerable effect on the mechanical properties of the machined part and often leads to excessive tool wear, tool breakage, microstructure-induced vibrations and chatter instability, consequently dramatically deteriorated part quality. Addressing that challenge by developing the mathematical model of the machining mechanics for AMed parts is the core objective of this thesis, allowing the manufacturers to digitally simulate the process ahead of time to ensure dimensional and surface qualities.

1.1 Basic concepts of metal cutting process

Metal cutting is one of the most widely used manufacturing processes for shaping final products. Starting from a bulk raw material, it involves removing excess material in the form of chips to achieve high-quality surfaces with precise dimensions. Figure 1.1 shows the most commonly used metal cutting processes in aerospace part manufacturing, (a) turning and (b) milling, with their respective cutting parameters. Turning is used to create objects with radial symmetry about an axis while milling is better suited to fabricate non-cylindrical, free-form parts. The material removal results from the relative motion between the *cutting tool* and the material, called *workpiece*, while they are in contact. In turning, the interaction between the tool and workpiece comes from both the rotating workpiece and the linearly moving cutting tool along the axis of rotation of the workpiece. In milling, the workpiece can either be fixed or rotate about one or two axes depending on the configuration of the machine. The speed at which the cutting tool passes over the surface of the material being cut is known as the *cutting speed* or *cutting velocity*. (V). The linear distance that the cutting tool travels per minute or per revolution of the spindle is the *feed rate* (f_c). The thickness and width of the layer of material being removed by the cutting tool are called the *uncut chip thickness* (h) and the *width of cut* (w), respectively. In milling, two more parameters are needed to

fully define the cutting geometry: the *axial* (a_p) and *radial* (a_e) *depths of cut* which characterize the tool's engagement along its axis and its engagement with the workpiece in the radial direction, respectively. These parameters are called the *cutting conditions* and are chosen depending on the type of the operation performed (roughing or finishing) and the material to cut. Cutting conditions along with the tool geometry, and work material properties can be used to predict the cutting forces, tool/part deflections, cutting temperature, chip morphology, surface integrity, and vibrations using computational modeling of cutting process, also known as *virtual machining*. This digital approach is central to the goals of *Industry 4.0*, enabling predictive modeling, process automation, and real-time monitoring. The ability to simulate the machining process with high fidelity empowers engineers to reduce lead times, prevent tool breakage, ensure dimensional accuracy especially for critical and high value-added sectors like aerospace. However, most existing models assume isotropic material behavior that does not hold for AMed parts for which anisotropy has a strong influence on cutting mechanics.

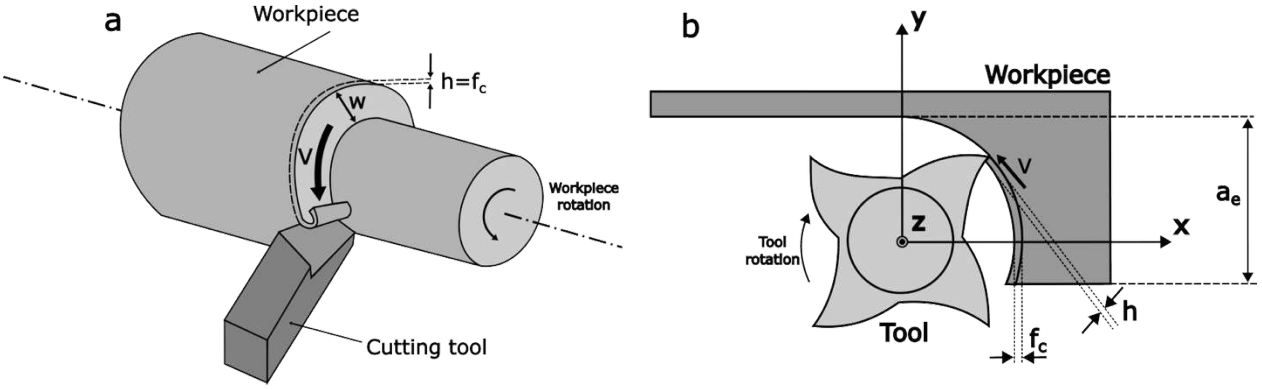


Figure 1.1 Geometry of a. turning process b. milling process. V, h, f_c, w and a_e are respectively the cutting speed, the uncut chip thickness, the feed rate, the width of cut and the radial depth of cut

1.2 Research problem and objectives

Isotropic homogeneous metals have, by definition, the same mechanical properties in every direction. Machining mechanics of these materials, in other words, the cutting forces generated by the process only depend on the cutting tool geometry, material properties of the workpiece, and the cutting conditions chosen by manufacturing engineers. If these three sets of parameters are known, one can predict the material response to machining using mechanistic approaches like Merchant's

theory [9]. However, AMed parts are no longer isotropic and their microstructure, altered by the AM process, contributes to the change in the material behaviour with the cutting direction [10]. Microstructure induced anisotropy is independent of the cutting process and must be predicted to ensure the part quality. The hypothesis of this thesis is that microstructural anisotropy significantly influences the machining mechanics (cutting forces) of AMed parts as compared to their isotropic wrought counterparts. Therefore, the research problem addressed in this thesis can be summarized by the following question: **How can the influence of anisotropic microstructures resulting from AM be accounted for to accurately predict the cutting forces during machining?**

To answer this research question, four research objectives have been established:

1. **Develop a crystal plasticity-based model to predict the cutting forces for FCC single crystal materials.** The first step of this research is to model the effect of crystallographic orientation in two-dimensional (2D) orthogonal machining mechanics for FCC (nickel-based superalloys) single crystal materials. The work material is solid, and its entire structure is composed of a continuous and unbroken lattice with no grain boundaries. As a result, mechanical properties of the workpiece vary significantly with direction and can be observed using the orthogonal turning process, which enables to cut all around the crystal as it rotates with the part. FCC single crystals were initially chosen because experimental cutting forces data is available in literature [11] for the 2D verification of the model.

2. **Extend the model to other lattice structures.** The second step is to expand the model to body-centered cubic (BCC) and hexagonal close-packed (HCP) lattice structures. That plays a crucial role in simulating the machining mechanics of common aerospace alloys such as titanium that is composed of two main phases, BCC and HCP.

3. **Develop three-dimensional (3D) oblique cutting mechanics model.** Most of the practical post-AM machining operations are milling as it allows to create complex free-form geometries. Hence, the third objective is to integrate the milling kinematics into the developed 2D model for cutting force prediction in single crystal machining. That has been achieved by incorporating the inclination angle between the cutting edge and the cutting speed direction. The helical cutting edges of the milling tool are axially discretized in infinitesimal oblique cutting processes.

4. Extend the model to polycrystals. The final objective aims at adapting the model to polycrystals. Even though single crystals are the ideal materials to study the effect of microstructure anisotropy on cutting forces, almost all metals are polycrystals and composed of several grains oriented in different directions. That has been addressed by integrating a homogenization method into the proposed 3D machining mechanics model to consider the crystallographic orientation effect on the cutting forces for each grain.

CHAPTER 2 LITERATURE REVIEW

The three main fields involved in this research project are **machining**, **crystal plasticity,** and **additive manufacturing**, particularly **DED** processes. This chapter will provide an overview of each of them and explain how they are related and used together in the proposed force prediction model. The basic concepts and the terminology will be developed.

2.1 Notions of machining

2.1.1 Machining and its industrial significance

Machining is the name of a subtractive manufacturing process family using controlled material removal to create the design geometry from an initial raw material. It includes processes like turning, milling, boring, drilling, and grinding. As mentioned in Section 1.1 the unnecessary material is removed as chips, which allows to meet tight dimensional tolerances. For example, mechanical machining remains today the most reliable and cheapest method to create micro-structured surfaces using the ultra-precision diamond sculpturing methods with a form error of 70 nm [12-14]. Machining processes are also used to create components for industries such as aerospace [1], automotive [15] and biomedical [16] with the possibility to produce complex-shaped parts with high precision, which is not always possible with other widespread manufacturing methods such as forging and casting. Figure 2.1 positions machining according to the dimensional accuracy, roughness, workpiece complexity and mass with casting and forging.

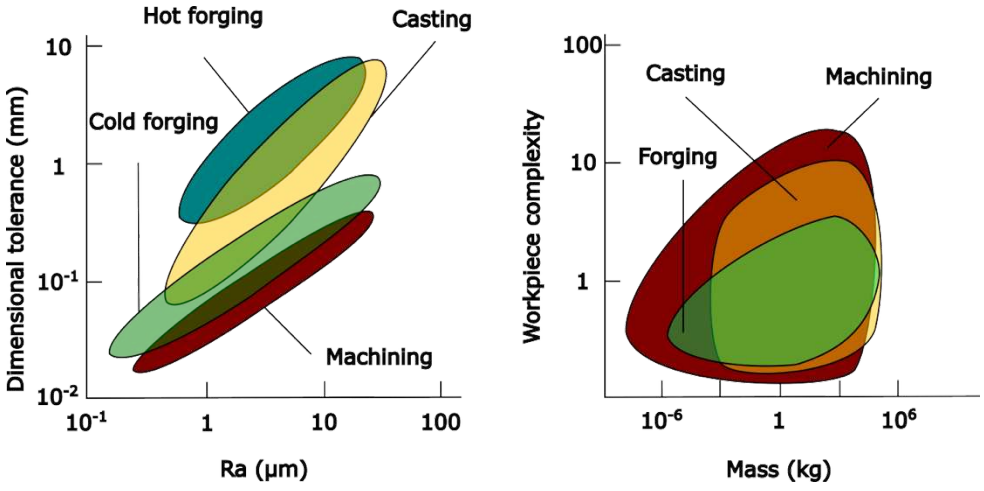


Figure 2.1 Comparison between machining, forging and casting in terms of dimensional accuracy, roughness, workpiece complexity and mass. Reproduced from [17]

Merchant [18] reported that machining contributes around 15% of the global value of manufactured mechanical components. In the US, machining amounts to approximately $154 billion annually with 75% of this attributed to milling, turning, drilling and grinding [19]. These facts highlight the importance of machining as a manufacturing process and its economic significance in every industry. A deep understanding of the fundamentals of metal cutting processes is necessary to keep improving machining methods, to create products with a better quality at lower costs, machine new materials coming from various manufacturing methods like AM or single crystal parts in order to obtain higher mechanical properties.

2.1.2 Machining mechanics modeling

Machining process modeling has progressed through three major stages: empirical modeling, predictive modeling based on scientific principles, and numerical modeling [18]. All three methods are currently used in parallel, enhancing and supporting each other.

Empirical modeling

Prior to the 1900s, modeling of machining process was limited to what was experimentally observed to be the most efficient cutting parameters depending on the work material used and geometry. The first researcher who tried to understand the effect of cutting parameters (cutting speed, feed rate, cutting tool geometry etc.) on the machining process was F.W. Taylor. He notably derived a tool wear prediction equation that is still used today [20],

$$VT^n = C \tag{2.1}$$

where V is the cutting speed in m/min, T is the tool life in min, n is an empirical material constant and C is a parameter considering the influence of the cutting conditions on the tool life. While Taylor's work laid the foundation for empirical modeling of machining processes, particularly tool wear, it also indirectly highlighted the importance of understanding the mechanical interactions between the tool and the workpiece. In fact, tool wear directly affects the cutting forces, heat generation, and chip formation, which are all governed by the mechanics of machining. As machining research progressed, it became increasingly clear that to predict and control the process states such as cutting forces, tool deflections, and surface integrity, more physics-based machining mechanics models were needed, beyond purely empirical relationships.

Physics-based modeling

In the 1940's, Ernst and Merchant [21] modeled orthogonal cutting mechanics, while the cutting edge being perpendicular to the cutting velocity direction. The mechanism by which the material was removed in chip form was investigated through a microscope during cutting [22], and the notion of *shear plane* was introduced and considered as the starting point of the chip generation. The *shear plane*, where the plastic deformation occurs during cutting, is a narrow band between the workpiece and the chip. The shearing process had already been observed earlier by Piispanen [23] who stated this phenomenon was like cutting a deck of stack cards. The cards are inclined at an angle ϕ_c from the horizontal, which is called the *shear angle*. Then, Merchant kept studying chip formation mechanism and thought that the chip itself could be considered as a body being part of the tool – workpiece – chip system on which continuum mechanics could be applied. The outcome was a set of geometric relations (Figure 2.2) that constitutes the fundamentals of science-based predictive modeling of orthogonal machining, which is still widely used today [9]. In Figure 2.2, h and h_c are respectively the *uncut* and *cut chip thicknesses*, α_r and β_a are the *rake* and *friction angles*, F_c, F_u, F_v, F_s, F_{tc}, F_{fc} and F_n are respectively the *resultant force*, *friction force*, *normal force* acting on the *rake face* of the tool, *shear force*, *tangential force*, *feed force* and *normal force* acting on the *shear plane*.

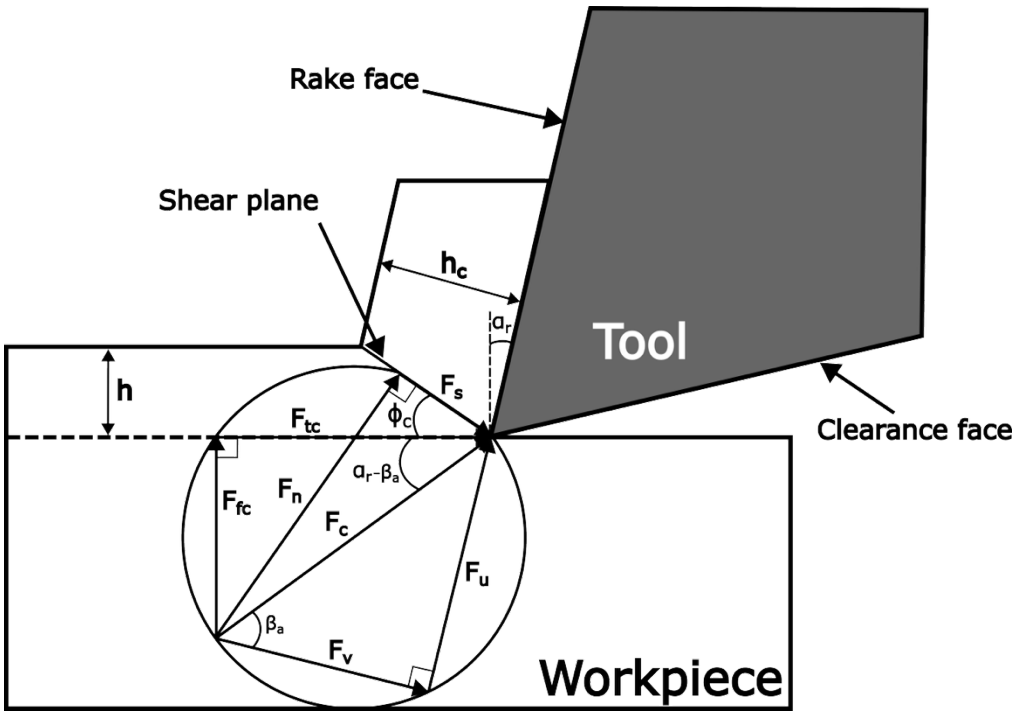


Figure 2.2 Illustration of the geometric relations between force components in the tool-workpiece-chip system

The predictive machining model derived by Merchant relies on the following assumptions:

(1) The cutting edge of the tool is perfectly sharp and there is no contact between the clearance face and the machined surface.

(2) The shear zone is either a plane or a band with a very thin thickness.

(3) The machining geometry must be orthogonal cutting.

The tangential and feed forces expressions according to Merchant's geometric relations are [9],

$$F_{tc} = hw\left[\frac{\cos(\beta_a - \alpha_r)}{\cos(\phi_c + \beta_a - \alpha_r)}\,\tau_s\right] \tag{2.2}$$

$$F_{fc} = hw\left[\frac{\sin(\beta_a - \alpha_r)}{\cos(\phi_c + \beta_a - \alpha_r)}\,\tau_s\right] \tag{2.3}$$

where τ_s is the shear stress in the shear plane. Merchant [9] also attempted to predict the shear angle by linking it to the rake and friction angles. He proposed that the cut chip thickness h_c adjusts to a value that minimizes the cutting power, which gives the shear angle as:

$$\phi_c = \frac{\pi}{4} - \frac{\beta_a - \alpha_r}{2} \tag{2.4}$$

Lee and Shaffer [24] proposed their predictive orthogonal machining mechanics model considering a thick shear zone on which they applied continuum plasticity theory. Therefore, they introduced a fictitious plastic field delimitating the shear zone, in which the shear occurs through a single slip line. The tangential and feed force components are expressed as [24],

$$F_{tc} = \tau_s hw \left[1 + \cot\left(\frac{\pi}{4} - \beta_a + \alpha_r\right)\right] \tag{2.4}$$

$$F_{fc} = \tau_s hw \left[\cot\left(\frac{\pi}{4} - \beta_a + \alpha_r\right) - 1\right] \tag{2.5}$$

For the shear angle prediction, it was assumed [24] that the shear occurs in the direction of the maximum shear stress, and shear angle becomes:

$$\phi_c = \frac{\pi}{4} - (\beta_a - \alpha_r) \tag{2.6}$$

The same relation (Eq. (2.6)) has been derived by Krystof [25] based on the maximum shear stress principle. However, neither equations Eq. (2.4) nor Eq. (2.6) are supported by experiments. Each predicts a universal relationship between ϕ_c, α_r and β_a with Merchant's equation predicting larger shear angles than [24] for the same rake and friction angles, but such relations are not observed in practice [26]. Zorev [27] considered a pie-shaped shear deformation zone where the material flows along curved streamlines. The non-uniform nature of plastic deformation during machining was captured unlike Lee and Shaffer [24], who considered a uniform distribution of the shear stress in the shear deformation zone. Palmer and Oxley [28] also considered a thick shear deformation zone to develop their predictive machining mechanics model but they incorporated strain hardening, strain rate sensitivity, and temperature effects. They observed a shear strain rate distribution, leading to variations of the shear stress in the shear deformation zone.

Although slip-line field models [24, 27, 28] may better represent the plastic deformation mechanics behind the shearing process in metal cutting, they assume an isotropic state of the material and do not naturally account for crystallographic effects. On the contrary, Merchant's theory offers a straightforward analytical orthogonal machining model based on force equilibrium and minimum cutting power principle making it more suitable for integrating the crystal plasticity equations to consider the microstructure induced anisotropy of AMed parts.

Two-dimensional orthogonal cutting is an appropriate machining geometry for understanding the fundamental physical phenomena in metal cutting. However, since most practical machining operations are oblique (three-dimensional) a comprehensive extension to such conditions is essential to fully leverage the benefits of modeling.

Merchant [9] generalized the geometric equations of 2D orthogonal cutting to predict the 3D oblique cutting mechanics. In oblique machining, the cutting edge of the tool is no longer perpendicular to the cutting speed direction, but an *inclination angle* (i) between the cutting edge normal in the cutting plane and the direction of relative motion between tool and workpiece is considered. Altintas [29] derived a set of geometric equations (presented in Section 4.2.2) between five cutting parameters specific to oblique cutting: *chip flow angle* (η), *normal shear angle* (ϕ_n) *oblique shear angle* (ϕ_i), and the *direction angles of the resultant force* (θ_n, θ_i). Values of these parameters can be solved iteratively by applying the maximum shear stress principle as used for orthogonal cutting [24, 25] to oblique cutting [30] by initially considering that $\eta = i$ as proposed by Stabler [31]. The minimum energy principle [9] can also be used in oblique cutting to determine both the normal ϕ_n and oblique ϕ_i shear angles by power minimization, and it is considered in this thesis for both 2D orthogonal and 3D oblique cutting mechanics modeling.

Armarego and Whitfield [32] developed an empirical orthogonal to oblique transformation model allowing to use the material's shear stress, friction coefficient, and shear angle determined through orthogonal cutting tests or databases and then adapted it to oblique cutting using the geometry of the cutting tool [33]. However, this method is not well suited for anisotropic materials since an unmanageable number of orthogonal cutting tests would be necessary to accurately transform the orthogonal cutting mechanics to the oblique one.

Numerical modeling

The advent of digital computer technology opened a new dimension to the modeling of machining operations. Finite element (FE) methods have started to be used by Strenkowski and Carroll [34] to simulate orthogonal cutting operations to predict the chip geometry, the residual stress in the workpiece, the tool stresses and the cutting forces. This type of modeling method then became very popular in the field of machining, being used to simulate turning [35-37], milling [38-40] and almost all the other metal cutting processes. The shear zone is among the most critical regions in FE metal cutting simulations. High shear strain and shear strain rate in the cutting process cause

severe mesh distortion and may result in computational issues such as convergence rate and numerical errors [41]. To apply FE methods to machining simulations and cope with the process induced computational difficulties, three main FE formulations have been developed: Lagrangian, Eulerian, Arbitrary Lagrangian-Eulerian (ALE). The Lagrangian formulation is commonly used in solid mechanics and metal cutting simulations. In this approach, the mesh moves with the material, making it useful for modeling how metal flows and chips form during cutting. It allows the chip shape to develop naturally without knowing it in advance, and it can also simulate chip breaking. However, because the material undergoes large deformation, the mesh can become distorted, requiring remeshing [42-44] which means updating the mesh during the solution process to reduce distortion [45]. Another solution to overcome distortion problem is to use a pre-distorted mesh [46, 47]. In the Eulerian formulation, the mesh stays fixed, and the material flows through it. This avoids mesh distortion and uses fewer elements, making simulations faster. However, the chip shape and boundaries must be known before the simulation, and certain values like chip thickness and tool-chip contact must stay constant, which doesn't fully reflect real cutting conditions. Raczy *et al.* [48] simulated an orthogonal cutting operation on copper and predicted the stress and strain distribution in the shear zone using the Eulerian formulation. The Arbitrary Lagrangian-Eulerian (ALE) method combines the best parts of both Lagrangian and Eulerian approaches. In ALE, the mesh moves independently from the material. The model uses the Lagrangian method to track material movement and the Eulerian method to update the mesh. This helps avoid mesh distortion near the cutting tool without remeshing, while still allowing the chip to form naturally based on material deformation. Olovson *et al.* [49] developed a 2D finite element machining model based on the ALE formulation to simulate the material fracture during cutting. Movahhedy *et al.* [50] presented a sample cutting model based on the ALE formulation to showcase the method's capabilities and potential. They concluded that ALE is highly efficient because it does not require a node separation criterion, allows for natural chip formation, eliminates the need for iterative boundary adjustments, and does not demand a highly refined mesh around the tool tip. Ozel and Zeren [51] used the ALE formulation to simulate an orthogonal cutting operation of AISI 4340 steel to study the effect of the tool edge radius on the stress and temperature of the workpiece, which they found to be significant.

Since FE methods are very computationally demanding compared to analytical physics-based models which doesn't require complex meshing strategies and are specifically derived for

machining process, no finite element (FE) methods will be used in this thesis. Analytical methods are already accurate, computationally more efficient, and independent of the workpiece geometry.

2.2 Crystal plasticity basics

In a crystalline solid, each atom occupies a well-defined position in space, not only relative to its nearest neighbors, but also in relation to all other atoms, regardless of the distance separating them [52]. An important consequence of the regular arrangement of atoms in crystalline solids is *anisotropy* and it is reflected in many types of material properties such as mechanics, magnetism, electrical conductivity, etc. The classification of solid materials commonly includes three major types: amorphous, polycrystals, and single crystals [53] as shown in Figure 2.3. Amorphous materials are non-crystalline solids that lack the long-range order in atoms position described above [54]. Polycrystals are crystalline solids composed of several *grains* separated by *grain boundaries*. One grain is characterized by a unique crystalline structure, and the *grain boundary* marks a change in this structure in the material. Finally, single crystal materials are ideally composed of a single *grain*, with no *grain boundary*, and consequently a unique crystal structure. In this thesis, machining operations on single crystals will first be considered to fundamentally understand the effect of crystal orientation on cutting forces, and then the case of polycrystals will be treated with AMed parts machining.

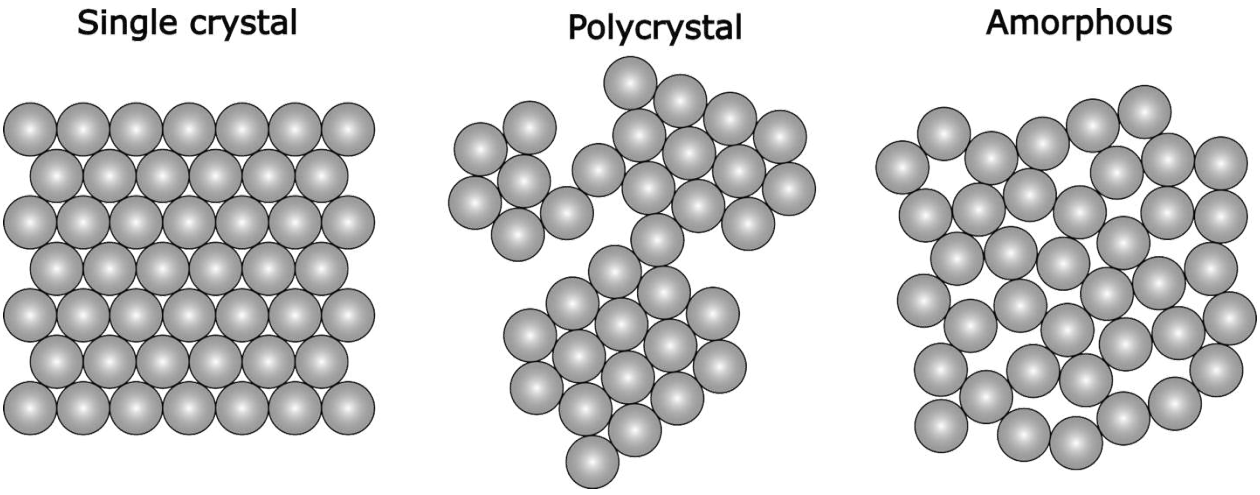


Figure 2.3 Schematics of three general types of solids

2.2.1 Lattice structures

A crystalline structure is composed of atoms or molecules organized in a repeating pattern that extends in all three spatial dimensions. The smallest repeating unit of this structure is called *unit cell*. The geometry of the crystal *lattice* is fully defined by its *lattice* parameters — the edge lengths a, b, and c, along with the interaxial angles α, β, and γ [55] as shown in Figure 2.4.

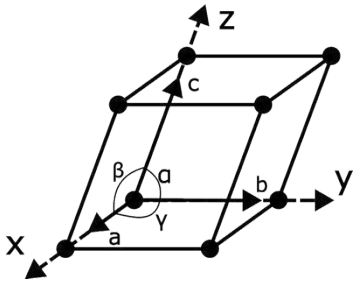
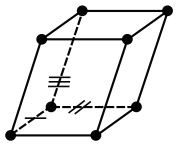
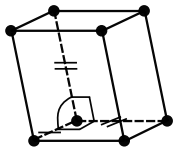
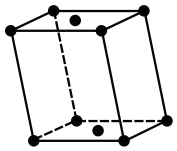
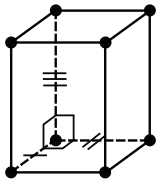
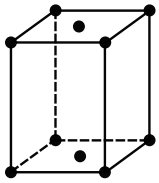
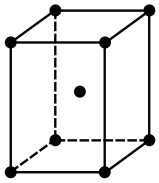
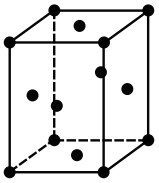
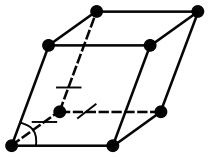
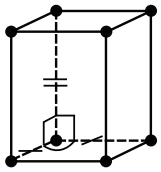
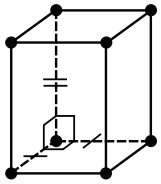
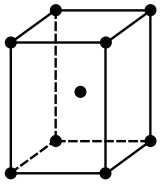
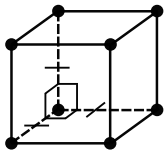
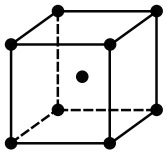
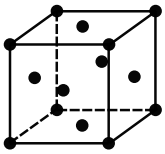


Figure 2.4 Crystal lattice and its parameters

Depending on the relations between the three vectors a, b, and c, and the three angles α, β, and γ, seven different crystal systems can be distinguished. These seven crystal systems can form 14 different arrangements called *Bravais lattices* (Table 2.1).

Table 2.1 Seven crystal systems and fourteen Bravais lattices [52]

Crystal system	Edge length	Interaxial angle	Bravais lattice			
			Simple	Base-centered	Body-centered	Face-centered
Triclinic	$a \neq b \neq c$	$\alpha \neq \beta \neq \gamma \neq 90°$				
Monoclinic	$a \neq b \neq c$	$\alpha = \gamma = 90° \neq \beta$				

Orthorhombic	$a \neq b \neq c$	$\alpha = \beta = \gamma = 90°$				
Rhombohedral	$a = b = c$	$\alpha = \beta = \gamma \neq 90°$				
Hexagonal	$a = b \neq c$	$\alpha = \beta = 90°$ $\gamma = 120°$				
Tetragonal	$a = b \neq c$	$\alpha = \beta = \gamma = 90°$				
Cubic	$a = b = c$	$\alpha = \beta = \gamma = 90°$				

Among all the lattice configurations presented above, three are particularly common in metals: face-centered cubic (FCC), body-centered cubic (BCC) and hexagonal close-packed (HCP). In this thesis, copper, aluminum, and austenitic stainless steel are studied, which all have an FCC lattice structure, but the proposed model can also handle BCC and HCP to simulate cutting operations on titanium alloys, whose main phases are composed of these two lattice types. In an FCC lattice structure, atoms are arranged such that there is one atom at each corner of the cube and one atom at the center of each of the six faces as shown in Figure 2.5. Each corner atom is shared among eight neighboring unit cells, while each face-centered atom is shared between two. This arrangement results in four atoms per unit cell and a high packing efficiency of about 74%, making FCC one of the most densely packed crystal structures.

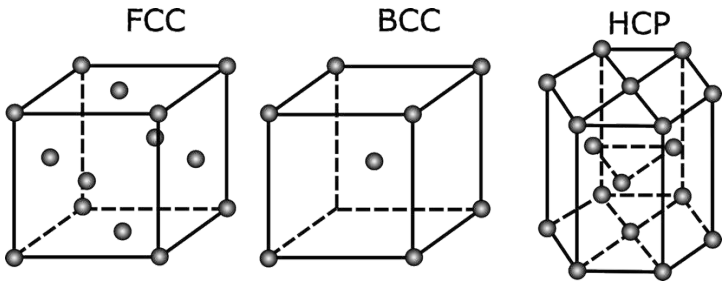


Figure 2.5 Three common lattice structures (FCC, BCC, HCP)

2.2.2 Miller indices

At the crystal level, a specific coordinate system called the Miller indices is used to describe directions and planes. It is based on three directional vectors a, b, and c that define the lattice structure. The origin of the coordinate system is arbitrarily placed at one of the lattice nodes, since all nodes are geometrically equivalent [56]. A node is an abstract point to which an atom or group of atoms may be associated. These indices will be used in the rest of the thesis to describe the microstructure and dislocation movements of the crystal during plastic deformation.

Direction indices

A crystallographic direction is defined with three indices $[uvw]$. It is the direction of a line starting from the origin and passing through the points of coordinates u, v and w. To simplify the writing, u, v and w are integers with no common denominator. For example, the line passing through the points of coordinates 4, 4, 2 also passes through the point 2, 2, 1 and its direction is $[221]$. To use negative indices, the convention rule is to put a negative sign on top them, for instance $[22\bar{1}]$. Depending on the crystal system considered, some directions are equivalent and a permutation of the indices u, v and w does not change the characteristics of the direction. These directions are part of the *family of directions* $\langle uvw \rangle$. For example, in the cubic crystal system, since $a = b = c$, the directions $[100]$, $[010]$ and $[001]$ are equivalent and form the family of directions $\langle 100 \rangle$. Another example, directions $[221]$, $[212]$, $[122]$, $[\bar{2}21]$, $[\bar{2}12]$, $[\bar{1}22]$, $[2\bar{2}1]$, $[2\bar{1}2]$, $[1\bar{2}2]$, $[22\bar{1}]$, $[21\bar{2}]$ and $[12\bar{2}]$ form the family $\langle 221 \rangle$. Figure 2.6 shows three crystallographic orientation examples.

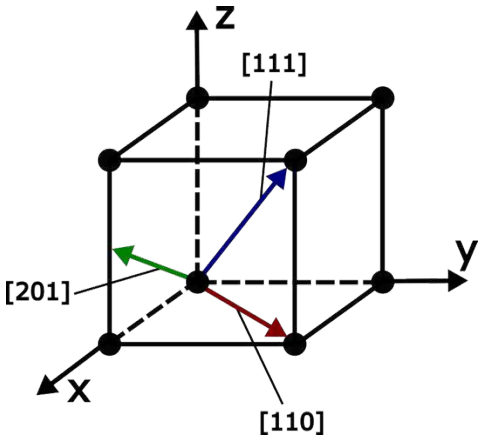


Figure 2.6 Directions in cubic unit cells

Plane indices

A plane is entirely defined by its normal vector, and this is how to refer to a plane at the crystal level. An easy method to determine the normal vector of a plane in a cubic unit cell is to follow these steps:

1. Take the fractional lengths at which the plane intersects the crystallographic axes.
2. Take the reciprocal of the fractions.
3. Put all the fractions to the smallest same common denominator.
4. Only keep the numerators.

For example, if a plane intersects the crystallographic axes at points 1/1, 1/2 and 1/1, the reciprocals are 1/1, 2/1 and 1/1. The smallest same common denominator is 1 therefore the fractions remain identical. Then the plane normal is (121). Figure 2.7 shows some planes in their Miller indices notation.

As for direction indices, a family of plane is mentioned as $\{100\}$ as a convention.

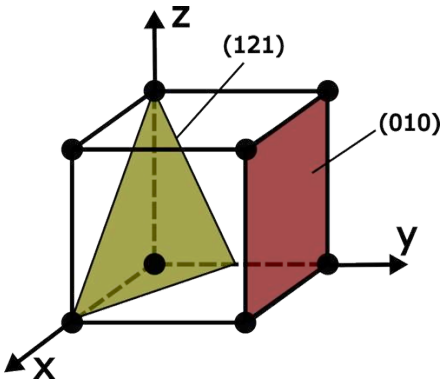


Figure 2.7 Slip planes in a cubic cell

Hexagonal structure

A different coordinate system is used to refer to planes and directions in HCP structures. This coordinate system is called *Miller-Bravais indices* and is based on four axes a_1, a_2, a_3 and c represented in Figure 2.8. a_1, a_2, a_3 are coplanar and form 120° angle between each other whereas c is normal to the plane containing them. Plane indices are written $(hkil)$ and are obtained the same way as Miller indices. Since a_1, a_2, a_3 are coplanar and since a plane is fully defined with only two vectors, h, k and i are not independent and the third index is derived according to the following relation $i = -(h + k)$.

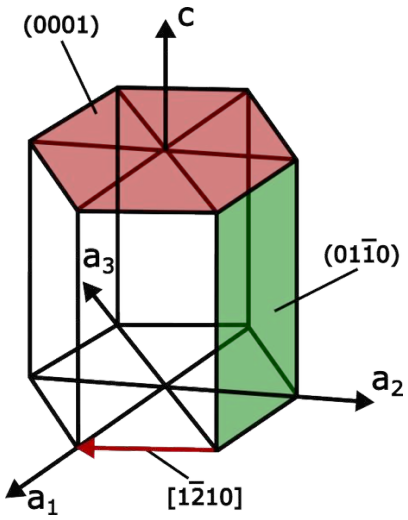


Figure 2.8 Illustration of Miller-Bravais indices on an HCP unit cell

2.2.3 Plastic deformation at the crystal level

For most metals and alloys undergoing a tensile test, the stress-strain curve shows an elastic-plastic transition in between the elastic and plastic zones. This transition zone is characterized by the yield stress σ_y. If the external load on the material remains below σ_y, deformation occurs in the elastic domain, and the material is in an unstable state: as soon as the mechanical constraint is removed, the material turns back to its original shape. When the imposed loading becomes greater than σ_y, the material deforms plastically and does not recover its original shape once the constraint is removed because it reached a new stable state. This permanent deformation occurs through crystallographic slip, where atoms in the most densely packed planes slide along the most closely packed directions [52]. This phenomenon is called *dislocation*. The atoms move on specific planes called *slip planes* and along specific directions on these planes called *slip directions*. The combination of a slip plane and a slip direction forms a *slip system*.

In FCC materials, for example, there are 12 different slip systems available as illustrated in Figure 2.9.

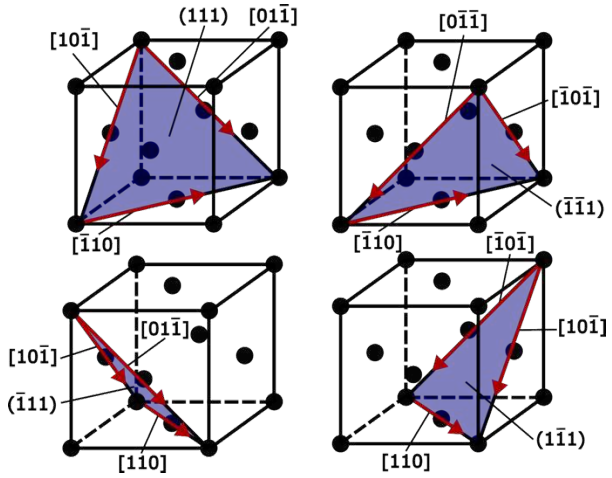


Figure 2.9 Slip systems in FCC materials

For a slip system to be activated, the shear stress on that plane along the shear direction, called *resolved shear* stress, must be greater than the slip resistance of that slip system, also referred as *critical resolved shear stress* (CRSS). Generally, the material accommodates the plastic deformation owing to the activation of a combination of different slip systems. However, depending on the crystal orientation and the loading direction, different sets of slip system might

activate, leading to high fluctuations of the mechanical response of the material to the external loading. This particularly applies on machining and especially on turning, where the workpiece rotates with respect to the tool and exhibits different crystal orientation. In the next section, some machining experiments on single crystals are presented.

2.2.4 Machining experiments on single crystals

Single crystal materials are ideal for studying the effect of crystallographic orientation on the machining mechanics because they have no grain boundaries and possess a unique crystallographic orientation. In addition, the microelectronics industry heavily relies on single crystal semiconductor materials that are micro-machined and motivates the researchers to investigate their mechanical behaviour at the crystal level during machining. Single crystals are produced using crystal growth methods, which generally consist of melting the material and resolidifying it by varying the temperature field [57-59]. Starting from the 1970's, several researchers experimentally observed the crystallographic orientation effect on the machining response using single crystal copper and aluminum. Von Turkovich and Black [60] examined very early process of chip formation in single crystal copper and aluminum, performing cutting tests at depths of cut ranging from 1 to 100μm inside a scanning electron microscope (SEM). They were able to capture the shear deformation at a very low cutting speed, observing a thin band (shear plane), where intense deformation takes place, as shown in Figure 2.10.

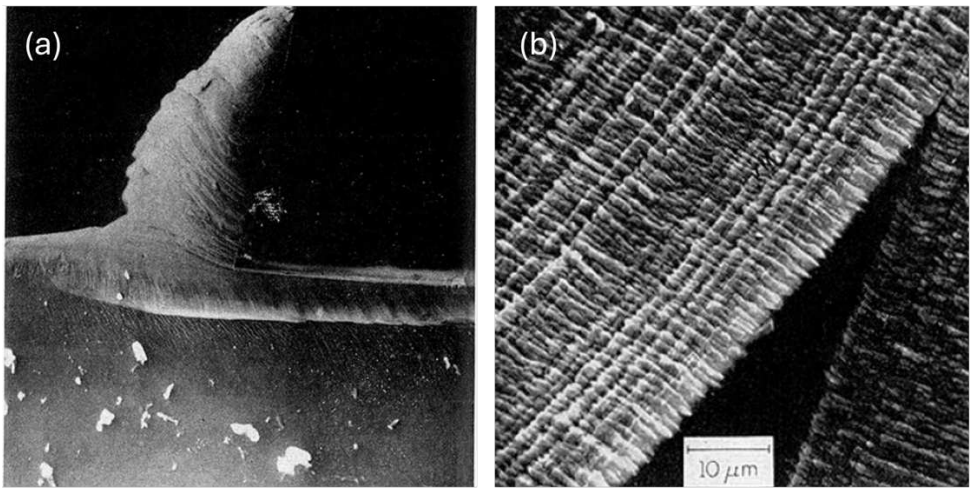


Figure 2.10 (a) Side view of the chip formation in machining of single crystal. (b) Top view of a thick aluminum single crystal chip [60]

Ramalingam and Hazra [61] found that the *dynamic shear stress* remains constant for all orientations when single crystals of aluminum are machined and matches the predicted values for polycrystalline aluminum. As a result, they stated that the dynamic shear stress can be considered as a true material property, and its calculation, derived by von Turkovich [62], relies on the physical process of dislocations at the crystal level. Williams and Gane [63] performed orthogonal cutting tests on polycrystalline copper, gold, aluminum, iron, magnesium, zinc, titanium and had the same conclusion. They also machined a single crystal copper and noticed that the chip formation was easier when the {111} slip planes were parallel to the shear plane with a shear stress 40% lower than when they were parallel to the cutting direction.

The chip morphology in machining has attracted researchers' attention since it is related to the cutting forces and the machined surface quality. The ratio between the uncut chip thickness and the effective cutting edge radius of the tool plays a critical role in both isotropic and anisotropic cutting processes. In micromachining, where the uncut chip thickness is generally less than 200 μm [64], the tool edge radius frequently approaches the same order of magnitude. A small ratio of the uncut chip thickness to the tool edge radius is the cause of *size effect*, a phenomenon characterized by an increase of the cutting forces when the uncut chip thickness decreases. Consequently, the material removal process highly depends on the uncut chip thickness as a small change in its value can lead to the suppression of the chip formation, with all the material ploughed under the tool cutting edge, producing a poor surface quality. The notion of *minimum chip thickness* which characterizes the minimum depth of cut below which no chip will be formed has been investigated by researchers [65, 66]. In addition, at such a small scale, the effect of crystallographic orientation on the cutting mechanism becomes non-negligible and changes markedly from conventional machining when the tool size or the feature scale approaches the material's grain size [67]. Vogler *et al.* [68, 69] examined how the microstructure of single- and multi-phase irons influences surface generation and cutting forces in micro-end milling. They used endmills of 508 μm diameter with edge radii of 2 and 5 μm. They reported that a fragmented chip led to a poor surface quality especially when the tool cuts through different phases. Also, it was confirmed that the tool edge radius has a significant impact on surface formation, primarily due to the existence of a minimum chip thickness, particularly in single-phase materials. Lucca *et al.* [70, 71] used a single crystal diamond tool to study the effect of the tool edge geometry on the cutting forces and specific cutting energy in an ultraprecision orthogonal fly cutting operation on copper. The rake angle and tool

edge radius were found to have a significant effect on the *specific cutting energy*. Uncut chip thicknesses ranging from 20 to 10 μm were investigated and a drastic increase of the specific cutting energy which could not be explained by the shearing process alone has been revealed. Furukawa and Moronuki [72] proved that the cutting mechanism differs a lot when micromachining polycrystals, single crystals or amorphous materials. According to their results on pure copper, aluminum and germanium alloys, the cutting forces increase exponentially when the uncut chip thickness decreases below $3\mu m$. They also found that when cutting single-crystal fluorite and amorphous acrylic, the cutting forces were more consistent due to the absence of grain boundaries, which is the primary source of cutting force fluctuations in the machining of polycrystals. To avoid the crystallographic effect of grains, they recommend using a depth of cut about ten times larger than the grain size.

Variation in the chip formation with crystallographic orientation is also observed in macro machining, when cutting single crystal materials even though the size effect is no longer present. This could be achieved in machining single crystal turbine blades or silicon wafers [73]. The chip generation has been studied by Ueda *et al.* [74] in orthogonal cutting of single crystal β-brass. They showed that depending on the cutting direction, the pattern of chip generation was changing, with continuous or discontinuous chips and varying shear angles between 15° and 60° as shown in Figure 2.11. A lamellar structure has been observed in the shear zone through scanning electron microscopy (SEM), starting from the tool tip and propagating through the material.

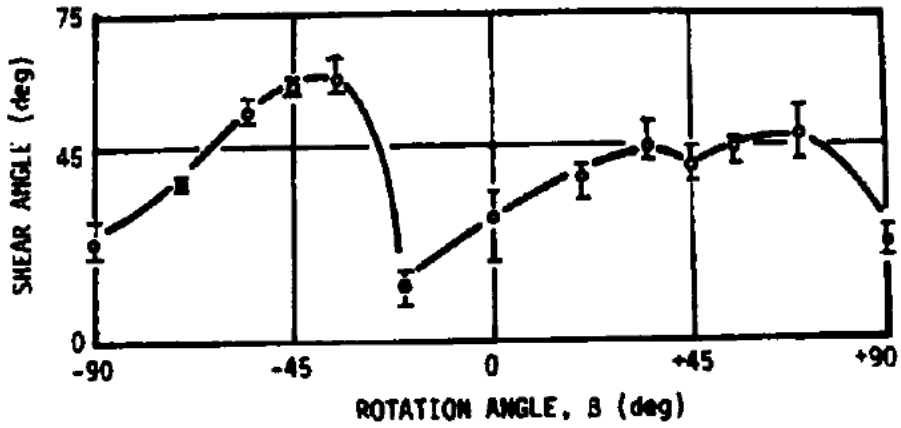


Figure 2.11 Variation of the shear angle with the rotation angle of a β-brass single crystal orthogonal cutting. The rotation axis corresponds to the [101] crystallographic direction [74]

Black [75] previously observed this phenomenon in single crystals of copper and aluminum, correlating lamella thickness with the depth of cut: the lamella spacing increases with the depth of cut, eventually stabilizing at around $2\mu m$.

Sato *et al.* [76, 77] studied more specifically the effect of crystallographic orientation on the finished surface. They conducted orthogonal cutting tests on aluminum single crystals and proved that cutting on the (111) slip plane in the $[0\bar{1}1]$ direction produces the lowest roughness and the best flatness on the surface. On the contrary, the $[1\bar{2}1]$ direction produced the worst surface quality since this direction is perpendicular to the sliding direction in the (111) slip plane. These observations confirmed that the variations of the cutting performance with cutting direction is explained by the crystallographic slip systems. Cohen [11] performed orthogonal turning tests on copper and aluminum single crystal disks and showed four-fold symmetric fluctuations in the machining forces when cutting around the $\langle 100 \rangle$ crystallographic axes for both materials. To *et al.* [78] performed orthogonal turning on aluminum single crystals on (001), (110) and (111) crystallographic planes. They observed an increase in the tangential cutting force with a decrease in the depth of cut, with the $\langle 110 \rangle$ and $\langle 111 \rangle$ orientations leading to the highest and lowest cutting forces, respectively. Lawson *et al.* [79] observed variations in cutting forces by threefold for different crystallographic orientations in orthogonal planing of aluminum single crystals.

Yuan *et al.* [80] also observed a crystallographic orientation effect on the surface roughness and cutting forces for single crystal copper and aluminum in ultraprecision diamond cutting. They modeled the crystal response to the machining induced shear by using an effective Taylor factor for a specific crystallographic direction and calculating the shear resistance of the crystal. This factor characterizes anisotropy by calculating the ratio between the crystallographic work and the macroscopic work [81] and paved the way for the first cutting force modeling method including anisotropy due to the crystallographic effect.

2.2.5 Microstructure-level machining process modeling

As mentioned in Section 2.1.2, classical machining models do not consider material anisotropy. Crystal plasticity has been used as a method to incorporate the elastic and plastic anisotropy of metals. Asaro and Needleman [82] has performed the first implementations in a finite element framework to model slip bands observed in the uniaxial response of single crystals. Kalidindi *et al.* [83] and Maniatty *et al.* [84] applied the method to polycrystals, thanks to the improvements in the

computers in the 1990s. Material anisotropy can be incorporated through either numerical methods such as FE analyses or analytical approaches by integrating crystal plasticity equations into the machining mechanics model.

Numerical methods

Numerical methods, like finite element techniques (FE) combined with crystal plasticity constitutive laws are the most accurate means to include anisotropy in machining models [85]. This is due to the ability to combine plasticity models across different length scales, providing a more comprehensive representation of the material behavior. Chuzhoy *et al.* [86, 87] incorporated the crystallographic effect on their FE model for micromachining of heterogeneous materials such as cast iron. A microstructure is generated according to the specified proportions and spatial distribution of pearlite, ferrite, and graphite, then the machining simulation is carried out with the tool moving forward by a distance smaller than the grain size. More recently, many studies used FE models to directly implement the crystallographic orientation of the grains in the cut material. Obikawa *et al.* [88] studied the microscopic phase-dependent residual stresses generated in machined surfaces of irons and steels. They developed a FE model to simulate a cutting operation and analysed the chip formation and the cutting forces and found that the workpiece microstructure significantly affects the residual stress distribution on the machined surface. Simoneau *et al.* [89, 90] defined micro-scale cutting as occurring when the uncut chip thickness is smaller than the average size of the smallest grain type in the material's microstructure. They compared experimental results on a AISI 1045 steel with their FE model and especially the chip formation evolution when the uncut chip thickness decreases. But despite the accuracy provided by FE methods, the high-strain-rate nature of the machining process, the frictional contact and chip formation make them computationally very expensive. Thus, analytical methods based on continuum mechanics offer a practical approach for simulating machining operations with both high accuracy and computational efficiency.

Analytical methods

Analytical machining mechanics models presented in Section 2.1.2 do not naturally include the effect of material anisotropy. To investigate the influence of anisotropic material behavior in the model, it is essential to account for the underlying physical mechanisms responsible for this anisotropy. Sato *et al.* [91, 92] developed a Schmid-law-based model to account for the orientation-

dependent differences in measured shear angles in an aluminum single crystal. Lee and Zhou [93] employed the Texture Softening Factor method to predict shear angles, a technique originally developed for studying shear banding. Lee and Yang [94] made the bridge between macro and microplasticity and applied the resulting theory (mesoplasticity) in the machining field and especially in the prediction of chip formation in single crystal cutting. Generally, analytical machining mechanics models are divided in two parts: first the machining kinematics equations allows to consider every cutting parameter including the tool geometry, the cutting conditions and the material properties, then, the crystal plasticity equations are used to calculate the deformation at the crystal level to finally obtain the shear stress on the shear plane. The second part differs depending on whether the analytical model is Taylor-based, physics-based or phenomenological. Taylor-based models were historically among the first to propose a solution to consider material anisotropy and were then adapted to machining. They were used to explain the crystallographic effect on the friction coefficient between the chip and the tool, which at the end has a significant impact on the chip generation and the cutting forces [95-98]. As mentioned in Section 2.2.4, Taylor factor accounts for the material anisotropy. The Taylor factor can be determined using the Taylor work minimization principle [81], which aims at determining the combination of slip systems activated when an external stress is applied on the material, mathematically stated as,

$$\sum_{\alpha=1}^{n} \tau_c^{\alpha} \dot{\gamma}^{\alpha} \leq \sum_{\alpha=1}^{n} \tau_c^{\alpha*} \dot{\gamma}^{\alpha*} \tag{2.7}$$

where $\dot{\gamma}^{\alpha}$ and τ_c^{α} are respectively the slip rates and CRSS of the activated slip system, while $\dot{\gamma}^{\alpha*}$ and $\tau_c^{\alpha*}$ are respectively the slip rates and CRSS of any set of slip systems accommodating the external stress. However, in Taylor-based models, all the slip systems are assumed to harden at the same rate which means that $\tau_c^{\alpha} = \tau_c^{\alpha*}$. Therefore, Eq. (2.7) becomes:

$$\sum_{\alpha=1}^{n} |\dot{\gamma}^{\alpha}| \leq \sum_{\alpha=1}^{n} |\dot{\gamma}^{\alpha*}| \tag{2.8}$$

Eq. (2.8) can be summarized in the following sentence: Among the 12 possible slip systems, the ones that become active is the combination that minimizes the total sum of absolute shear values.

The Taylor factor can then be calculated as follows:

$$M = \frac{\sum_\alpha d\gamma^\alpha}{d\varepsilon} \tag{2.9}$$

where $d\gamma^\alpha$ is the slip increment of the α^{th} slip system and $d\varepsilon$ is the macroscopic total strain increment.

The Bishop-Hill work maximization principle [99] is an alternative to the Taylor work minimization to calculate the Taylor factor. Although the names of both principles suggest they are opposites, they are mathematically equivalent. The work maximization principle states that, among the possible multiaxial stress states that activate to accommodate an external deformation, the one that maximizes the mechanical work is the operative stress state. Work increment is composed of 28 possible stress states [99] and strain increment for FCC materials, expressed in the crystal coordinate system,

$$dW = -B\ d\varepsilon_{11} + A\ d\varepsilon_{22} + 2F\ d\varepsilon_{23} + 2H\ d\varepsilon_{13} + 2I\ d\varepsilon_{12} \tag{2.10}$$

where the strain multiplier coefficients are defined as follows:

$$A = \frac{\sigma_{22} - \sigma_{33}}{\sqrt{6}\,\tau_c}, B = \frac{\sigma_{33} - \sigma_{11}}{\sqrt{6}\,\tau_c}, F = \frac{\sigma_{23}}{\sqrt{6}\,\tau_c}, H = \frac{\sigma_{13}}{\sqrt{6}\,\tau_c}, I = \frac{\sigma_{12}}{\sqrt{6}\,\tau_c} \tag{2.11}$$

Then, the Taylor factor is defined as,

$$M = \frac{dW}{\tau_c d\varepsilon_{VM}} \tag{2.12}$$

where $d\varepsilon_{VM}$ is the equivalent Von-Mises strain increment.

The shear stress is then calculated as a product between the CRSS and the Taylor factor,

$$\tau_s = M\,\tau_c \tag{2.13}$$

Taylor-based models provide a relatively straightforward approach to incorporating crystallographic anisotropy in machining mechanics models. However, some limitations, such as the use of a single hardening rate or the lack of strain rate sensitivity, have been shown to hinder the accuracy of machining mechanics predictions [73].

Physics-based analytical models are better representing what really happens at the crystal level during the cutting process [100, 101]. They use the dislocation mechanics as the underlying

physical basis for continuum crystal plasticity formulation and the dislocation density as the state variable of the model. Therefore, the slip rate of each slip system is calculated as follows,

$$\dot{\gamma}^{\alpha} = \varrho_m^{\alpha}\, b\, v^{\alpha}\, \mathrm{sign}(\tau^{\alpha}) \tag{2.14}$$

where ϱ_m^{α}, v^{α} and τ^{α} are the mobile dislocation density, the average glide velocity and the shear stress on the slip system α and b is the Burgers vector which quantifies the magnitude and direction of lattice distortion caused by a dislocation in a crystal.

Demir and Mercan [73] developed a physics-based orthogonal machining model for FCC single crystals and compared its performance to a Taylor-based machining model. They found that the physics-based model better predicted the location of the cutting force peaks and generally provided more accurate force patterns than the Taylor-based model when compared to experimental data [11]. Phenomenological models describe material behavior under load using empirical relationships derived from experimental data, rather than explicitly modeling dislocation mechanics. They rely on the CRSS as the state variable, and the slip rate of each slip system is governed by the power law proposed by Hutchinson [102],

$$\dot{\gamma}^{\alpha} = \dot{\gamma}_0 \left|\frac{\tau^{\alpha}}{\tau_c^{\alpha}}\right|^{n} \mathrm{sign}(\tau^{\alpha}) \tag{2.15}$$

where $\dot{\gamma}_0$ is the reference slip rate and n is the slip rate sensitivity parameter.

Physics-based and phenomenological models directly calculate the Cauchy stress tensor ($\boldsymbol{\sigma}$) in the shear plane, from which the shear stress is deduced while Taylor-based model estimates it from the CRSS (Eq. 2.13).

Boubaker *et al.* [103] proposed an analytical phenomenological model for single-crystal orthogonal machining that incorporates a non-uniform shear strain rate distribution within the shear zone. Phenomenological crystal plasticity formulations are also widely integrated in FE simulations [104-106].

Unlike physics-based models which require numerous unconventional material parameters, phenomenological models offer a simpler way to incorporate material anisotropy in machining, relying on fewer and more readily material parameters. In this thesis, a phenomenological analytical model for orthogonal cutting simulation on FCC single crystals is developed and then

adapted to milling and polycrystals including BCC and HCP lattice structures in order to simulate machining operations on AMed parts.

2.3 Additive manufacturing

Additive manufacturing (AM) process involves the direct, layer-by-layer deposition of material to fabricate prototypes or the near-net-shape of functional components from three-dimensional digital models.

2.3.1 Classification and characteristics

ASTM Standard F2792 [107] categorizes additive manufacturing processes into two broad groups: powder bed fusion (PBF) and directed energy deposition (DED) methods. PBF process involves spreading a thin layer of metal powder over a build platform using a roller or blade. A directed energy source, such as a laser (in the case of laser powder bed fusion LPBF) or an electron beam (electron beam melting EBM) is then applied to selectively fuse the material. The powder is deposited layer by layer, and the part is built additively. In the directed energy deposition (DED) process, material, either in powder or wire form, is fed through a nozzle and deposited onto a substrate, where it is simultaneously melted by a heat source. In this thesis, the wire laser additive manufacturing (WLAM) which is part of the DED group will be used in experimental verifications.

2.3.2 Effect on the microstructure

AM conveys anisotropy in the microstructure of the built part because of the thermal gradient generated by the metal melting and solidification [108]. The effect of AM on the microstructure has been observed in both powder bed fusion (PBF) and directed energy deposition (DED) processes.

Powder Bed Fusion (PBF)

It's been shown that the microstructure produced by selective laser melting (SLM) process was characterized by a preferred crystallographic orientation, and that the texture could be controlled by selecting specific laser scanning strategies or applying a heat treatment after printing. Zhou *et al.* [109] studied the crystal texture of a CoCrMo alloy produced by SLM with different scanning strategies. After an electron backscatter diffraction (EBSD) analysis, they found that columnar

grains were formed along the building direction (BD) when a zig-zag strategy was used whereas an arbitrary crystallization occurs with the cross-hatching strategy (Figure 2.12).

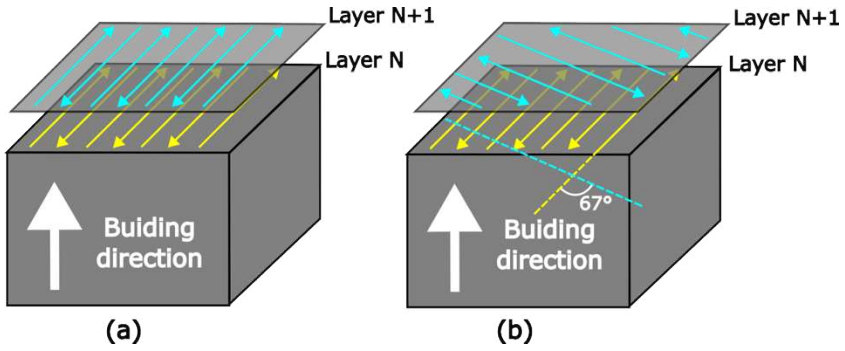


Figure 2.12 (a) zig-zag scanning strategy and (b) cross-hatching strategy. Reproduced from [109]

In the long columnar grains, one ⟨100⟩ orientation is parallel to the BD, and all the grains have another ⟨100⟩ orientation parallel to the scanning direction, with most of the time a (011) plane parallel to the scan surface. Kunze *et al.* [110] built nickel-based IN738LC cylindrical samples by SLM with their axis parallel or perpendicular to the BD. The same elongated grain morphology was found in the BD and crystals also had a ⟨100⟩ orientation parallel to both the building and scanning directions. Tensile tests on the specimens revealed that the Young's modulus was significantly lower in the BD than perpendicular to it and the mechanical anisotropy was not primarily correlated to grain shape but rather by the crystallographic orientation. Geiger *et al.* [111] used three different scanning strategies to build IN738LC samples through SLM: A the scanning direction rotates 90°, B the scanning direction rotates 90° with an initial rotation of 45° from the reference direction and C the scanning direction rotates 67°. The three strategies are illustrated in Figure 2.13

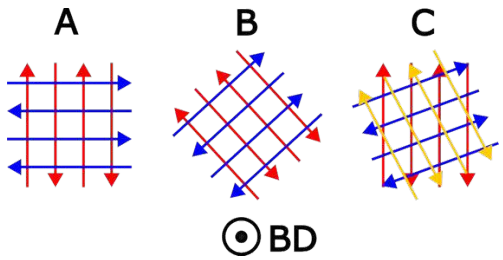


Figure 2.13 Three scanning strategies. Reproduced from [111]

They observed a strong crystallographic texture in the as-built samples with three scanning strategies. A predominant alignment of the crystals with one of their ⟨001⟩ axes parallel to the BD

was observed, regardless of the laser scanning strategy applied. They also showed that a heat treatment could almost annihilate the texture observed in the as-built samples. Thijs *et al.* [112] built AlSi10Mg parts via SLM with scanning strategy A and obtained the same crystallographic texture as in [111].

Direct Energy Deposition (DED)

In DED processes, the microstructure of the parts can vary depending on the distance from the substrate. Grain size near the substrate is typically smaller than in the central region of the deposit, as the colder substrate acts as a heat sink during the deposition of the initial layers [113]. EBSD analyses on AISI 316L produced by WLAM showed that the central region is mainly composed of columnar grains, and some small equiaxed grains [114]. Wang *et al.* [115] characterized the microstructure of a 316L stainless steel built with wire arc additive manufacturing (WAAM) and observed that the austenitic columnar grains have grown along the building direction, exhibiting ⟨100⟩ preferred orientation. The same observation was made by Chen *et al.* [116] who built 316L stainless steel samples through gas metal additive manufacturing (GMAAM). They also found that the material texture could be reduced with an appropriate heat treatment (1200°C, 4h) with the columnar grains transforming into equiaxed grains with random crystallographic orientation. Other studies show a preferred crystallographic orientation for 316L stainless steel built using a DED process, with one of the ⟨100⟩ orientations aligned with the BD [117, 118].

2.3.3 Effect on the machining mechanics

The influence of the layer-by-layer manufacturing process and the resulting microstructural anisotropy in additively manufactured (AMed) parts has already been experimentally observed in machining, notably through variations in cutting forces, chip formation, surface integrity, and vibration behavior. Calleja *et al.* [119] studied the machinability of Inconel 718 superalloy after laser cladding AM process. Turning tests performed on the wrought, as-built and heat treated (precipitation hardening) AMed parts. The resulting specific cutting pressures in turning were the highest for the laser cladding added material with precipitation hardening while the wrought and non-hardened laser cladding added materials exhibit similar values. Chen *et al.* [120] also studied the machinability of Inconel 718 in turning on both the base and added. It was shown that the cutting forces were 10% lower for the AMed workpiece than the wrought material, that was attributed to the poor density and the presence of microstructural defects in the AMed sample. In

addition, lower vibrations as well as higher roughness and irregular continuous chips were obtained when machining the AMed workpiece as compared to the wrought Inconel 718. Chernovol *et al.* [121] analyzed the interactions between the wire and arc additive manufacturing (WAAM) and milling process to determine the optimal machining and AM parameters to obtain the best surface quality. They showed that the welding parameters which influence the quality of the as-deposited surface also directly affects the machined surface. High flatness deviation in the as-deposited surface resulted in variations of the radial depth of cut and then, variations of the cutting forces in the subsequent machining operations. Fonseca *et al.* [122] performed orthogonal cutting tests on WAAM thin-walled steel structures and stated that the cutting force and consumed power could be 12% lower when cutting the AMed samples. However, their cutting force results indicate that lower values for the AMed parts are only observed when machining near the base of the sample, where the material is softer; in most cases, the measured cutting forces in AMed samples are higher than those in wrought material. Polishetty *et al.* [123] compared the cutting forces generated by the turning of a 316L stainless steel produced with SLM and its wrought counterpart for different cutting conditions. For each test, they measured higher cutting forces on the AMed parts. Le Coz *et al.* [124] performed turning operations on Ti-6Al-4V parts produced by SLM process and cast Ti-6Al-4V and systematically measured higher cutting forces for the AMed titanium alloy. The tangential force difference varies from 3% at the lowest feed rate (1 µm/rev) to 24% at the highest one (20 µm/rev). Al-Rubaie *et al.* [125] performed milling tests on SLM-produced Ti-6Al-4V and on its wrought counterparts. They calculated the resultant force from the measured forces in the X, Y, and Z directions and observed a 40% increase for the AMed parts compared to the wrought ones due to greater hardness caused by the SLM process. Kallel *et al.* [126] observed the same increase in milling a laser metal deposited (LMD) Ti-6Al-4V compared to the conventional alloy. Other studies relate a general increase of cutting forces in AMed parts compared to their wrought counterparts [127, 128]. The microstructure induced anisotropy of AMed parts causes their machining behavior to be directionally dependant. Lizzul *et al.* [129] studied the influence of microstructural anisotropy of a laser power bed fused (LPBF) Ti6Al4V alloy. By analyzing the chip morphology and the machined surfaces, they concluded that the tool life could be reduced by 40% when performing slot-milling operations in the BD. Bagherzadeh *et al.* [10] performed orthogonal machining operations on an AMed Inconel 718 using laser powder bed fusion and concluded that the best machinability was obtained when machining along the BD, with larger

shear angles and lower cutting forces because of the elongated grains parallel to the building direction, which promote subsurface deformations.

2.4 Summary

Machining mechanics modeling has progressed from early empirical laws to more advanced physics-based and numerical approaches. While slip-line and finite element models offer detailed predictions, they are limited by assumptions of isotropy or high computational cost. Merchant's analytical model remains a practical and efficient choice, especially for integrating microstructure effects in anisotropic materials. For these reasons, it forms the foundation of the modeling strategy used in this thesis.

Many researchers conducted machining experiments on single crystals to show that the crystallographic orientation has a significant impact on the chip formation, shear angles and cutting mechanics. Several modeling approaches have been developed to account for the microstructure induced anisotropy effect on the material mechanical behavior (Taylor models, physics-based models and phenomenological models) and then incorporated into the machining mechanics. The phenomenological approach, combined with the analytical Merchant's model for machining modeling offers the best compromise between prediction accuracy and computational cost.

As for single crystals, AMed parts exhibit a strong microstructure induced anisotropy, with elongated grains oriented parallel to the BD. Machining tests on AMed parts revealed higher measured cutting forces than on their wrought counterparts. While analytical models for cutting force prediction in single crystal materials that account for crystallographic anisotropy have already been developed in the literature, the anisotropic microstructures of AMed parts have not yet been integrated into such models. This thesis aims to fill this gap by developing two- and three-dimensional analytical, crystal-based machining mechanics models that account for the microstructure-induced anisotropy of AMed parts.

CHAPTER 3 ARTICLE 1: A CRYSTAL PLASTICITY-BASED MODEL FOR ORTHOGONAL MACHINING MECHANICS OF SINGLE CRYSTAL MATERIALS

Gabriel Dupoirieux
Department of Mechanical Engineering, Polytechnique Montréal
2500, Chemin de Polytechnique, H3T 1J4, Montréal, QC, Canada
gabriel.dupoirieux@polymtl.ca

Eralp Demir
Department of Engineering Science, University of Oxford,
Parks Road, Oxford, OX1 3PJ
eralp.demir@eng.ox.ac.uk

Oguzhan Tuysuz
Department of Mechanical Engineering, Polytechnique Montréal
2500, Chemin de Polytechnique, H3T 1J4, Montréal, QC, Canada
oguzhan.tuysuz@polymtl.ca

Journal: ASME-Manufacturing Science and Engineering
Initial submission date: April 22nd, 2025
Acceptance date: August 2nd, 2025

3.1 Abstract

Microstructural anisotropy caused by single crystal orientation, or by thermal gradients in casting and additive manufacturing processes poses significant direction-dependency in the machining behavior of materials. Effect of crystal orientation on the machining mechanics has not been fully explored yet. This study introduces a phenomenological crystal plasticity model to predict the cutting forces in orthogonal machining of single crystals, addressing the unique challenge of crystal orientation induced anisotropy. The proposed model incorporates temperature, strain rate, and strain hardening effects by adapting the Johnson-Cook constitutive law and integrating it into the

crystal plasticity framework for accurate simulation of the machining mechanics. The model evaluates the cutting force coefficients in two orthogonal directions along with the shear angle determined by minimizing the cutting power for any machining conditions such as uncut chip thickness, cutting speed, tool geometry, and friction coefficient. Comparison of the predicted cutting force coefficients with the experimental results on copper and aluminum single crystals demonstrates that the proposed model can accurately predict the specific cutting pressures and the impact of crystallographic orientation on the orthogonal machining mechanics. The introduced model offers a computationally efficient approach to better understand the deformation behavior in single-crystal machining and provides a basis for further extension to polycrystalline materials and milling operations.

3.2 Introduction

Predicting cutting forces with high accuracy is essential for controlling dimensional and surface quality in machining operations, especially when dealing with anisotropic materials such as single-crystal metals. Single crystal metals have unique properties, particularly the absence of grain boundaries, making them ideal for specific high-performance applications. Gas turbine blades are usually made of single-crystal nickel-based superalloys to handle high temperatures of the combustion gas without rapidly deteriorating [130]. Many semi-conductors are also single crystals because of their low defect density and no grain boundaries, which are very advantageous properties for solar cells, LEDs, and lasers [131]. Micromachining has various applications relying on single crystals as most of them concern the electronics field, but this process is more generally used for polycrystal metals. During micromachining of metals, the intense plastic deformation occurs at grain scale in the material, and the machining response, chip formation and resulting surface quality highly depends on crystal orientations because each grain has different slip systems and mechanical properties, leading to variations in the cutting forces. The resulting anisotropy at the crystal level prevents manufacturing engineers from using standard cutting parameters without risking the tool breakage. Hybrid manufacturing is another process in which material anisotropy cannot be ignored. When the near-net-shape geometry is obtained using casting or additive manufacturing such as directed energy deposition (DED) methods, grain sizes and orientations are affected by the generated heat flow when the metal melts and solidifies [111, 132]. In the subsequent machining operations, the material anisotropy needs to be considered to achieve better surface quality and dimensional accuracy.

The effect of crystal orientation on the machining response of face-centered cubic (FCC) metals has already been experimentally observed in terms of cutting forces, chip formation, and surface integrity [60, 61, 80]. Sato *et al.* [76, 77] reported that the surface roughness variations of a single crystal aluminum due to crystallographic orientation can exceed 65% in orthogonal machining. Cohen [11] used aluminum and copper single crystal disks to perform orthogonal cutting tests and showed a four-fold symmetry in the cutting forces by turning the workpiece around the ⟨100⟩ crystallographic direction. According to Zhou *et al.* [95], crystallographic orientation has a non-negligeable effect on the friction coefficient between the workpiece material and the cutting tool. The crystallographic orientation of the diamond cutting tool caused anisotropy in the friction coefficient, which in turn led to variations in the shear angle. Kieren-Ehses *et al.* [133] showed that the chip and blur formations were affected by the grain orientations in micromachining of polycrystal titanium alloys. Hence, considering the crystal orientations in machining mechanics simulations is highly critical to better represent the physics of metal deformation.

Integrating crystal orientation in machining models has recently attracted researchers' attention. Taylor-based single crystal methods as an upper bound for machining have been used as an efficient analytical approach to predict the anisotropy of shear angles and specific cutting energies (cutting force coefficients) [96, 97, 134]. Numerical models using finite elements (FE) simulations allow to accurately recreate the microstructure of the material with the orientation of each grain. Zhang *et al.* [135] simulated the material removal of polycrystal Ti-6Al-4V using a two-dimensional (2D) FE model in orthogonal cutting with randomly oriented grains and concluded that the crystallographic orientation strongly affects the chip morphology. Wang *et al.* [136] studied the machining of polycrystal copper with a diamond cutting tool using a 2D FE model with grain morphology and crystal orientations characterized by electron backscatter diffraction (EBSD) measurements. Their results captured the crystal-orientation induced anisotropy, showing a clear difference in the cutting forces and surface heights from one grain to another. Numerical models incorporating crystal plasticity laws provide the most accurate simulations for machining of polycrystals because each grain is defined separately, allowing the modeled microstructure to closely match the reality. However, numerical models are computationally expensive due to the high strain rates involved in the machining process. That computational challenge counterbalances the benefits of the numerical tools. Analytical models relying on the continuum material mechanics

are much more practical to simulate the machining operations with high accuracy and computational efficiency.

Among all the analytical models for machining simulations, two main categories emerge. Physics-based models directly account for the physical process that governs the plastic deformation at the crystal scale. Demir and Mercan [73] developed a physics-based crystal plasticity model for machining single crystals using the dislocation mechanics, which used the dislocation density as the state variable. Despite accurately representing the plastic deformation mechanism in the crystal framework, that type of analytical model needs more experimentally identified material input parameters than phenomenological models. On the other hand, phenomenological models rely on empirical relationships based on experimental observations to describe the material response to a load, rather than considering the direct representation of dislocation mechanics. Once calibrated, their efficiency is equal to their physics-based counterparts. Boubaker *et al.* [103] developed a phenomenological model for single crystal orthogonal machining using a non-uniform shear strain rate distribution in the shear zone. The temperature effect was incorporated into the model through an empirical relation proposed by Oxley [137]. Follansbee and Kocks [138] proposed the Mechanical Threshold Stress method in the hardening law of the material constitutive model to update the critical resolved shear stress in the material by considering the temperature and strain rate effects on the strain hardening. However, the elastic elongation was neglected while it contributes to the stress state of the metal in the shear zone.

To consider the temperature and shear strain rate effects on strain hardening in general crystal plasticity framework, researchers used Johnson-Cook (J-C) material constitutive model [139] along with Voce-type hardening law to update the critical resolved shear stress of the slip systems. Wang and Liu [140] studied magnesium single crystal's temperature and strain rate sensitivities with a crystal plasticity model using J-C constitutive law for strain hardening. Experimental data from compression tests were compared to a three-dimensional (3D) FE simulation, and increasing strain rate sensitivity with the temperature was captured. Chakrabarty and Song [141] used the J-C law for strain hardening in crystal plasticity to simulate a cold spray operation of a single crystal copper. However, analytical machining mechanics model based on crystal plasticity including the temperature and strain rate sensitivities through the J-C law has not been reported in literature.

In this work, a new, phenomenological crystal plasticity-based orthogonal machining mechanics model is proposed for FCC metals. The developed model integrates the J-C constitutive law into the machining-adapted crystal plasticity model for the first time. Both elastic and plastic deformation mechanics are used in the crystal plasticity framework to accurately model the effect of anisotropy on the machining mechanics through crystallographic orientation. The proposed model simultaneously considers the effects of temperature and strain rate on strain hardening by modifying the classical J-C model and maintains the computational efficiency by limiting the number of required material parameters to minimum. The introduced model predicts the shear angle, the cutting force coefficients (specific cutting pressures), and in turn the cutting forces for different crystal orientations. The variation of the cutting parameters (cutting speed, uncut chip thickness), tool geometry (rake angle), friction coefficient, temperature and their effects on the force prediction are all included in the model. The developed model has been experimentally verified in orthogonal machining of single crystal copper [11]. The introduced model currently relies on the perfectly sharp tool assumption, and turning operations on shafts, and pipes without engagement of the nose radius of the tool as well as orthogonal side milling can be simulated without any further assumptions on the cutting tool geometry. While this work focuses primarily on cutting force prediction, its ultimate objective is to enable a better understanding of how crystallographic anisotropy affects dimensional and surface quality. Accurate force prediction is a necessary first step toward this broader goal, particularly in hybrid manufacturing and micromachining, where local material behavior plays a critical role.

This article is organized as follows: Section 3.3 presents the orthogonal machining geometry used in the developed crystal plasticity model. Section 3.4 develops the deformation kinematics and introduces the crystal plasticity-modified phenomenological J-C constitutive law for strain hardening. Section 3.5 compares the predicted specific machining pressures (cutting force coefficients) and shear angles against the experimentally obtained ones, presents the effect of different machining parameters on the predicted specific cutting pressures in the tangential and radial directions, and shows the influence of crystallographic orientation on these pressures. The article is concluded in Section 3.6.

3.3 Orthogonal machining model

In this section, the orthogonal cutting geometry, kinematics, cutting parameters, and cutting forces are presented for completeness.

3.3.1 Orthogonal cutting

The proposed crystal plasticity model is integrated into the orthogonal machining mechanics [9] to simplify the kinematics equations. The primary shear zone can be considered a thick deformation zone inclined at the shear angle ϕ_c with respect to the cutting velocity direction. Unlike the thin shear plane assumption, a thick shear zone is adopted in this work, which allows for a precise geometric definition of the shear strain rate and its dependent parameters (the shear time t_s and the deformation gradient $\boldsymbol{F}$). The shear zone will be mentioned as the shear plane throughout the paper. The friction between the chip and the rake face of the tool in the secondary deformation zone is included in the model, but the friction between the clearance face and the newly machined surface in the tertiary shear zone is neglected owing to sharp cutting edge assumption and sufficiently high clearance angle. Figure 3.1 (a) shows a three-dimensional (3D) representation of the orthogonal cutting kinematics and the machining parameters (cutting speed V, width of cut w, uncut chip thickness h) required to calculate the cutting forces. Three frames presented in Figure 3.1 (b) are respectively the sample frame (X_0, Y_0, Z_0), the cutting frame (X_c, Y_c, Z_c), and the shear frame (X_s, Y_s, Z_s). The crystal frame is defined by three orthogonal crystallographic directions ([100],[010],[001]). Some crystallographic directions for FCC metals are shown in Figure 3.2 The use of multiple intermediate frames is necessary to consider the crystallographic orientation influence on the shear deformation zone. The different frame transformations will be addressed in Section 3.3.2.

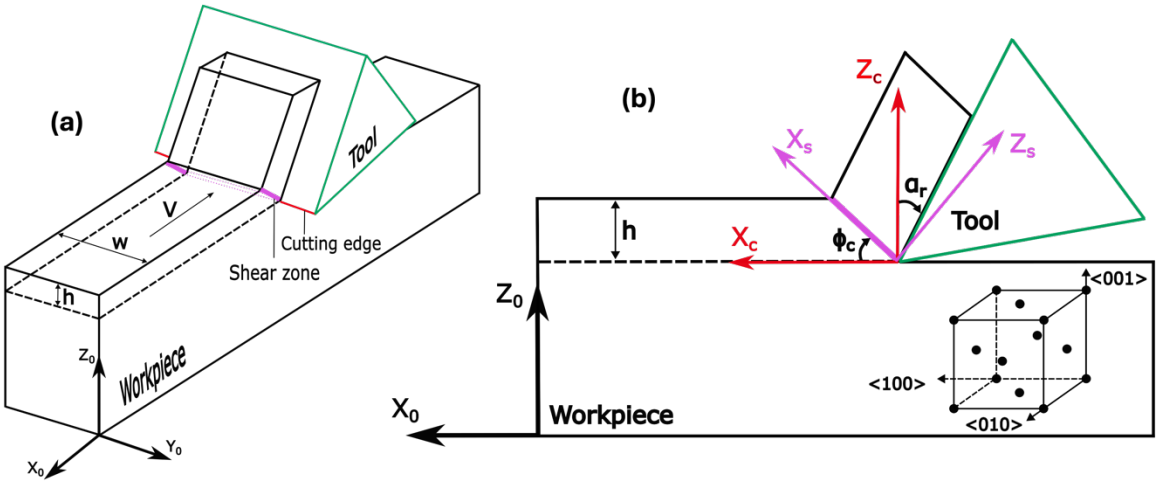


Figure 3.1 Representation of an orthogonal cutting process, (a) orthogonal cutting geometry, (b) sample, cutting, and shear frames

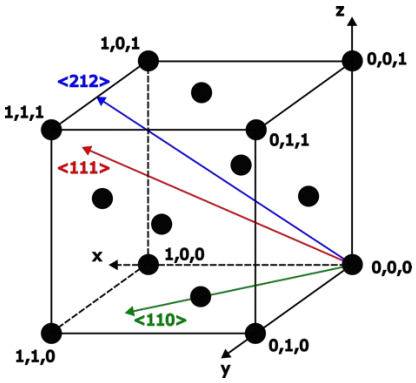


Figure 3.2 Some crystallographic directions for FCC metals in crystal frame

The force acting on the shear plane is derived from Merchant's geometry [142] as follows:

$$F_s = F_c \cos(\phi_c + \beta_a - \alpha_r) \tag{3.1}$$

$$F_c = \sqrt{{F_{tc}}^2 + {F_{fc}}^2} \tag{3.2}$$

where F_c, F_{tc} and F_{fc} are respectively the resultant, tangential and feed forces. α_r is the rake angle, and β_a is the friction angle. The shear force is then used to calculate the specific cutting pressures K_{tc} and K_{fc} (cutting force coefficients in tangential and feed directions), which are the main outputs of the proposed crystal plasticity-based machining mechanics model,

$$K_{tc} = \frac{\cos(\beta_a - \alpha_r)}{\cos(\phi_c + \beta_a - \alpha_r)} \frac{F_s}{wh} \tag{3.3}$$

$$K_{fc} = \frac{\sin(\beta_a - \alpha_r)}{\cos(\phi_c + \beta_a - \alpha_r)} \frac{F_s}{wh} \tag{3.4}$$

where w and h are respectively the width of cut and the uncut chip thickness. The shear force is obtained as the product of the shear stress (τ_s) on the shear plane and the shear plane area (A_s) as,

$$F_s = \tau_s \, A_s \tag{3.5}$$

τ_s is evaluated using the Cauchy stress tensor $\boldsymbol{\sigma}$ of the material in the shear plane. In the shear reference coordinate system (Figure 3.1 (b)), the component of the stress state corresponding to the shear stress is $\boldsymbol{\sigma}_{13}$,

$$\tau_s = \boldsymbol{\sigma}_{13} \tag{3.6}$$

The shear area depends on the shear angle ϕ_c and is calculated using the uncut chip thickness h and the width of cut w as,

$$A_s = \frac{h\, w}{\sin(\phi_c)} \tag{3.7}$$

In this article, the Cauchy stress tensor $\boldsymbol{\sigma}$ is obtained through the proposed temperature and rate-sensitive crystal plasticity model detailed in Section 3.4. For one value of the shear angle ϕ_c, the model calculates the corresponding stress state $\boldsymbol{\sigma}$ in the shear plane. The total cutting power $\dot{W}_{tot}$ is evaluated by summing the shear power $\dot{W}_s$ and the friction power $\dot{W}_f$.

$$\dot{W}_s = F_s \, V_s = \frac{\cos(\alpha_r)}{\cos(\phi_c - \alpha_r)} F_s \, V \tag{3.8}$$

$$\dot{W}_f = F_u \, V_c = \frac{\sin(\beta_a)\sin(\phi_c)}{\cos(\phi_c + \beta_a - \alpha_r)\cos(\phi_c - \alpha_r)} F_s \, V \tag{3.9}$$

where V, V_s and V_c are respectively the cutting, shear and chip speeds and F_u is the friction force.

$$\dot{W}_{tot} = \dot{W}_s + \dot{W}_f \tag{3.10}$$

The shear angle is evaluated by minimizing the total cutting power [29] in the shear plane for a range of candidate shear angles ($\phi_c \in \left[0,\ \frac{\pi}{2} - (\beta_a - \alpha_r)\right]$).

3.3.2 Orthogonal turning process

Plunge turning is well suited to capture the effect of crystal orientation induced anisotropy on the cutting force coefficients and the shear angle as the workpiece rotates. The cutting edge of the tool remains parallel to the rotation axis, which allows the edge to cut all around the crystal as it rotates (θ) with the workpiece as shown in Figure 3.3. To account for the effect of crystal orientation on the stress state of the shear plane, plunge turning kinematics needs to be described. In this section, the frame transformations between the crystal and shear plane frames are developed specifically for orthogonal plunge turning process.

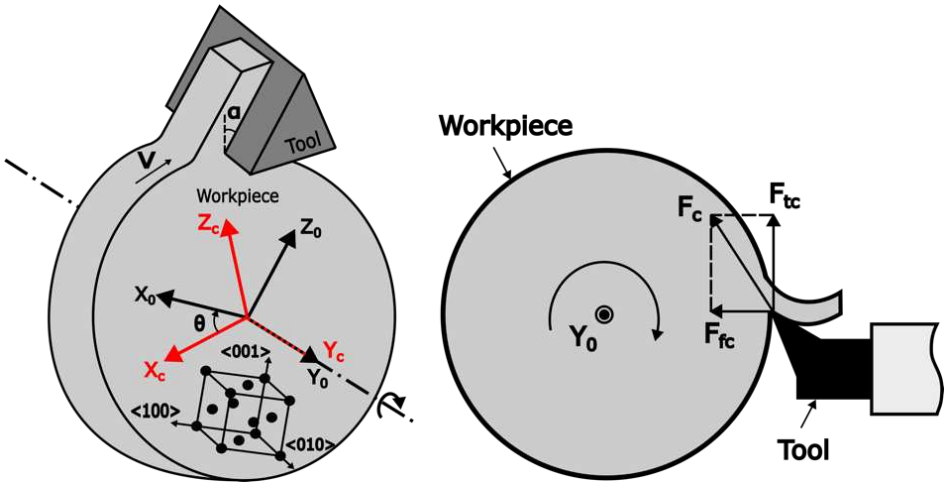


Figure 3.3 Representation of a plunge turning operation around the <010> crystallographic zone axis. (X_0, Y_0, Z_0) is the sample reference frame and (X_c, Y_c, Z_c) is the cutting reference frame. The workpiece rotates around $Y_0 = Y_c$, aligned with the <010> crystallographic direction

The single crystal orientation with respect to the workpiece is described using the crystallographic directions $[uvw]$, $[pqr]$ and $[hkl]$ in the workpiece reference coordinate system (sample frame). For instance, when the crystallographic axes are aligned with the sample reference axes (X_0, Y_0, Z_0), the crystal orientation is $[100] - [010] - [001]$. The transformation matrix between the sample frame and the crystal reference is expressed as,

$$\boldsymbol{T}_{sample \rightarrow crystal} = \begin{bmatrix} u & p & h \\ v & q & k \\ w & r & l \end{bmatrix} \tag{3.11}$$

The rotation of the workpiece with respect to the tool is characterized by an angle $\theta \in [0,360]°$ ($\theta < 0$ if the workpiece rotates clockwise) as shown in Figure 3.3. The sample frame rotates with respect to the reference of the tool (cutting frame) around $Y_0 = Y_c$ axis. This transformation is represented through the transformation matrix $\boldsymbol{T}_{sample \rightarrow cutting}$:

$$\boldsymbol{T}_{sample \rightarrow cutting} = \begin{bmatrix} \cos(\theta) & 0 & \sin(\theta) \\ 0 & 1 & 0 \\ -\sin(\theta) & 0 & \cos(\theta) \end{bmatrix} \tag{3.12}$$

As the cutting velocity direction is aligned with X_c, the shear plane (shear frame) is rotating with respect to the cutting frame around $Y_c = Y_s$. Since ϕ_c is defined clockwise, this transformation is described as,

$$\boldsymbol{T}_{cutting \rightarrow shear} = \begin{bmatrix} \cos(\phi_c) & 0 & \sin(\phi_c) \\ 0 & 1 & 0 \\ -\sin(\phi_c) & 0 & \cos(\phi_c) \end{bmatrix} \tag{3.13}$$

Since the shear stress of the material is calculated in the shear reference coordinate system, the overall transformation from the crystal frame to the shear frame is described by the following transformation matrix $\boldsymbol{R}$:

$$\boldsymbol{R} = \boldsymbol{T}_{cutting \rightarrow shear}\, \boldsymbol{T}_{sample \rightarrow cutting}\, \boldsymbol{T}^{T}_{sample \rightarrow crystal} \tag{3.14}$$

3.3.3 Shear strain and shear strain rate

The deformation gradient $\boldsymbol{F}$ defined in the shear frame for orthogonal cutting is written as,

$$\boldsymbol{F} = \begin{bmatrix} 1 & 0 & \gamma \\ 0 & 1 & 0 \\ 0 & 0 & 1 \end{bmatrix} \tag{3.15}$$

where γ is the shear strain that depends on the rake α_r and shear ϕ_c angles. It is geometrically defined as the ratio between the shear increment Δs and the shear zone thickness Δd shown in Figure 3.4.

$$\gamma = \frac{\Delta s}{\Delta d} = \frac{\cos(\alpha_r)}{\sin(\phi_c)\cos(\phi_c - \alpha_r)} \tag{3.16}$$

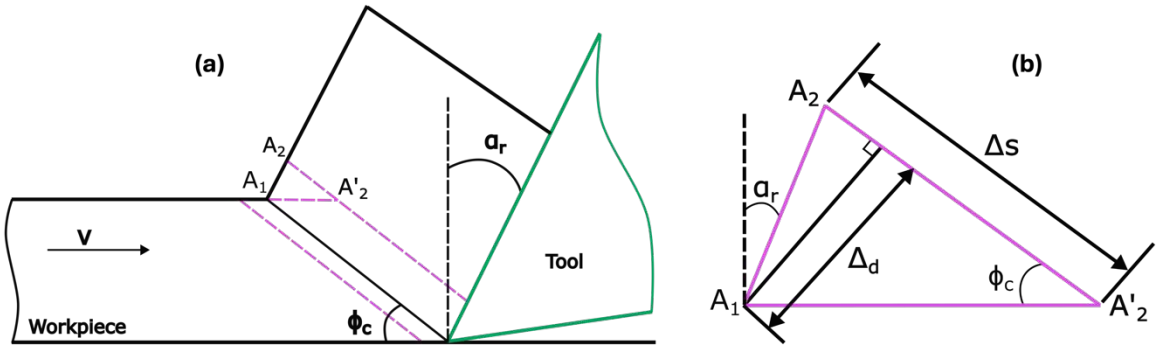


Figure 3.4 (a) Geometry of the deformation in the shear zone, (b) Shearing geometry. Symbols Δs and Δd are respectively the shear increment and the shear zone thickness

The shear velocity can be defined as,

$$V_s = \frac{\Delta s}{\Delta t} = \frac{V\cos(\alpha_r)}{\cos(\phi_c - \alpha_r)} \tag{3.17}$$

where Δt is the time increment. Therefore, the shear strain rate becomes,

$$\dot{\gamma} = \frac{\gamma}{\Delta t} = \frac{1}{\Delta d}\frac{\Delta s}{\Delta t} = \frac{V_s}{\Delta d} = \frac{V\cos(\alpha_r)}{\Delta d\cos(\phi_c - \alpha_r)} \tag{3.18}$$

In practice, the shear zone thickness can be approximated by a fraction of the shear plane length (L_c) [29] as,

$$\Delta d = k\,L_c \qquad k \in [0.15; 0.2] \tag{3.19}$$

where L_c is a function of the uncut chip thickness h and the shear angle ϕ_c.

$$L_c = \frac{h}{\sin(\phi_c)} \tag{3.20}$$

3.3.4 Temperature rise in the shear zone

A part of the plastic deformation caused by the turning process is converted into heat in the thick shear zone. The temperature rise in the shear zone can be modeled through the following relation proposed in [137],

$$T_s = T_r + \lambda_h(1 - \lambda_s)\frac{\dot{W}_s}{m_c c_s} \tag{3.21}$$

where λ_h (≈ 0.7) [29] is a factor that accounts for the plastic work occurring outside the shear zone and λ_s is the proportion of heat transferred into the workpiece. m_c, c_s and T_r are respectively the material removal rate, the specific heat of the material and the room temperature. The part of the heat conducted into the material of the workpiece is calculated according to the experimentally derived relations [137]:

$$\begin{cases} \lambda_s = 1 \quad \text{for } 0 \leq R_T \tan(\phi_c) \leq 0.04 \\ \lambda_s = 0.5 - 0.35 \log(R_T \tan(\phi_c)) \quad \text{for } 0.04 \leq R_T \tan(\phi_c) \leq 10 \\ \lambda_s = 0.3 - 0.15 \log(R_T \tan(\phi_c)) \quad \text{for } R_T \tan(\phi_c) \geq 10 \end{cases} \tag{3.22}$$

where R_T is a nondimensional thermal number calculated as,

$$R_T = \frac{\rho c_s V h}{c_t} \tag{3.23}$$

where c_t is the thermal conductivity of the material.

3.4 Proposed crystal plasticity-based machining model

In this section, elastic-plastic equations of the material deformation are developed. First, kinematics of the deformations at macro and micro levels are given, and then the crystal plasticity constitutive laws are derived. Though this article focuses on orthogonal machining, the developed deformation kinematics is independent of two- or three-dimensional machining.

3.4.1 Deformation kinematics

The shearing process in orthogonal turning involves continuous deformation over time. For a given shear angle ϕ_c, the deformation gradient in the shear zone can be expressed as a function of the shear strain rate $\dot{\gamma}$ and time $t \in \left[0, \frac{\gamma}{\dot{\gamma}}\right]$ as,

$$\boldsymbol{F} = \begin{bmatrix} 1 & 0 & \dot{\gamma} t \\ 0 & 1 & 0 \\ 0 & 0 & 1 \end{bmatrix} \tag{3.24}$$

The derivative of the deformation gradient with respect to time is evaluated using the deformation gradient at the current time ($\boldsymbol{F}$), its previous value $\boldsymbol{F}(t)$, and the time increment Δt,

$$\dot{\boldsymbol{F}} = \frac{\boldsymbol{F} - \boldsymbol{F}(t)}{\Delta t} \tag{3.25}$$

Hence, the velocity gradient can be expressed as,

$$\boldsymbol{L} = \dot{\boldsymbol{F}}\boldsymbol{F}^{-1} \tag{3.26}$$

The total strain is calculated in its tensorial form with the velocity gradient $\boldsymbol{L}$ and the time increment Δt as,

$$\boldsymbol{\varepsilon} = \frac{\boldsymbol{L} + \boldsymbol{L}^T}{2}\Delta t \tag{3.27}$$

The total strain ($\boldsymbol{\varepsilon}$) vectorized in Voigt notation is the sum of the elastic strain ($\boldsymbol{\varepsilon}^e$) and the plastic one ($\boldsymbol{\varepsilon}^p$) as given in Eq. (3.28). The Cauchy stress ($\boldsymbol{\sigma}$) is then calculated using the elastic part of the total strain $\boldsymbol{\varepsilon}^e$ and the elasticity matrix $\boldsymbol{C}$. $\boldsymbol{\varepsilon}^e$ is composed of its value at the previous time step $\boldsymbol{\varepsilon}^e(t)$ and the current elastic strain increment $\Delta\varepsilon^e$,

$$\boldsymbol{\varepsilon} = \boldsymbol{\varepsilon}^e + \boldsymbol{\varepsilon}^p \tag{3.28}$$

$$\boldsymbol{\sigma} = \boldsymbol{C}\boldsymbol{\varepsilon}^e = \boldsymbol{C}.(\boldsymbol{\varepsilon}^e(t) + \Delta\boldsymbol{\varepsilon}^e) \tag{4.29}$$

Then, the Cauchy stress in the thick deformation zone can be expressed as a function of a trial stress $\boldsymbol{\sigma}_{tr}$ and a plastic strain corrector,

$$\boldsymbol{\sigma} = \boldsymbol{C}.(\boldsymbol{\varepsilon}^e(t) + \Delta\boldsymbol{\varepsilon} - \Delta\boldsymbol{\varepsilon}^p) \tag{4.30}$$

$$\boldsymbol{\sigma} = \boldsymbol{\sigma}_{tr} - \boldsymbol{C}.\Delta\boldsymbol{\varepsilon}^p \tag{3.31}$$

where $\Delta\boldsymbol{\varepsilon}$ and $\Delta\boldsymbol{\varepsilon}^p$ are respectively the increments of the total and plastic strains. The plastic corrector ($\boldsymbol{\sigma}_p = \boldsymbol{C}.\Delta\boldsymbol{\varepsilon}^p$) is the unknown that must be calculated to determine the Cauchy stress tensor ($\boldsymbol{\sigma}$) of the material in the shear plane. The trial stress is computed using $\boldsymbol{\sigma}$ at the previous time step and the total strain increment.

$$\boldsymbol{\sigma}_{tr} = \boldsymbol{\sigma}(t) + \boldsymbol{C}.\Delta\boldsymbol{\varepsilon} \tag{3.32}$$

To calculate the plastic corrector, it is necessary to calculate the plastic strain increment $\Delta\varepsilon^p$, which is presented next.

The plastic part of the velocity gradient $(\boldsymbol{L}_p)$ is evaluated by the sum of all the slip rates $\dot{\gamma}^{\alpha}$ over the undeformed slip systems as,

$$\boldsymbol{L}_p = \sum_{\alpha} \dot{\gamma}^{\alpha}\, \boldsymbol{s}_0^{\alpha} \otimes \boldsymbol{n}_0^{\alpha} \tag{3.33}$$

where, $\boldsymbol{s}_0^\alpha \otimes \boldsymbol{n}_0^\alpha$ represents the dyadic product of the slip direction $\boldsymbol{s}_0^\alpha$ and the normal direction $\boldsymbol{n}_0^\alpha$ of the slip system α at the undeformed state ($t = 0$). The plastic strain increment $\Delta\boldsymbol{\varepsilon}^p$ is evaluated using the symmetric part of the deformed plastic strain rate tensor ($\boldsymbol{D}_p$) [143] in Voigt notation,

$$D_p = \sum_\alpha \dot{\gamma}^\alpha \left(\frac{\boldsymbol{s}^\alpha \otimes \boldsymbol{n}^\alpha + \boldsymbol{n}^\alpha \otimes \boldsymbol{s}^\alpha}{2} \right) \tag{3.34}$$

$$\Delta\boldsymbol{\varepsilon}^p = \boldsymbol{D}_p \, \Delta t \tag{3.35}$$

Hutchinson [102] established a direct and distinctive relationship between the resolved shear stress and the shear strain rate for a given slip system and expressed it as a viscoplastic power-law formulation,

$$\dot{\gamma}^\alpha = \dot{\gamma}_0 \left| \frac{\tau^\alpha}{\tau_c^\alpha} \right|^n sign(\tau^\alpha) \tag{3.36}$$

where, $\dot{\gamma}_0$ is the reference slip rate of the slip systems, τ^α is the resolved shear stress on the slip system α, τ_c^α is the critical resolved shear stress (CRSS) on the slip system α, and n is the slip rate sensitivity parameter. The resolved shear stress τ^α can be obtained through the projection of $\boldsymbol{\sigma}$ onto each slip plane and slip direction as,

$$\tau^\alpha = \boldsymbol{s}^\alpha . (\boldsymbol{\sigma} . \boldsymbol{n}^\alpha) \tag{3.37}$$

In this study, crystal plasticity kinematic equations (Eqs. (3.24)-(3.37)) are iteratively solved using the Newton-Raphson minimization method.

Once $\boldsymbol{\sigma}$ at the current time t is calculated, the crystal orientation needs to be updated for the next time step. Thus, the transformation matrix $\boldsymbol{R}$ is changed to update the slip vectors $\boldsymbol{s}^\alpha$ and $\boldsymbol{n}^\alpha$ as well as the elasticity matrix $\boldsymbol{C}$**.** The elastic part of the velocity gradient $\boldsymbol{L}_e$ is obtained by subtracting the plastic part ($\boldsymbol{L}_p$) from the total velocity gradient $\boldsymbol{L}$ as,

$$\boldsymbol{L}_e = \boldsymbol{L} - \boldsymbol{L}_p \tag{3.38}$$

The elastic part of the spin tensor ($\boldsymbol{W}_e$) is the antisymmetric part of the elastic velocity gradient $\boldsymbol{L}_e$,

$$\boldsymbol{W}_e = \left(\frac{\boldsymbol{L}_e - \boldsymbol{L}_e^{\,T}}{2} \right) \tag{3.39}$$

At the end of the current time step, the rotation matrix $\boldsymbol{R}$ is then updated as,

$$\boldsymbol{R} = (\boldsymbol{I} - \boldsymbol{W}_e\,\Delta t)^{-1}\,\boldsymbol{R}(t) \tag{3.40}$$

3.4.2 Constitutive law

FCC metals are cubic materials, and their stiffness matrix $\boldsymbol{C}$ depends on three elastic components C_{11}, C_{12} and C_{44}. In the crystal reference, elasticity matrix takes the following form in Voigt notation,

$$\boldsymbol{C} = \begin{bmatrix} C_{11} & C_{12} & C_{12} & 0 & 0 & 0 \\ C_{12} & C_{11} & C_{12} & 0 & 0 & 0 \\ C_{12} & C_{12} & C_{11} & 0 & 0 & 0 \\ 0 & 0 & 0 & C_{44} & 0 & 0 \\ 0 & 0 & 0 & 0 & C_{44} & 0 \\ 0 & 0 & 0 & 0 & 0 & C_{44} \end{bmatrix} \tag{3.41}$$

The slip resistance of each slip system is characterized by ${\tau_c}^{\alpha}$. The evolution of the slip resistance is modeled using the Voce-type hardening law to evaluate the strain hardening of slip systems in the proposed model. Then, the single-slip hardening rate can be described as,

$$\dot{h}^{\beta} = h_0 \left(1 - \frac{\tau^{\beta}}{\tau_c^{sat}}\right)^{E} \tag{3.42}$$

where, h_0, τ_c^{sat} and E are respectively the reference hardening rate, the saturation value of the slip resistance, and the strain hardening exponent. The evolution of the critical resolved shear stress ${\dot{\tau}_c}^{\alpha}$ (slip resistance) is given by the sum of the single-slip hardening rates $\dot{h}^{\beta}$ multiplied by the slip rate $\dot{\gamma}^{\beta}$ and a dependency matrix $\boldsymbol{X}_{\beta}^{\alpha}$ [143],

$${\dot{\tau}_c}^{\alpha} = \sum_{\beta} \boldsymbol{X}_{\beta}^{\alpha}\,\dot{h}^{\beta}\,\left|\dot{\gamma}^{\beta}\right| \tag{3.43}$$

$$\boldsymbol{X}_{\beta}^{\alpha} = \begin{bmatrix} \boldsymbol{A} & q\boldsymbol{A} & q\boldsymbol{A} & q\boldsymbol{A} \\ q\boldsymbol{A} & \boldsymbol{A} & q\boldsymbol{A} & q\boldsymbol{A} \\ q\boldsymbol{A} & q\boldsymbol{A} & \boldsymbol{A} & q\boldsymbol{A} \\ q\boldsymbol{A} & q\boldsymbol{A} & q\boldsymbol{A} & \boldsymbol{A} \end{bmatrix} \tag{3.44}$$

$\boldsymbol{X}_{\beta}^{\alpha}$ considers the influence of the slip rate of the other slip systems on the evolution of the critical resolved shear stress of one particular slip system. $\boldsymbol{A}$ is a 3×3 matrix of ones and q is the latent to self-hardening ratio that describes the relationship between the hardening rate of each slip system

(self-hardening) and the slip rate of all systems (latent hardening) [144]. To consider the temperature rise and high-strain-rates in machining, Eq. (3.43) is modified to simultaneously include the shear strain rate and temperature effects on strain hardening of the slip systems by adapting Johnson-Cook (J-C) constitutive material model to crystal plasticity. The traditional J-C constitutive law [139] is given by:

$$\boldsymbol{\sigma}_{JC} = (A + B\varepsilon^{n})\left(1 + C\ ln\frac{\dot{\varepsilon}_p}{\dot{\varepsilon}_0}\right)\left[1 - \left(\frac{T - T_r}{T_m - T_r}\right)\right]^{m} \tag{3.45}$$

where, A is the yield stress under quasi-static conditions, B is the hardening modulus, n is the hardening exponent, C is the strain rate coefficient, $\dot{\varepsilon}_p$ is the plastic strain rate, $\dot{\varepsilon}_0$ is the reference strain rate, T is the temperature, T_r is the room temperature, T_m is the melting temperature, and m is the thermal softening exponent of the workpiece material. Replacing the first term by the Voce-type hardening law (Eq. (3.43)) allows to incorporate strain rate and temperature effects into the shear strain hardening of the workpiece material during chip generation. Then, the proposed hardening rule is,

$$\dot{\tau}_c{}^{\alpha} = \sum_{\beta} \boldsymbol{X}_{\beta}^{\alpha}\ h_0\left(1 - \frac{\tau^{\beta}}{\tau_c^{sat}}\right)^{E}\left(1 + C\ ln\frac{|\dot{\gamma}|}{\dot{\gamma}_0}\right)\left[1 - \left(\frac{T_s - T_r}{T_m - T_r}\right)\right]^{m}|\dot{\gamma}^{\beta}| \tag{3.46}$$

where T_s is the temperature in the shear plane, $\dot{\gamma}$ is the shear strain rate of the machining process and $\dot{\gamma}_0$ is the reference shear strain rate. The proposed modified J-C hardening law offers a simpler way to include the shear strain rate and workpiece temperature effects in the proposed machining mechanics model. J-C parameters as well as the optimized parameters for h_0, $\tau_c{}^{sat}$ and E used in the Voce-type part of the proposed hardening rule for various materials are widely available in literature [145-147]. To summarize the calculation procedure, for a given couple of rotation θ and shear ϕ_c angles, the orthogonal machining mechanics equations (Eqs. (3.15)-(3.20)) are used to compute the initial value of $\boldsymbol{F}$ (Eq. (3.24)) at the beginning of each time step. Then the plastic corrector $\boldsymbol{\sigma}_p$ is computed iteratively in the crystal plasticity solver (Eqs. (3.24)-(3.37)) and the state variable τ_c^{α} is updated in Eq. (3.46) for the next time step. A total cutting power minimization allows to find the true shear angle ϕ_c and calculate the cutting force coefficients (Eqs. (3.1)-(3.10)).

3.5 Experimental verification

The proposed model is used to predict the specific cutting pressures (cutting force coefficients) in a plunge-turning operation on copper and aluminum single crystals (FCC materials). The predictions are compared against the experimental results for $\langle 010 \rangle$ crystallographic orientation given in [11]. Then, the influence of the crystallographic orientation, the cutting tool geometry (rake angle), friction coefficient, and cutting parameters (uncut chip thickness, cutting speed) on the predicted cutting force coefficients are shown with simulation results.

3.5.1 Crystal plasticity-based machining mechanics model validation

Cutting tests were performed [11] on single-crystal copper and aluminum disks in plunge turning. The rotation axis of the workpieces was aligned with the $\langle 001 \rangle$ crystallographic axis. The cutting operations were conducted at very low cutting speeds, $0.55\ mm/s$ for the copper samples and $0.44\ mm/s$ for the aluminum samples, and the shear angles along with both orthogonal force components, F_{tc} and F_{fc} were measured. The tangential and feed cutting force coefficients (K_{tc} and K_{fc}) were deduced using Eqs. ((3.1)-(3.4)). The uncut chip thickness was set to $0.11\ mm$ for every experiment. The widths of cut were respectively set to $2.35\ mm$ and $1.46\ mm$ for the copper and aluminum which are the average thicknesses of the disks used in [11]. Three different rake angles (α_r) of 20°, 40° and 50° were used in the experimental tests. The average friction angle (β_a) was calculated with the experimental values of F_{tc} and F_{fc} as follows,

$$\beta_a = \alpha_r + \tan^{-1}\left(\frac{F_{fc}}{F_{tc}}\right) \tag{3.47}$$

A summary of the cutting parameters used for each test is given Table 3.1.

Table 3.1 Values of machining parameters in the experiments [11]

Test number	**Material**	V **mm/s**	h **(mm)**	w **(mm)**	α_r **(deg)**	β_a **(deg)**
T1	Cu	0.55	0.11	2.35	20	43
T2	Cu	0.55	0.11	2.35	40	60
T3	Al	0.44	0.11	1.46	40	47
T4	Al	0.44	0.11	1.46	50	57

The material temperature is assumed to remain at room temperature at $T = 300K$ during machining owing to extremely low cutting speeds.

The constants used in the proposed machining mechanics model for copper and aluminum single crystals [11] are given in Table 3.2. The flow rule parameter $\dot{\gamma}_0$ is set to 0.001/s as suggested in literature [140, 141, 148]. The rate sensitivity exponent n was calibrated in T1 and T3 and set to 6.8 and 15 for the copper and the aluminum respectively due to the intense shear strains and high strain rates involved in machining [102]. Three parameters of the Voce-type hardening law (h_0, τ_c^{sat} and E) are respectively set to 180 MPa, 148 MPa and 2.25 for copper single crystal [146, 147] and 75 MPa, 63 MPa and 2.25 for aluminum single crystal [149, 150]. In the dependency matrix $\boldsymbol{X}_{\beta}^{\alpha}$, the latent to self-hardening ratio q is taken to 1.0 for coplanar slip systems ($\alpha = \beta$) and 1.4 for non-coplanar slip systems ($\alpha \neq \beta$) [146]. J-C model coefficients are obtained for pure copper and aluminum from literature [145] to represent the strains and strain rates that the material undergoes in orthogonal cutting tests in [11]. Every component of the initial stress state of the material $\boldsymbol{\sigma}_0$ is set to 0 MPa, and the initial value for the critical resolved shear stress τ_c^0 is set to 16 MPa for copper [146] and 31 MPa for aluminum [149]. The thickness of the shear zone (Eq. (3.19)) is computed with $k = 0.175$, average value of the interval proposed in [29].

Figure 3.5 shows the comparison of experimentally obtained [11] specific cutting pressures (cutting force coefficients) and the predicted ones using the proposed model by considering the effect of crystal orientation (anisotropy) as the workpiece rotates in orthogonal turning of single crystal copper (T1 and T2).

Table 3.2 Model parameters

	Parameter	**Description**	**Copper**	**Aluminum**
Flow rule	$\dot{\gamma}_0$	Reference slip rate (s^{-1})	0.001	0.001
	n	Rate sensitivity	7.2	15
	h_0	Strain hardening coefficient (MPa)	180	75

Hardening law (Voce-type law part) [146, 149]	τ_c^{sat}	Saturation value of CRSS (MPa)	148	63
	E	Hardening exponent	2.25	2.25
	τ_c^0	Initial critical resolved shear stress (MPa)	16	31
Hardening law (JC part) [145]	C	Strain rate coefficient	0.025	0.001
	$\dot{\gamma}_0$	Reference shear strain rate (s^{-1})	10^3	10^3
	T_r	Reference temperature (K)	293	293
	T_m	Melting temperature (K)	1356	916
	m	Thermal softening exponent	1.09	0.895
Elasticity [73, 149]	C_{11}	Single crystal elastic constants for copper (MPa)	168×10^3	107×10^3
	C_{12}		121.4×10^3	60×10^3
	C_{44}		75.4×10^3	28×10^3

As seen in Figure 3.5, the proposed model accurately predicts the cutting force coefficients (K_{tc} and K_{fc}) as the crystal rotates around the ⟨010⟩ zone axis, especially for the 40° rake angle case in (c) and (d) as the results for 20° rake angle cannot well capture the expected four-fold symmetry experimentally. The predicted crystal orientation dependency (anisotropy) of the cutting force coefficients is also accurately predicted by the introduced model. Due to the cubic geometry of the single crystal, the cutting force coefficients have four-fold symmetry as expected. However, experimental data in Figure 3.5 (c) and (d) exhibits an abnormal behavior beyond the orientation angle of 300°. Based on crystallographic symmetry of the single crystal copper, the data was expected to follow a continued periodic pattern.

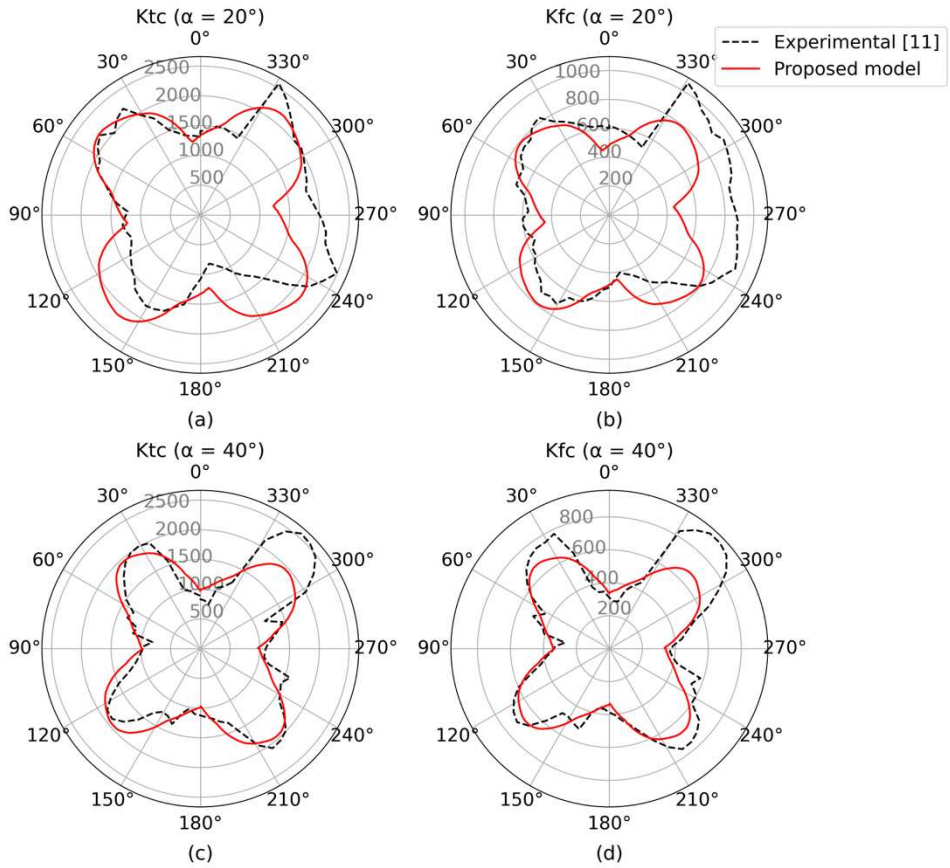


Figure 3.5 Comparison of experimentally measured and predicted cutting force coefficients (MPa), (a) K_{tc} in T1 ($\alpha_r = 20°$), (b) K_{fc} in T1 ($\alpha_r = 20°$), (c) K_{tc} in T2 ($\alpha_r = 40°$) and (d) K_{fc} in T2 ($\alpha_r = 40°$) for ⟨010⟩ crystallographic orientation of single crystal copper

Figure 3.6 shows the comparison between the experimental and predicted tangential cutting force coefficient K_{tc} for the aluminum samples. Similar to copper, K_{tc} matches well with the experimental values. Unfortunately, the experimental data [11] for K_{fc} were of poor quality, containing repeated or zero values, making meaningful comparison with the model predictions impossible.

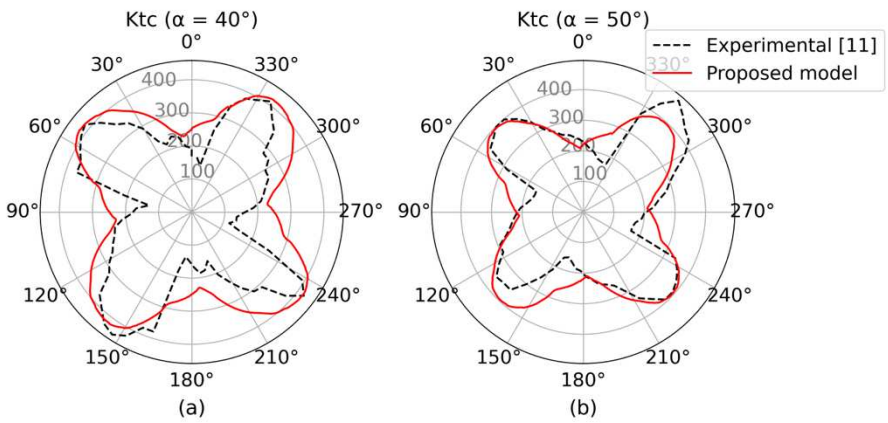


Figure 3.6 Comparison of experimentally measured and predicted K_{tc} (MPa), (a) in T3 ($\alpha_r = 40°$) and (b) in T4 ($\alpha_r = 20°$) for ⟨010⟩ crystallographic orientation of single crystal aluminum

Figure 3.7 compares the predicted and experimental shear angles for single crystal copper and aluminum. The discrepancy between the experimental results and model predictions for T1 in Figure 3.7 (a) can be attributed to the errors in measuring the shear angles using scanning electron microscope (SEM) images as the dashed curve does not follow a four-fold symmetry. The cyclic behavior of the shear angles is well captured by the proposed model for T2, T3 and T4 in Figure 3.7 (b-d). While the peaks of both the experimental and simulation results are in phase and close in terms of amplitude, the valleys are more pronounced in the experimental data. This mismatch is often encountered in literature [73, 103, 134], where it seems that force predictions are always much more accurate than shear angles. One reason that may explain those differences is the experimental limitations of shear angle measurements in [11]. While the forces were measured using a dynamometer, the shear angles were visually estimated by analyzing single frames from a video recording. Although this method is more accurate than estimations based on chip thickness, it still relies on the observer's judgment and may introduce subjectivity.

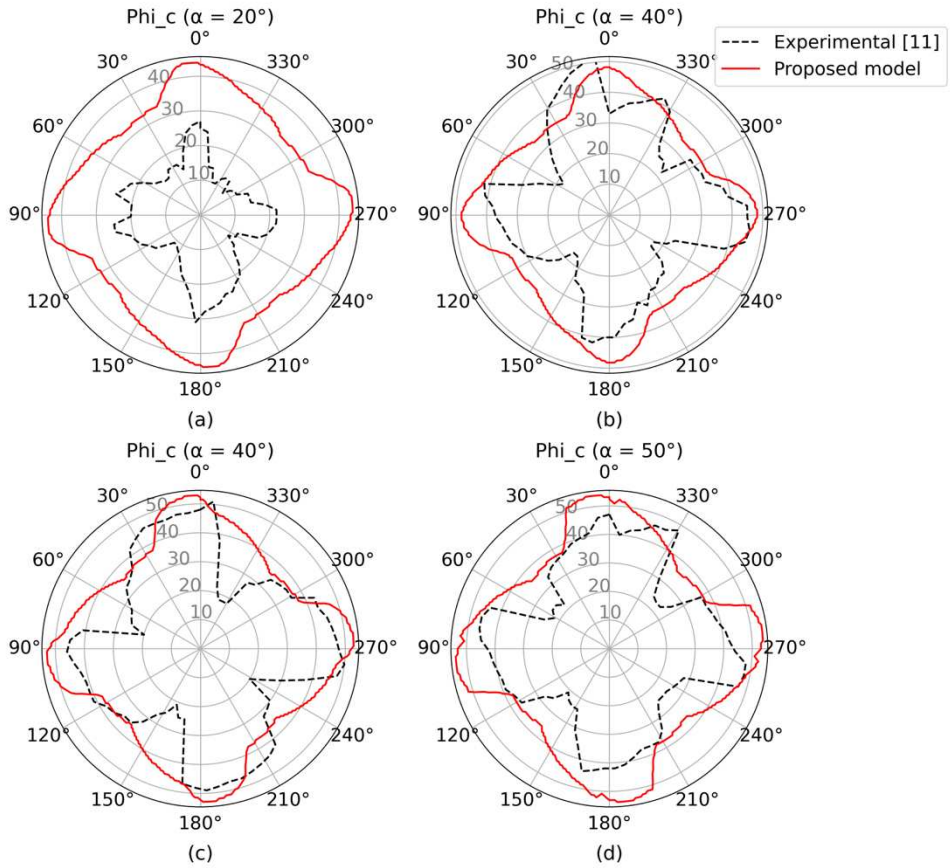


Figure 3.7 Comparison of the predicted and experimentally observed shear angles (°), (a) in T1 ($Cu - \alpha_r = 20°$), (b) in T2 ($Cu - \alpha_r = 40°$), (c) in T3 ($Al - \alpha_r = 40°$) and (d) in T4 ($Al - \alpha_r = 50°$)

Another reason that may explain the difference between the experimentally measured and predicted shear angles in (a) and (b) is the small variation of the total cutting power for a large range of shear angle candidates around the minimum cutting power as shown by Kota *et al.* [134]. Figure 3.8 shows the variation of the total cutting power $\dot{W}_{tot}$ with respect to the orientation and shear angles. The solid line represents the chosen shear angles minimizing the cutting power for each orientation angle. For an orientation angle, a small variation in the total cutting power results in a large variation in the shear angle and may explain the relatively large deviation observed between the experimental and predicted data. However, the cutting force coefficients, which depend on the cutting power, can still be predicted accurately since the cutting power does not show significant variations.

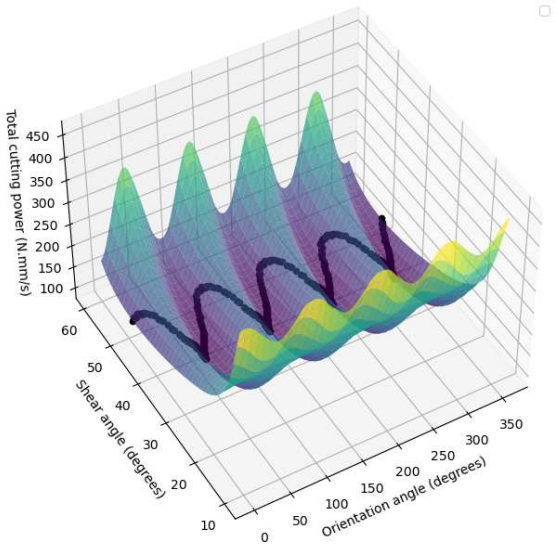


Figure 3.8 Variation of total cutting power with the orientation and shear angles in T2. The solid line shows the minimum total cutting power

3.5.2 Effect of cutting and geometric parameters

Once the proposed model is experimentally verified, the developed model has been used with different sets of machining parameters to study their influence on the tangential cutting force coefficient (K_{tc}) in orthogonal cutting of single crystal copper with the workpiece rotating around the ⟨010⟩ crystallographic zone axis. This analysis is not intended to represent real process tuning, but rather to assess the model's behavior with respect to key input parameters. All other cutting and geometric parameters remain the same as those used in the experiment T2. In Figure 3.9 (a), three different rake angles α_r (20°, 30° and 40°) are used. The increase in K_{tc} while decreasing the rake angle is clearly visible in the simulation results. A smaller rake angle forces the chip to bend more before being evacuated. On the contrary, a higher rake angle allows the chip to easily slide on the rake face and be evacuated easily. Figure 3.9 (b) shows the effect of the friction coefficient μ (0, 0.5 and 0.75) on the specific cutting pressure. As expected, when the friction coefficient between the chip and the rake face of the tool is low, the chip easily flows over the tool and the specific cutting pressure is lower than that of higher friction coefficients. Although the friction coefficient is not a direct process variable, it plays a critical role in defining the tool–chip interaction and depends on the material pair, lubrication conditions, and surface states. The model

also captures the increase in specific cutting pressure with decreasing uncut chip thickness (h), known as the size effect [151]. This effect is often attributed to the tool's cutting-edge radius, [152, 153]. Other causes of the size effect focus on the shear zone, and it has been experimentally observed [154] that the shear strain rate ($\dot{\gamma}$) is inversely proportional to the uncut chip thickness (h). The predictions of the proposed model also demonstrate the same relationship between $\dot{\gamma}$ and h (e.g., 0.2 mm and 0.1 mm uncut chip thicknesses respectively have average shear strain rates of 9.83 s^{-1} and 19.65 s^{-1}). Then, the tangential cutting force coefficient (K_{tc}) tends to increase when the uncut chip thickness is reduced, which is correctly predicted by the proposed model in Figure 3.9 (c), where the value of the uncut chip thickness varies between 0.2mm and 0.05 mm. While the model assumes a constant friction coefficient, Oxley's sliding-stick model and experimental observations [154] showed that the tool–chip contact zone becomes thinner as the uncut chip thickness decreases. This reduction in contact length, in practice, reduces the average friction at the interface. As this effect is not captured in the model, it may partially explain the overestimation of specific cutting pressure observed at low h.

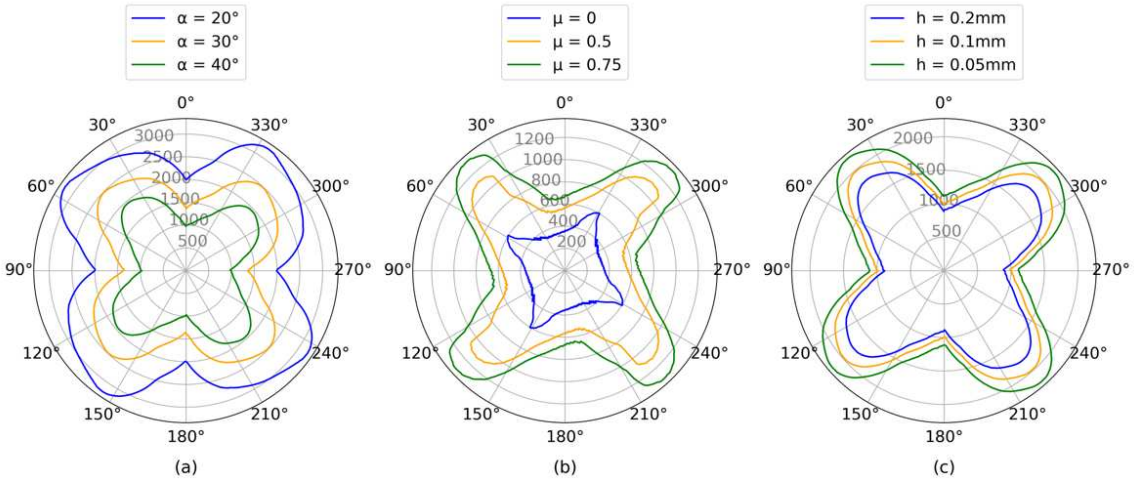


Figure 3.9 Influence of (a) the rake angle (α_r), (b) the friction coefficient (μ), (c) the uncut chip thickness (h), on the tangential cutting force coefficient (K_{tc}) (MPa)

Simulations are also run with different cutting speeds V (0.55mm/s, 250mm/s, 500mm/s and 1000mm/s). The experimental verification in Figure 3.5 was presented for the cutting speed used in [11] (0.55mm/s), which is slow enough to assume that the temperature in the cutting zone remains constant. However, this assumption cannot be kept for higher cutting speeds, hence the

temperature prediction model in the shear zone (Section 3.3.4) is used to consider the effect of thermal softening on the newly introduced J-C based hardening law. Thermal properties of single crystal copper [155] are given in Table 3.3. Cutting velocity has a direct influence on the shear strain rate (Eq. (3.18)), and in turn on the cutting forces and force coefficients but the thermal softening effect coming from the J-C hardening law moderates its impact on the machining response. Nevertheless, a 10% increase in K_{tc} is still visible in Figure 3.10 (a) when V goes from 250 to 1000mm/s, suggesting that the hardening effect from increased strain rate marginally surpasses the softening effect resulting from temperature rise as cutting speed increases. The assumption of a constant shear zone temperature in the experimental validation section (Section 3.5.1) is supported by Figure 3.10 (b), which shows that the temperature remains steady at 293 K for a cutting speed of 0.55 mm/s. The same conclusion has been found in [103]. For the three other cutting speeds, the temperature fluctuations follow the same trend as K_{tc}.

Table 3.3 Thermal properties of copper [155]

ρ (kg/m^3)	c_s (Nm/kg°C)	c_t (W/m°C)
8960	385	401

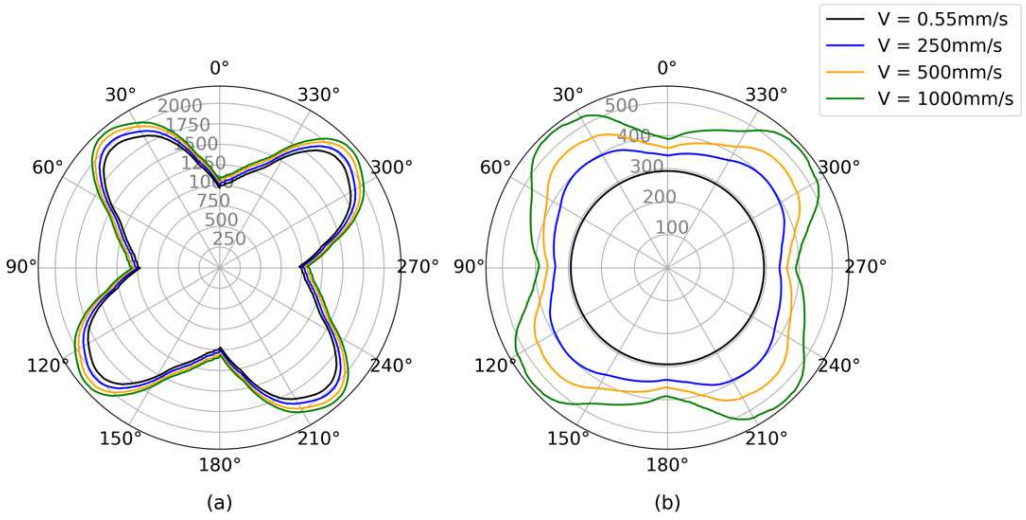


Figure 3.10 Influence of the cutting speed on (a) K_{tc} (MPa), (b) the temperature (K) in the shear zone

3.5.3 Crystallographic orientation

To study the effect of crystallographic orientation on the tangential cutting force coefficient (K_{tc}), four orientations (⟨010⟩, ⟨110⟩, ⟨111⟩, and ⟨112⟩) have been chosen to rotate around during the orthogonal turning operation of a copper single crystal. Figure 3.11 shows that the crystallographic orientation has a significant effect on the fluctuations of K_{tc}. The 2-fold symmetry is visible in ⟨110⟩ and ⟨112⟩, while 4-fold and 6-fold symmetries are respectively observed in ⟨010⟩ and ⟨111⟩.

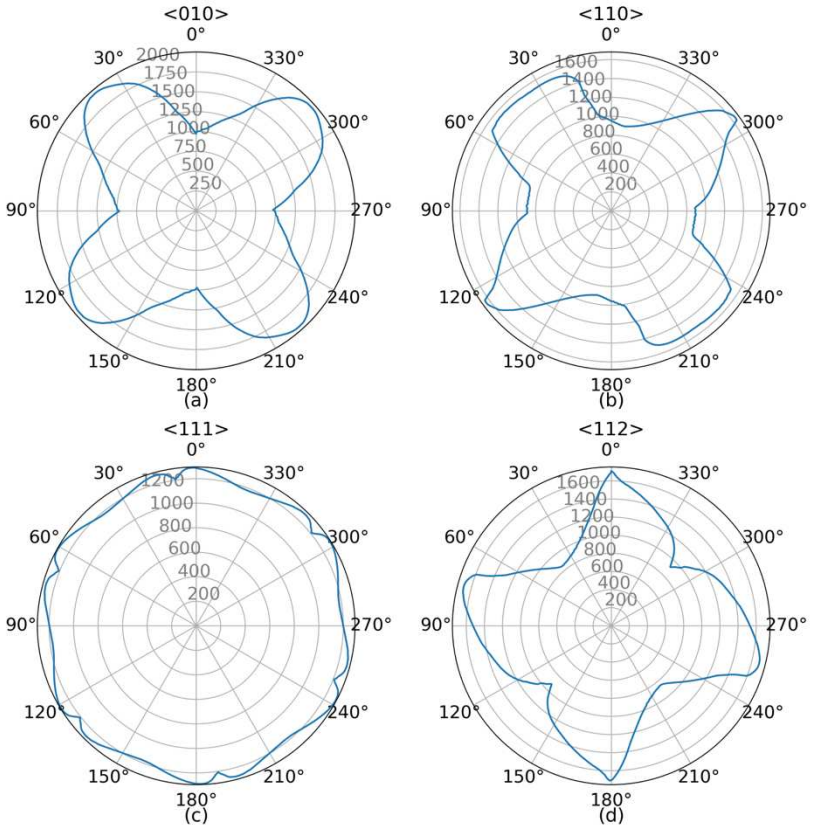


Figure 3.11 Influence of the crystallographic orientation on K_{tc}

The observed 2-fold, 4-fold, and 6-fold symmetries in machining an FCC metal arise from the activation of {111} ⟨110⟩ slip systems, where 2-fold symmetry results from slip asymmetry in orientations like ⟨112⟩, 4-fold symmetry in ⟨010⟩ reflects the 90° intersection of {111} planes, and 6-fold symmetry in ⟨111⟩ corresponds to the hexagonal arrangement of slip planes. The same conclusions can be drawn from the shear angle fluctuations in Figure 3.12.

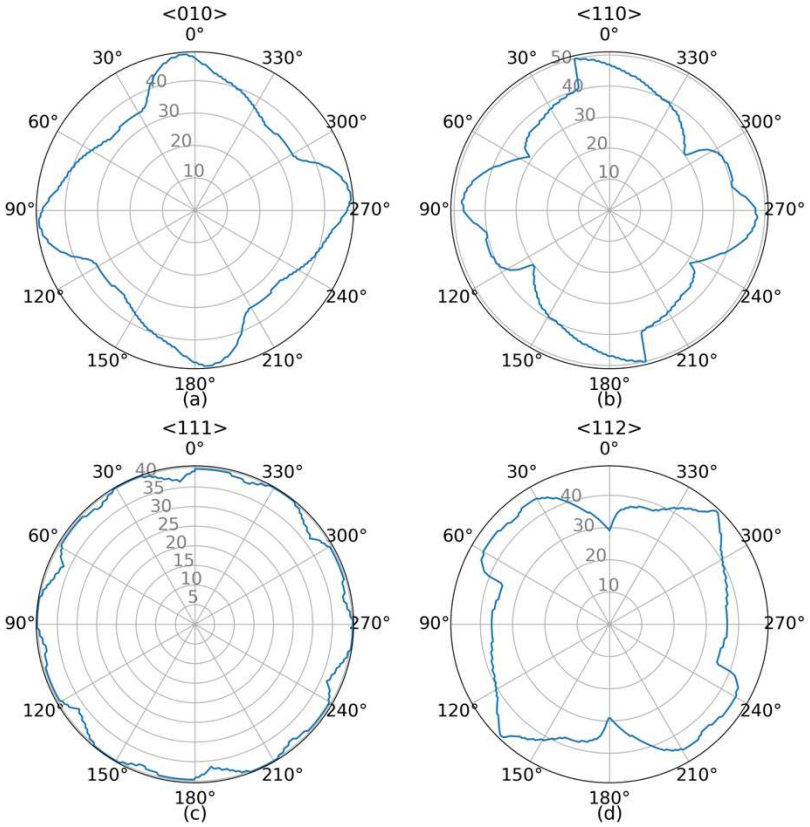


Figure 3.12 Influence of the crystallographic orientation on the shear angle

The ⟨010⟩ and ⟨112⟩ crystallographic directions correspond to the maximum and minimum value of K_{tc} (1953.34 MPa at 38° and 851.78 MPa at 44°) while the ⟨010⟩ and ⟨110⟩ directions exhibit the highest and lowest average specific cutting pressures (1479.8 MPa and 1218.6 MPa). This observation must be put in relation with the average cumulative slip ($\sum_\alpha|\gamma^\alpha|$) during a full rotation of the workpiece. Figure 3.13 shows that a higher average cumulative slip leads to a larger average value of K_{tc}. Indeed, orientations ⟨110⟩ and ⟨111⟩ require less active slip systems to accommodate the plastic deformation imposed by the shearing of the cutting process. Orientations ⟨010⟩ and ⟨120⟩ spread the deformation on more slip systems with a higher resulting cumulative slip and therefore a larger average value of K_{tc}. A comparison between the total number of activated slip systems and the amplitude of the specific cutting pressure fluctuations (Figure 3.11and Figure 3.13) reveals that a higher total number of activated slip systems during orthogonal cutting leads to more fluctuations in the specific cutting pressure (K_{tc}).

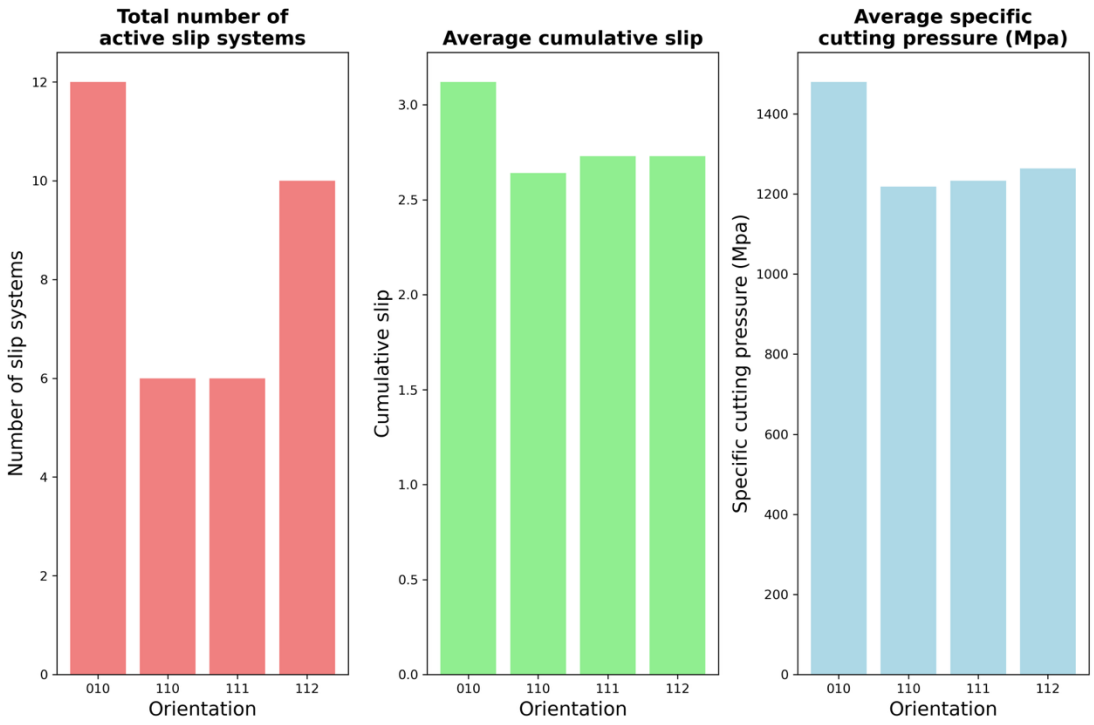


Figure 3.13 Total number of active slip systems, average cumulative shear and average specific cutting pressure (K_{tc}) during a full rotation of the cutting tool, with respect to the studied crystallographic zone axes

The crystallographic zone axis ⟨010⟩, which involves the biggest variations in K_{tc}, has also the highest total number of active slip systems (all 12 slip systems are activated at least once during one full rotation of the workpiece). On the contrary, the simulations around ⟨111⟩ and ⟨110⟩ crystallographic zone axes show lower cutting pressure variations with only 6 different slip systems activated in total.

Figure 3.14 illustrates the activated slip systems (Table 3.4) when cutting around the ⟨110⟩ crystallographic axis. Slip systems 3 and 6 are mainly activated when cutting along [001] and $[00\bar{1}]$ normal planes (a), slip systems 7 and 8 when cutting along $[\bar{1}11]$ and $[1\bar{1}\bar{1}]$ normal planes, and finally slip systems 10 and 11 when cutting along $[1\bar{1}1]$ and $[\bar{1}1\bar{1}]$ normal planes in the crystal reference.

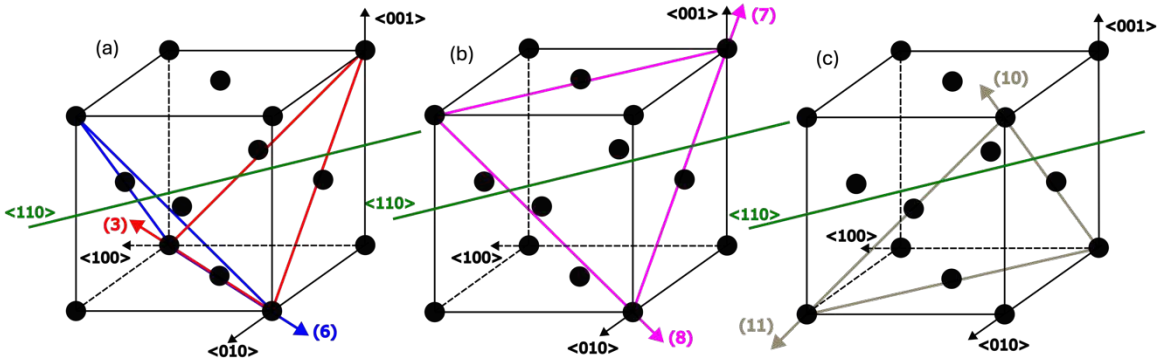


Figure 3.14 Illustration of the 6 slip systems involved when turning around the <110> crystallographic zone axis. Slip systems (a) 3 and 6, (b) 7 and 8, (c) 10 and 11

Table 3.4 Slip systems for FCC crystals. n_0^α and s_0^α are respectively the slip normal and the slip direction of the slip system α in the crystal reference

Slip system α	n_0^α	s_0^α
1	(111)	$[01\bar{1}]$
2		$[\bar{1}01]$
3		$[1\bar{1}0]$
4	$(\bar{1}\bar{1}1)$	$[0\bar{1}\bar{1}]$
5		$[101]$
6		$[\bar{1}10]$
7	$(1\bar{1}\bar{1})$	$[0\bar{1}1]$
8		$[\bar{1}0\bar{1}]$
9		$[110]$
10	$(\bar{1}1\bar{1})$	$[011]$
11		$[10\bar{1}]$
12		$[\bar{1}\bar{1}0]$

3.6 Conclusion

In this work, a temperature and rate sensitive, crystal plasticity-based machining mechanics model is proposed to predict the cutting force coefficients (and cutting forces) in orthogonal machining of single crystal materials. The model considers the influence of the rake angle, friction coefficient, uncut chip thickness, cutting speed, and crystallographic orientation on cutting force coefficients. The Cauchy stress tensor in the shear zone ($\boldsymbol{\sigma}$) is calculated using the theory of crystal plasticity with Johnson-Cook (J-C) phenomenological material constitutive model. The cutting temperature

and the shear strain rate dependencies are integrated into the hardening law using a crystal plasticity adapted form of J-C law for the first time in literature. The shear angle for each rotation angle of the workpiece is calculated by minimizing the total cutting power. A comparison between the predicted and experimentally identified cutting force coefficients shows that the proposed model can accurately predict the variation in the specific cutting pressures as the workpiece rotates in orthogonal turning process. Results reveal that crystallographic orientation strongly affects the magnitude of peaks and valleys of specific cutting pressures as the crystal orientation changes with respect to the cutting edge. The simulations results show that, the rake angle has the biggest impact on the specific cutting pressures while the friction coefficient is more influential than the uncut chip thickness and the cutting speed. In a future work, a general temperature prediction model [156] will be inserted to the proposed model, which will then be extended to other lattice structures, polycrystal anisotropic materials such as the additive manufactured components, and oblique cutting such as milling operations.

CHAPTER 4 CRYSTAL-BASED MACHINING MODEL EXTENSIONS

The analytical crystal-based machining model developed in the previous chapter only handles two-dimensional orthogonal cutting simulations on FCC single crystals. However, single crystals are not common materials and are used for very specific applications such as turbine blades in aerospace industry. In addition, FCC lattice type is just one of the three main lattice structures (FCC, BCC and HCP), and most of the common industrial machining processes are oblique (three-dimensional) cutting. These limitations hinder the use of the developed force prediction model for cutting operations on AMed parts in Chapter 3. AMed materials are usually polycrystals and often contain several phases of different lattice structures. In this chapter, the developed crystal-plasticity based machining mechanics model is first extended to BCC and HCP lattice structures, and then oblique cutting and milling kinematics are integrated into the model. A homogenization method is also used to simulate the flat end-milling operations on polycrystals. The performance of the adapted model is experimentally verified with milling tests conducted on an AMed thin-walled part made of AISI 316L stainless steel, and the predicted cutting forces are compared with those of the wrought counterpart.

4.1 Body-centered cubic (BCC) and hexagonal close-packed (HCP) lattice structures

Body-centered cubic (BCC) and hexagonal close-packed (HCP) lattice structures are very common in various metal alloys. For example, BCC lattice structures can be found in ferritic stainless steels but also in the β phase of titanium alloys while HCP lattice structures constitute the primary α grains in titanium. As mentioned in Section 2.2.3, the plastic deformation in single/polycrystalline materials results from the movement of dislocations at the crystal level. These dislocations cause slip along some preferred planes and directions in the crystal which are characterized by a high planar density and a directional close packed atomic arrangement. Unlike in FCC structures, BCC does not have evident most densely packed planes to clearly define the set of slip systems involved when the material deforms plastically. Hull [157] identified the $\{110\}$ and $\{112\}$ plane families as the primary slip planes, with $\{110\}$ being more favorable at low temperatures. Slip can also occur on $\{123\}$ and non-crystallographic planes. They are less dominant, primarily activated at elevated temperatures [158] and often neglected [159, 160]. However, accounting for the high-strain-rate nature of machining and the heat generated in the shear zone as well as in the chip/tool interface,

all three slip system families ($\{110\}\langle 111\rangle$, $\{112\}\langle 111\rangle$ and $\{123\}\langle 111\rangle$) are considered in this study (Figure 4.1 and Table 4.1).

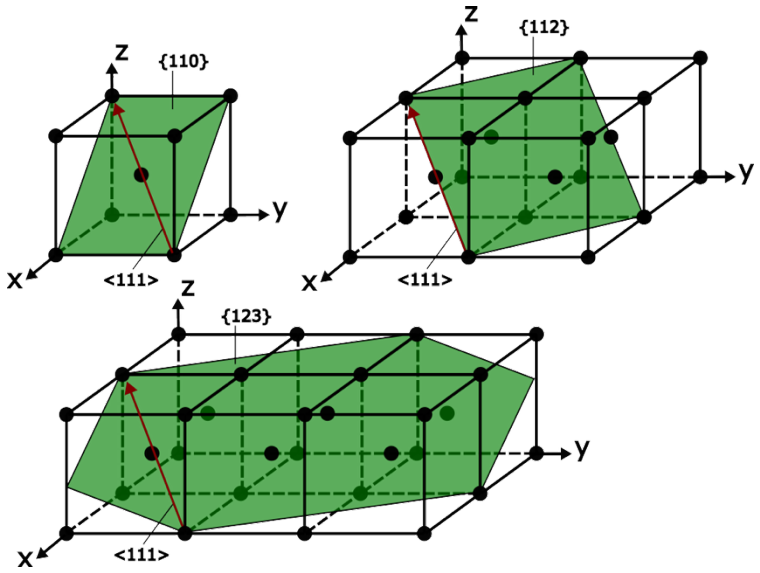


Figure 4.1 Schematic representation of slip systems in BCC crystals

Table 4.1 Deformation modes of BCC lattice structures

Slip plane	Slip direction	Number of systems
$\{110\}$	$\langle 111\rangle$	12
$\{112\}$		12
$\{123\}$		24

Since 48 BCC slip systems are composed of three plane families ($\{110\}, \{112\}$ and $\{123\}$), the slip resistance of these planes can be different. In addition, the shear strength on $\{112\}$ and $\{123\}$ planes depends on the sign of the shear strain applied [161], which implies defining several critical resolved shear stress values in the model while a single value was enough for FCC materials. However, since BCC and FCC are just variants of the primitive cubic or simple cubic lattice structure, they have the same crystallographic coordinate system and the transformation matrix in Eq. (3.11) can be used to transform BCC slip systems in the frame of the sample.

HCP lattice structures are different from FCC and BCC because they rely on their own coordinate system (see Section 2.2.2). In addition, because of a strong plastic anisotropy and the possibility of

twinning [162], HCP lattice structures have complex deformation modes. Twinning is a deformation mode at the crystal level where unit cells rearrange themselves in another orientation, creating new grain boundaries (Figure 4.2).

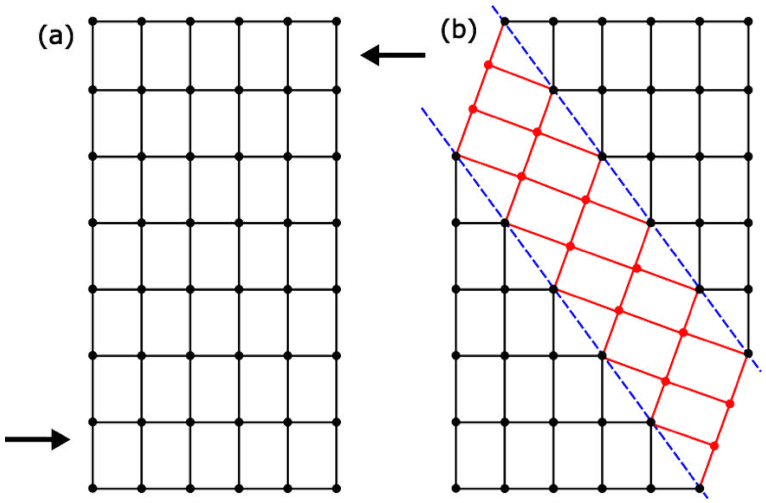


Figure 4.2 2D representation of the twinning effect. Lattice configuration, (a) before the shear load is applied, (b) after the shear with two new grain boundaries

Five types of slip systems are commonly reported to occur on four distinct slip planes: basal $\{0001\}\langle 11\bar{2}0\rangle$, prismatic <a> $\{1\bar{1}00\}\langle 11\bar{2}0\rangle$, pyramidal <a> $\{1\bar{1}01\}\langle 11\bar{2}0\rangle$, first order pyramidal <c+a> $\{1\bar{1}01\}\langle\bar{1}2\bar{1}3\rangle$, and second order pyramidal <c+a> $\{2\bar{1}\bar{1}2\}\langle\bar{2}113\rangle$ as shown in Figure 4.3 and Table 4.2.

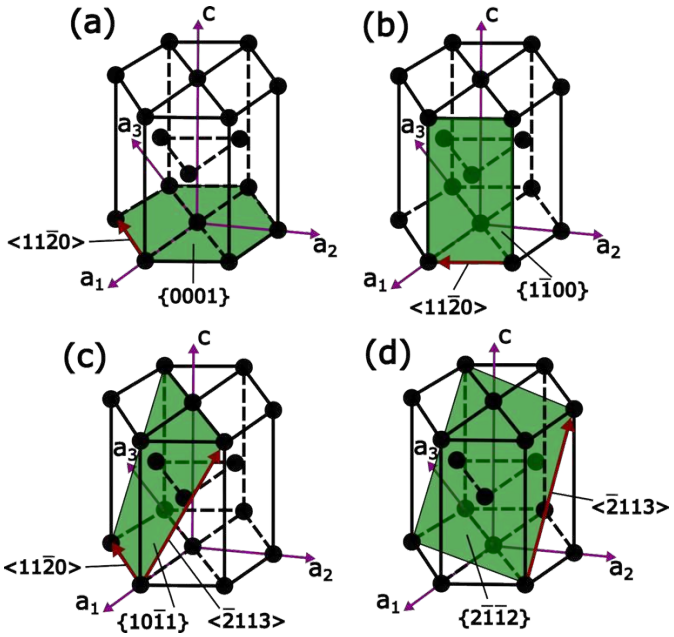


Figure 4.3 Schematic representation of slip systems in HCP crystals. (a) Basal, (b) Prismatic <a>, (c) Pyramidal <a> and first order Pyramidal <c+a>, (d) second order Pyramidal <c+a>

Table 4.2 Deformation modes of HCP lattice structures

Deformation mode	Slip plane	Slip direction	Number of systems
Basal	$\{0001\}$	$\langle 11\bar{2}0 \rangle$	3
Prismatic <a>	$\{1\bar{1}00\}$		3
Pyramidal <a>	$\{1\bar{1}01\}$		6
f.o. Pyramidal <c+a>	$\{1\bar{1}01\}$	$\langle \bar{1}2\bar{1}3 \rangle$	12
s.o. Pyramidal <c+a>	$\{2\bar{1}\bar{1}2\}$		6

The twinning deformation mode usually occurs at low temperature and high strain rates [163]. Even though machining involves high shear strain rate deformations, the temperature is also elevated especially in thermally resistant metals such as titanium- and nickel-based superalloys. Consequently, only slip deformations are considered in this thesis, with 30 slip systems presented above as it was done in literature [104]. Moreover, although twinning is commonly observed in unalloyed titanium and certain α/β Ti–Al alloys, its occurrence tends to diminish as the aluminum

content increases to the point that it is almost never observed in Ti-Al alloys containing 6% aluminum like Ti-6Al-4V [164].

To implement HCP slip systems in the developed machining model, slip planes and slip directions must be converted from the Miller-Bravais coordinates system (a_1, a_2, a_3, c) to the cubic coordinates system in the crystal frame (x', y', z') as shown in Figure 4.4.

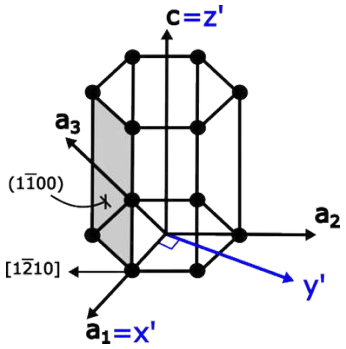


Figure 4.4 Miller-Bravais coordinate system (a_1, a_2, a_3, c) against cubic coordinate system (x', y', z') in an HCP lattice

The transformation equations between the Miller-Bravais and cubic coordinate systems for a slip direction (Eq. (4.1)) and a plane normal (Eq. (4.2)) are given as follows:

$$\begin{cases} x' = \frac{3}{2} a_1 \\ y' = (a_1 + 2a_2) \times \frac{\sqrt{3}}{2} \\ z' = c \times r \end{cases} \tag{4.1}$$

$$\begin{cases} x' = a_1 \\ y' = (a_1 + 2a_2) \times \frac{1}{\sqrt{3}} \\ z' = \frac{c}{r} \end{cases} \tag{4.2}$$

where r is the ratio between the dimensions of a cell unit along the c and a axes. Then, the same frame transformation between the global and crystal frames used for FCC and BCC lattices can be applied (Eq. (3.12)).

4.2 Flat end-milling process modelling

Flat end mills are cutting tools characterized by a flat bottom, typically with 90° angle. They are mainly used to create sharp edges, flat surfaces and square-bottomed slots with pockets, slots, facing and contouring milling operations. In this section, the flat end-milling geometry, kinematics, cutting parameters and cutting forces are presented.

4.2.1 Mechanics of helical end mills

Modeling the milling forces is based on the discretization approach [29]. The milling tool is characterized by its number of flutes (N), a constant helix angle (i) and its diameter (D) as shown in Figure 4.5. The cutting conditions are given by the spindle rotation speed (n), the axial depth of cut (a_p) the feed rate (f_c) and the immersion angles (ϕ_{st}) and (ϕ_{ex}). The cutter rotates with small incremental angles ($\Delta\phi$).

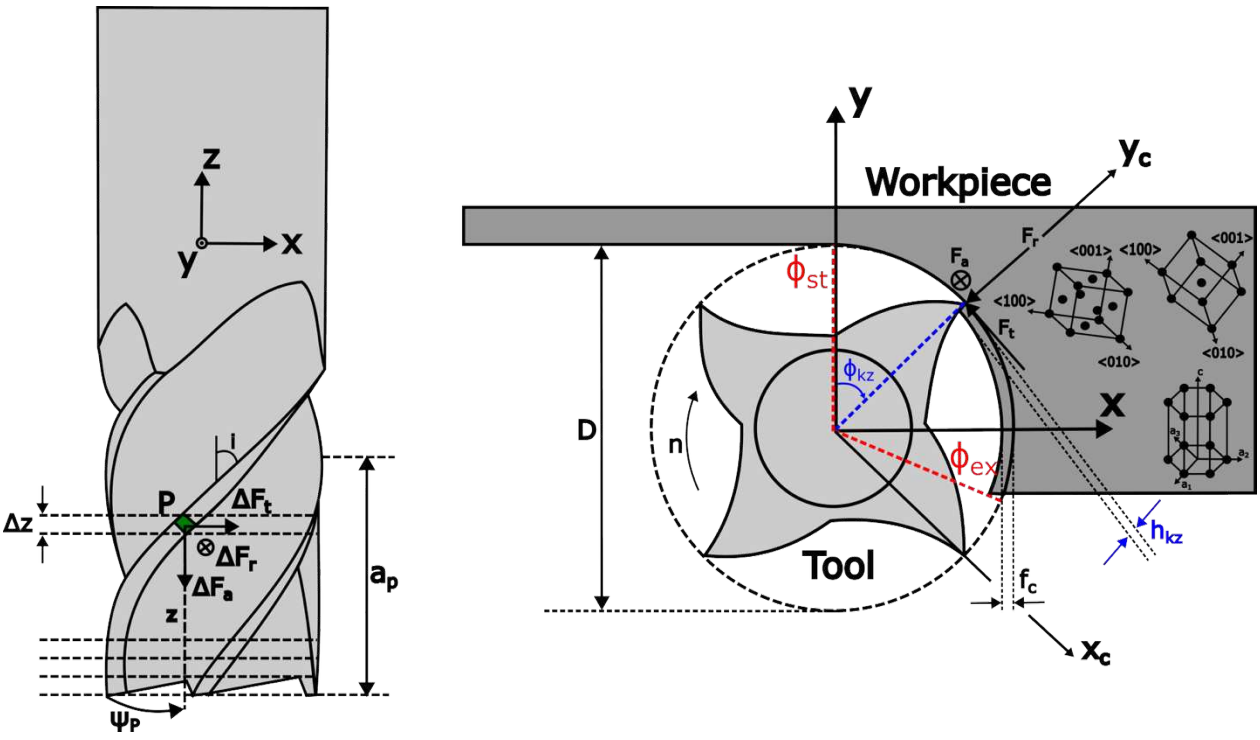


Figure 4.5 Geometry of the milling tool and direction of cutting forces

With each incremental rotation, integration of the cutting forces is performed over the axial differential flute elements, from the tool tip to the depth of cut. The angular position of the k^{th} flute at the height z from the tip of the tool is given by:

$$\phi_{k,z} = \theta + (k-1)\phi_p - \psi(z) = \theta + (k-1)\frac{2\pi}{N} - \frac{2z\tan(i)}{D} \tag{4.3}$$

where θ and ϕ_p are respectively the current rotation and pitch angles of the milling tool, and $\psi(z)$ is the lag angle, representing the angular position lag between the bottom of the k^{th} flute and the axial increment of the same flute located at the height z. The chip thickness (h_{kz}) cut by this portion of the k^{th} flute is defined as:

$$\begin{cases} f_c \sin(\phi_{k,z}) & \text{if } \phi_{st} < \phi_{k,z} < \phi_{ex} \\ 0 & \text{otherwise} \end{cases} \tag{4.4}$$

The incremental values of the cutting forces in tool's local frame (t, r, a) shown in Figure 4.5 are calculated as:

$$\Delta F_{t,r,a} = \Delta z \left(K_{t,r,a\,c}\, h_{kz} + K_{t,r,a\,e} \right) \tag{4.5}$$

where $\Delta F_{t,r,a}$, $K_{t,r,a\,c}$ and $K_{t,r,a\,e}$ are respectively the cutting force increment, the cutting and edge force coefficient and Δz is the height of an axial differential element. The edge forces are not considered in this work as the proposed model assumes perfectly sharp cutting tool. $\Delta F_{t,r,a}$ is then transformed into the global frame (x, y, z) as:

$$\begin{bmatrix} \Delta F_x \\ \Delta F_y \\ \Delta F_z \end{bmatrix} = \begin{bmatrix} -\sin(\phi_{k,z}) & -\cos(\phi_{k,z}) & 0 \\ -\cos(\phi_{k,z}) & \sin(\phi_{k,z}) & 0 \\ 0 & 0 & -1 \end{bmatrix} \begin{bmatrix} \Delta F_r \\ \Delta F_t \\ \Delta F_a \end{bmatrix} \tag{4.6}$$

The cutting forces in the global frame are obtained by summing the force increments over axial engagement of the tool with the workpiece material.

4.2.2 Oblique cutting

Discretization of the helical cutting edge transforms its complex geometry into multiple small-scale oblique cutting elements. For each element, the primary shear zone can be considered a thick deformation zone inclined at the normal shear angle ϕ_n with respect to the cutting velocity direction. The force acting on the shear plane is derived from Merchant's geometry [9] as follows:

$$F_s = F_c \left[\cos(\theta_n + \phi_n)\cos(\theta_i)\cos(\phi_i) + \sin(\theta_i)\cos(\phi_i)\right] \tag{4.7}$$

$$F_c = \sqrt{F_x^2 + F_y^2 + F_z^2} \tag{4.8}$$

where F_c is the resultant cutting force, (θ_n, θ_i) is the direction of the resultant force vector $\overrightarrow{F_c}$, and ϕ_i is the oblique shear angle. θ_n and θ_i are calculated as,

$$\begin{cases} \theta_n = tan^{-1}(\tan(\beta_a) \times \cos(\eta)) - \alpha_n \\ \theta_i = sin^{-1}(\sin(\beta_a) \times \sin(\eta)) \end{cases} \tag{4.9}$$

where, α_n is the normal rake angle, β_a is the friction angle and η is the chip flow angle derived as,

$$\eta = tan^{-1}\left(\frac{\tan(i)\cos(\phi_n - \alpha_n) - \cos(\alpha_r)\tan(\phi_i)}{\sin(\phi_n)}\right) \tag{4.10}$$

The geometric parameters $(\phi_n, \phi_i, \theta_n, \theta_i, i$ and $\eta)$ and the cutting parameters $\left(h, a_p, V\right)$ are illustrated in Figure 4.6.

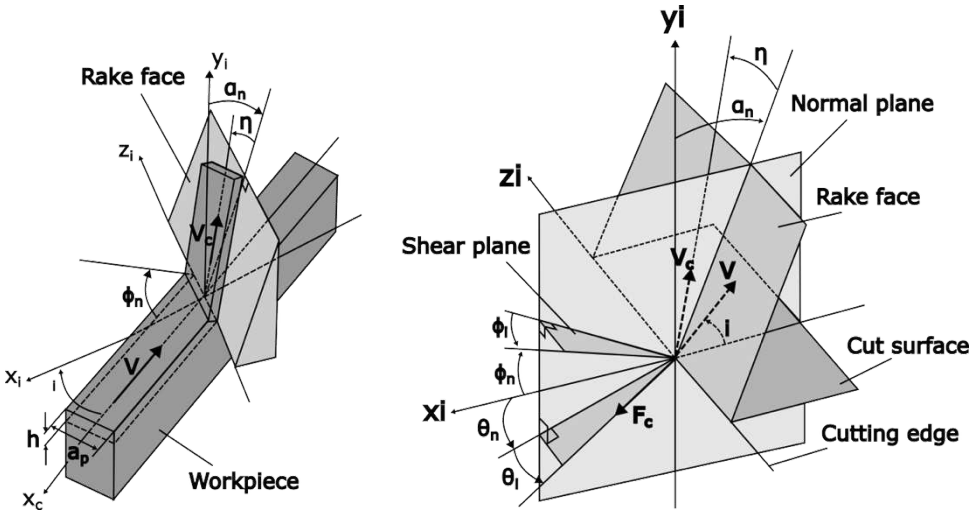


Figure 4.6 Geometry of the oblique (3D) cutting process. Reproduced from [29]

The shear force is then used to calculate the three-dimensional specific cutting pressures K_{tc}, K_{rc} and K_{ac}, which are respectively the tangential, radial and axial cutting force coefficient,

$$\begin{cases} K_{tc} = \dfrac{\cos(\theta_n) + \tan(\theta_i)\tan(i)}{\cos(\theta_n + \phi_n)\cos(\phi_i) + \tan(\theta_i)\sin(\phi_i)} \dfrac{F_s\cos(i)}{a_p h} \\ K_{rc} = \dfrac{\sin(\theta_n)}{[\cos(\theta_n + \phi_n)\cos(\phi_i) + \tan(\theta_i)\sin(\phi_i)]\cos(i)} \dfrac{F_s\cos(i)}{a_p h} \\ K_{ac} = \dfrac{\tan(\theta_i) - \cos(\theta_n)\tan(i)}{\cos(\theta_n + \phi_n)\cos(\phi_i) + \tan(\theta_i)\sin(\phi_i)} \dfrac{F_s\cos(i)}{a_p h} \end{cases} \tag{4.11}$$

The shear force is calculated by multiplying the shear stress τ_s acting on the shear plane with the shear plane area A_s using Eqs. (3.5) and (3.6). The shear area depends both on the normal ϕ_n and inclination angle i and is calculated as,

$$A_s = \frac{h\, a_p}{\sin(\phi_n)\cos(i)} \tag{4.12}$$

The same temperature- and rate-sensitive crystal plasticity model described in Section 3.4 is used to obtain the Cauchy stress tensor $\boldsymbol{\sigma}$ in the shear zone, which is then used to calculate the shear stress τ_s in Eq. (3.6) for a given couple (ϕ_n, ϕ_i). The total cutting power $\dot{W}_{tot}$ is then evaluated as,

$$\dot{W}_{tot} = F_c\, V\, [\cos(\theta_i)\cos(\theta_n)\cos(i) + \sin(\theta_i)\sin(i)] \tag{4.13}$$

The normal and oblique shear angles are evaluated by minimizing the total cutting power in the shear plane for a range of candidates ($\phi_n \in \left[0,\ \frac{\pi}{2} - (\beta_a - \alpha_n)\right]$ and $\phi_i \in [0,\ i]$).

To consider the crystallographic orientation in the evaluation of the Cauchy stress $\boldsymbol{\sigma}$ in the shear plane, the slip planes and directions of the crystal must be expressed in the shear frame. In Section 3.3.2, the crystal orientation has been converted into the global frame (x, y, z) with Eq. (3.11); this equation is applied again in oblique cutting. Each infinitesimal cutting edge element resulting from the axial discretization of the milling tool has an orientation described with its rotation angle ϕ_{kz} and a constant inclination angle i. The transformation matrix between the global frame (x, y, z) and the cutting frame $(x_c, y_{c,} z_c)$ is defined using the angular location of the infinitesimal cutting edge in the engagement zone as,

$$\boldsymbol{T}_{global \to cutting} = \begin{bmatrix} \cos(\phi_{kz}) & -\sin(\phi_{kz}) & 0 \\ \sin(\phi_{kz}) & \cos(\phi_{kz}) & 0 \\ 0 & 0 & 1 \end{bmatrix} \tag{4.14}$$

Then, the transformation between the cutting frame $(x_c, y_{c,} z_c)$ and the inclined frame $(x_i, y_{i,} z_i)$ characterized by the inclination angle $(i > 0)$ is described as,

$$\boldsymbol{T}_{cutting \to inclined} = \begin{bmatrix} \cos(i) & 0 & \sin(i) \\ 0 & 1 & 0 \\ -\sin(i) & 0 & \cos(i) \end{bmatrix} \tag{4.15}$$

The transformation from the inclined frame $(x_i, y_{i,} z_i)$ to the shear plane frame $(x_{sp}, y_{sp,} z_{sp})$ is given by,

$$\boldsymbol{T}_{inclined\rightarrow sp} = \begin{bmatrix} \cos(\phi_n) & \sin(\phi_n) & 0 \\ -\sin(\phi_n) & \cos(\phi_n) & 0 \\ 0 & 0 & 1 \end{bmatrix} \tag{4.16}$$

Finally, the shear direction frame is rotated by a positive oblique shear angle ϕ_i with respect to y_{sp}:

$$\boldsymbol{T}_{sp\rightarrow sd} = \begin{bmatrix} \cos(\phi_i) & 0 & -\sin(\phi_i) \\ 0 & 1 & 0 \\ \sin(\phi_i) & 0 & \cos(\phi_i) \end{bmatrix} \tag{4.17}$$

To calculate the shear stress of the material, all quantities and crystal plasticity equations are derived in the shear direction reference coordinate system. The transformation matrix from the crystal frame to the shear direction frame is calculated as,

$$\boldsymbol{R}_{milling} = \boldsymbol{T}_{sp\rightarrow sd}\, \boldsymbol{T}_{inclined\rightarrow sp}\, \boldsymbol{T}_{cutting\rightarrow inclined}\, \boldsymbol{T}_{global\rightarrow cutting}\, \boldsymbol{T}^{T}_{global\rightarrow \frac{FCC}{BCC}} \tag{4.18}$$

4.2.3 Shear and shear strain rate

The shear strain γ occurring in the shear plane is geometrically defined as the ratio between the shear increment Δs and the shear zone thickness Δd as illustrated in Figure 4.7.

$$\gamma = \frac{\Delta s}{\Delta d} = \frac{\cos(\alpha_n)}{\sin(\phi_n)\cos(\phi_n - \alpha_n)\cos(\phi_i)} \tag{4.19}$$

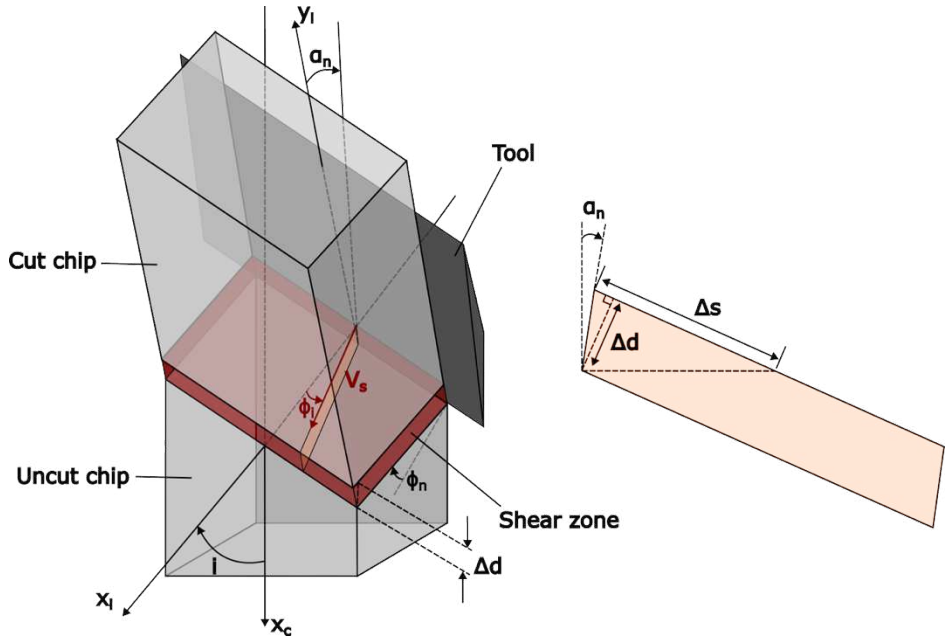


Figure 4.7 Geometry of the deformation in the shear zone in oblique cutting

The shear velocity geometrically corresponds to the speed at which the shear increment Δs occurs and is evaluated as:

$$V_s = \frac{\Delta s}{\Delta t} = \frac{V\cos(\alpha_n)\cos(i)}{\cos(\phi_n - \alpha_n)\cos(\phi_i)} \tag{4.20}$$

The shear strain rate can now be calculated as,

$$\dot{\gamma} = \frac{\gamma}{\Delta t} = \frac{1}{\Delta d}\frac{\Delta s}{\Delta t} = \frac{V_s}{\Delta d} = \frac{V\cos(\alpha_n)\cos(i)}{\Delta d\cos(\phi_n - \alpha_n)\cos(\phi_i)} \tag{4.21}$$

The shear zone thickness is generally approximated as a fraction of the shear plane length (L_c) [29]:

$$\Delta d = k\,L_c \qquad k \in [0.15; 0.2] \tag{4.22}$$

where L_c is a function of the axial depth of cut a_p, the normal ϕ_n and oblique ϕ_i shear angles,

$$L_c = \frac{h}{\sin(\phi_n)\cos(\phi_i)} \tag{4.23}$$

4.2.4 Temperature rise in the shear zone

To account for the temperature rise in the shear zone caused by the milling process, the approach developed in Section 3.3.4 for orthogonal cutting (Eqs. (3.21)-(3.23)) is adapted to oblique cutting by using the normal shear angle ϕ_n [165] in Eq. (2.22) as,

$$\begin{cases} \lambda_s = 1 \quad \text{for } 0 \leq R_T \tan(\phi_n) \leq 0.04 \\ \lambda_s = 0.5 - 0.35 \log(R_T \tan(\phi_n)) \quad \text{for } 0.04 \leq R_T \tan(\phi_n) \leq 10 \\ \lambda_s = 0.3 - 0.15 \log(R_T \tan(\phi_n)) \quad \text{for } R_T \tan(\phi_n) \geq 10 \end{cases} \tag{4.24}$$

4.2.5 Macro-scale deformation

The kinematics equations of the elastic-plastic deformation in the shear zone during the milling process are identical to the ones developed in Section 3.4. Only the expression of the deformation gradient $\boldsymbol{F}$ changes to match the shear direction frame defined in Eq. (4.17):

$$\boldsymbol{F} = \begin{bmatrix} 1 & \dot{\gamma} t & 0 \\ 0 & 1 & 0 \\ 0 & 0 & 1 \end{bmatrix} \tag{4.25}$$

4.3 Polycrystal materials

In machining of polycrystalline materials, the tool edge cuts along several grains or phases with different lattice arrangements and crystallographic orientations at the same time. This is particularly true for titanium alloys which contain two different phases (α and β) with two different lattice structures (HCP and BCC). To handle the challenge of considering all the phases of the material with their respective crystallographic orientations, a homogenization method (Figure 4.8) is used to approximate the microstructure of the material as an equivalent homogenous crystal.

In this study, it is assumed that the total shear strain is the same for every phase φ_{ij} contained in the homogenization volume v_i [104, 105]:

$$\boldsymbol{F}_i = \boldsymbol{F}_{\varphi_{ij}} \tag{4.26}$$

where $\boldsymbol{F}_i$ and $\boldsymbol{F}_{\varphi_{ij}}$ are respectively the deformation gradients of v_i and of each phase φ_{ij} in v_i.

The crystal plasticity kinematics equations (Eqs. (3.24)-(3.46)) are solved independently for each different phase contained in v_i, and a Cauchy stress tensor $\boldsymbol{\sigma}_{\varphi_{ij}}$ is calculated for each of them.

Then, a homogenized Cauchy stress $\boldsymbol{\sigma}_i$ is evaluated by summing the $\boldsymbol{\sigma}_{\varphi_{ij}}$ values, each weighted by the volume fraction $v_{\varphi_{ij}}$ of the corresponding phase,

$$\boldsymbol{\sigma}_i = \sum_j v_{\varphi_{ij}} \boldsymbol{\sigma}_{\varphi_{ij}} \tag{4.27}$$

The shear force resulting from the homogenized stress in the shear plane (Eqs. (3.5)-(3.6)) is used to evaluate the total cutting power (Eq. (4.13)) for a given couple of ϕ_n and ϕ_i. After the work minimization, a single couple (ϕ_n, ϕ_i) is retained for each homogenization volume considered. A single set of cutting force coefficients (K_{tc}, K_{rc} and K_{ac}) is calculated for the homogenized equivalent crystal in v_i. If several orientation maps are obtained with electron backscatter diffraction (EBSD) measurements, different sets of cutting force coefficients can be calculated and interpolated to consider changes in the material microstructure along the axis of the tool (axial depth of cut). Cutting force coefficients are then incorporated into the milling mechanics model (Eqs. (4.3)-(4.6)) to evaluate the cutting forces.

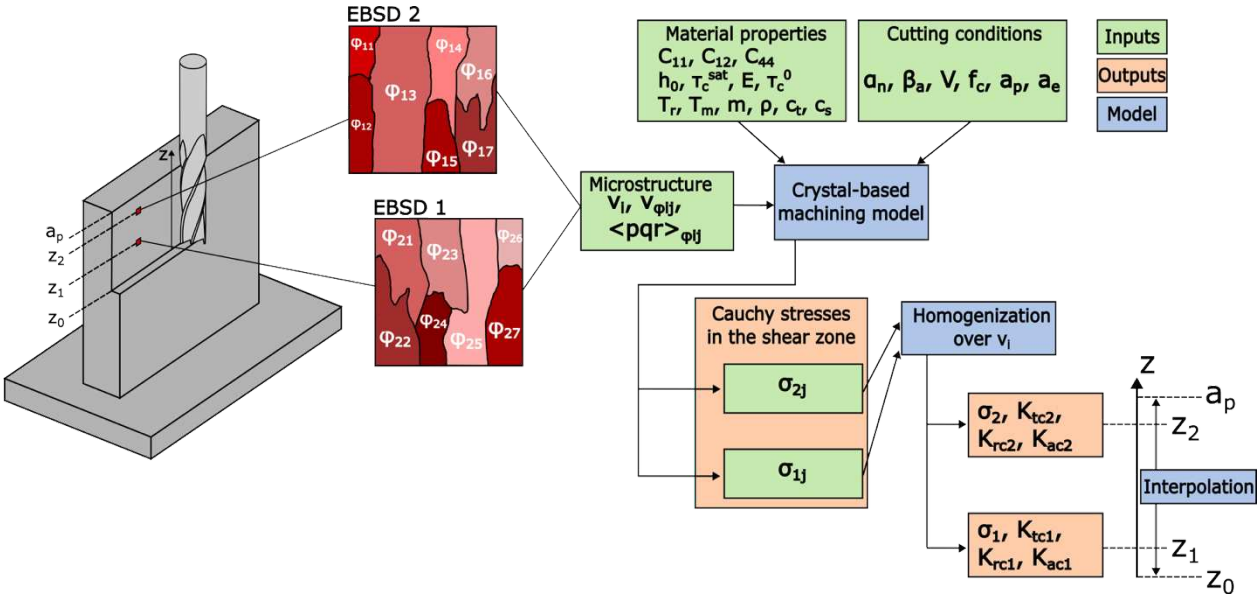


Figure 4.8 Illustration of the homogenization method with two EBSD measurements along the axis of the tool

4.4 Experimental verification

In this section, the experimental setup and the verification results for the proposed extended model are presented. A thin-walled plate geometry made of AISI 316L stainless steel (FCC metal) is used as the workpiece. A plate fabricated with Wire Laser Additive Manufacturing (WLAM) method and another one made of wrought AISI 316L are machined with the same cutting tool and machining conditions to compare their cutting forces. First, a microstructure analysis is carried out using EBSD, which is used in homogenisation calculations (Eqs. (4.26)-(4.27)). Then, machining experiments are conducted using a three-component table dynamometer (Kistler 9255B002) to measure the cutting forces during machining.

4.4.1 Fabrication of the AISI 316L thin-walled part via WLAM

The test piece is produced with WLAM. WLAM uses a laser to concentrate a heat beam and melt the material, which is supplied in wire form [166] as represented in Figure 4.9.

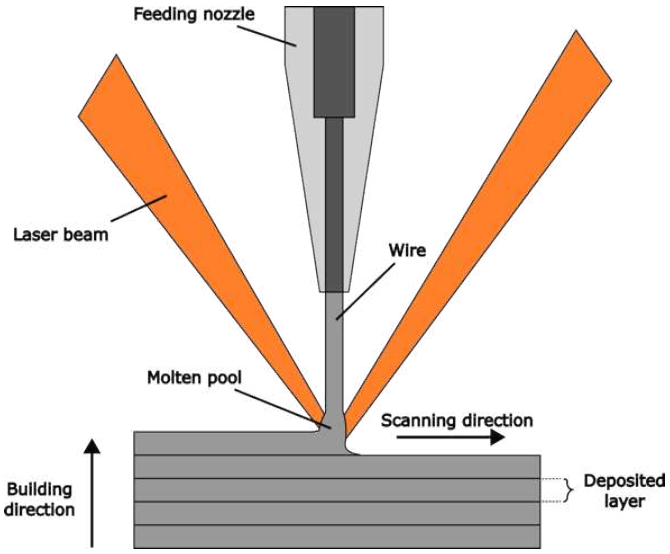


Figure 4.9 Illustration of the WLAM process

A single-layered thin-walled plate of 62×40×8 mm (Figure 4.10) was built upon a wrought substrate in the same AISI 316L alloy using an ABB hybrid cell for the deposition of the metal. It was equipped with an ABB IRBP A-250 tilt table, a Coaxworks head mounted on an ABB IRB4600 robot and powered by an Ytterbium fiber laser source with a maximum power of 4 kW. The RCC-M code specification for AISI 316L [167] are presented in Table 4.3.

Table 4.3 RCC-M code specifications for AISI 316L [167]

%Cr	%Mo	%Si	%Ni	%Mn	%C	%Cu	%N	%P	%S
16-19	2-2.5	<1	10-14	<2	<0.03	<1	-	<0.03	<0.015

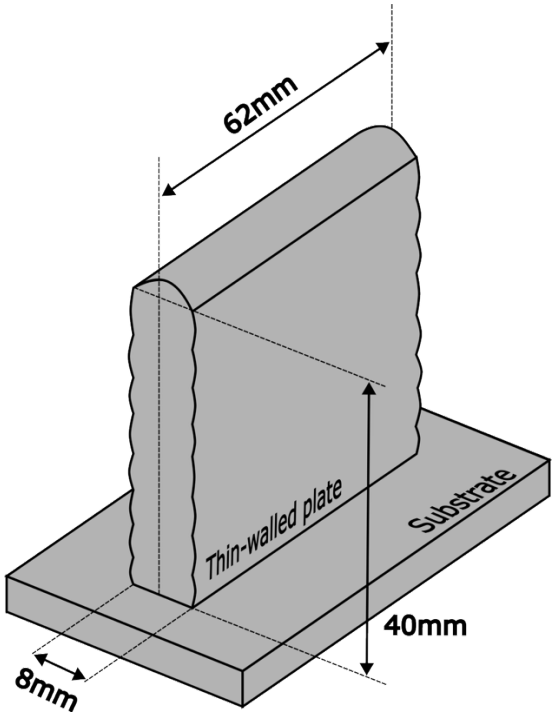


Figure 4.10 Dimensions of the WLAM produced thin-walled plate

4.4.2 Microstructure characterization

For the microstructure analysis, samples of both the AMed and wrought parts are cut out from the top-left corner the workpieces (Figure 4.11). The dimensions of the samples are approximately 10×10×3 mm with the main faces oriented toward the transverse direction (TD) as shown in Figure 4.11. They were hot-mounted in a press using a mix of thermoplastic and conductive resin for the scanning electron microscope (SEM) examination. A polishing preparation was performed on all the samples, starting from conventional polishing (Bruehler MetaServ 250) with diamond pastes, then with 9 µm diamond solution (Struers TegraForce-5) and finishing with 15 hours of vibro-polishing (Bruehler Vibromet 2) in 0.05 µm masterprep alumina solution. After polishing, the samples are cleaned with an ethanol solution. EBSD analyses are performed on a field emission SEM (Jeol JSM-IT810) equipped with Aztec and AztecCrystal EBSD softwares (Oxford

Instruments, UK). The orientation maps are obtained in the middle of the main face of the samples, and their dimensions are 266×200 µm. The data acquisition is performed using an acceleration voltage of 20 kV, a working distance of approximately 20 mm, and a nominal beam current of 2 nA. Microstructure orientation maps are obtained with a rate of zero-solution below 3% and a slight post-acquisition processing (clean-up) is applied before exporting the results.

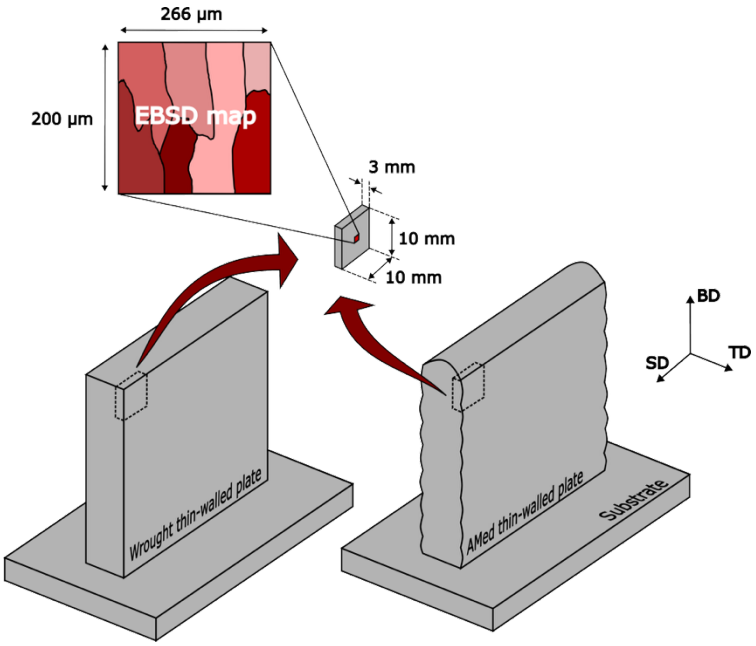


Figure 4.11 Location of the samples for EBSD analyses in the AMed and wrought parts. Location of the EBSD orientation maps in the samples. BD, TD and SD stand for Building, Transverse and Scanning Direction respectively

4.4.3 Machining tests

Both sides of the thin-walled part are dry machined with a 4-fluted milling tool (YG V7 Plus A UGMF70908), whose geometric parameters are given in Table 4.4, on a Mitsui Seiki HU40-T 5-Axis horizontal machining center.

Table 4.4 Geometric parameters of the tool

Tool diameter (mm)	**Helix angle (°)**	**Rake angle (°)**	**Friction angle (°)**	**Flute length (mm)**
6.35	35-37	2-4	55	23

The experimental setup is shown in Figure 4.12. A table dynamometer (Kistler 9255B002) is used to measure the cutting forces in x and y directions. A PCB Piezotronics 1/2" Microphone and three accelerometers (PCB Piezotronics 352C22) are used to capture the machining sound and acceleration data for further vibrations study.

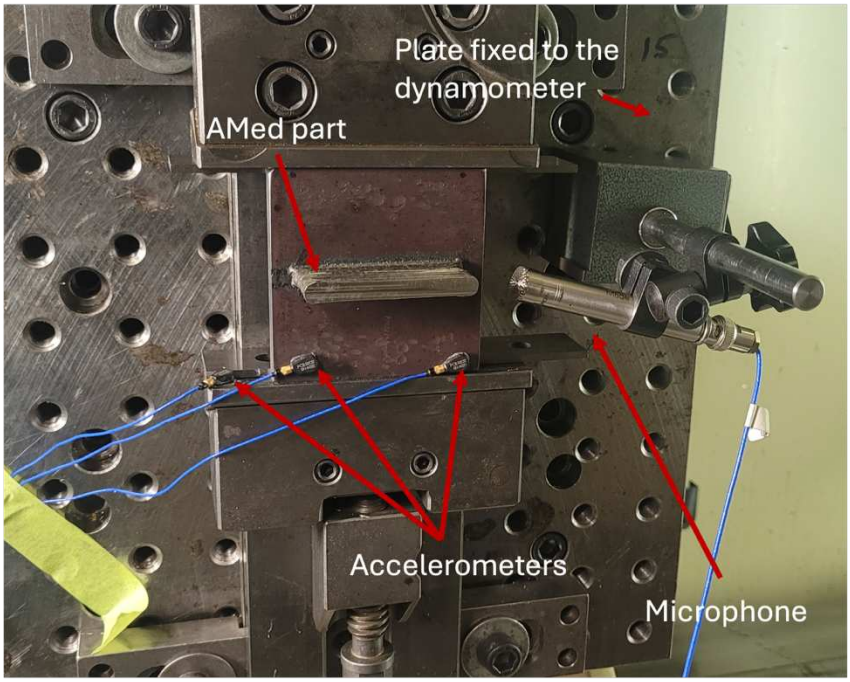


Figure 4.12 Experimental milling setup

Since the initial surface of the plate has a poor quality due to the stack of metal layers with the AM process, a cleaning cut is first performed with 1 mm of radial depth of cut around the workpiece. Then, up- and down-milling operations with various cutting conditions (Table 4.5) are carried out to validate the proposed crystal-based milling mechanics model.

Table 4.5 Cutting conditions used in the milling tests

Test	**Cutting configuration**	V **(m/min)**	n **(rpm)**	f_c **(mm/tooth/rev)**	a_p **(mm)**	a_e **(mm)**	ϕ_{st} **(°)**	ϕ_{ex} **(°)**
T1	Down-milling	15	752	0.06	4.5	1	133	180
T2	Down-milling	30	1504	0.03	4.5	1	133	180

T3	Down-milling	30	1504	0.06	4.5	1	133	180
T4	Up-milling	30	1504	0.015	4.5	1	0	47
T5	Up-milling	50	2506	0.03	4.5	1	0	47

The same cutting operations are performed on the wrought material, without any cleaning because the surfaces are already uniform. The geometry of the thin-walled parts and an illustration of the cutting operations are shown in Figure 4.13. The length of the workpiece is equally divided into three regions and $V_{1,2,3}$, $n_{1,2,3}$ as well as $f_{c1,2,3}$ represent different values of the experimental cutting speed, spindle speed and feed rate used for the tests. One face was used for up-milling operations while the other for down-milling. Only two up-milling cutting tests and three down-milling were analyzed for cutting parameters comparison purpose. Figure 4.13 represents an up-milling operation on a thin-walled part with the orientations of the global coordinate frame (x, y, z) and the frame of the dynamometer (x_d, y_d, z_d).

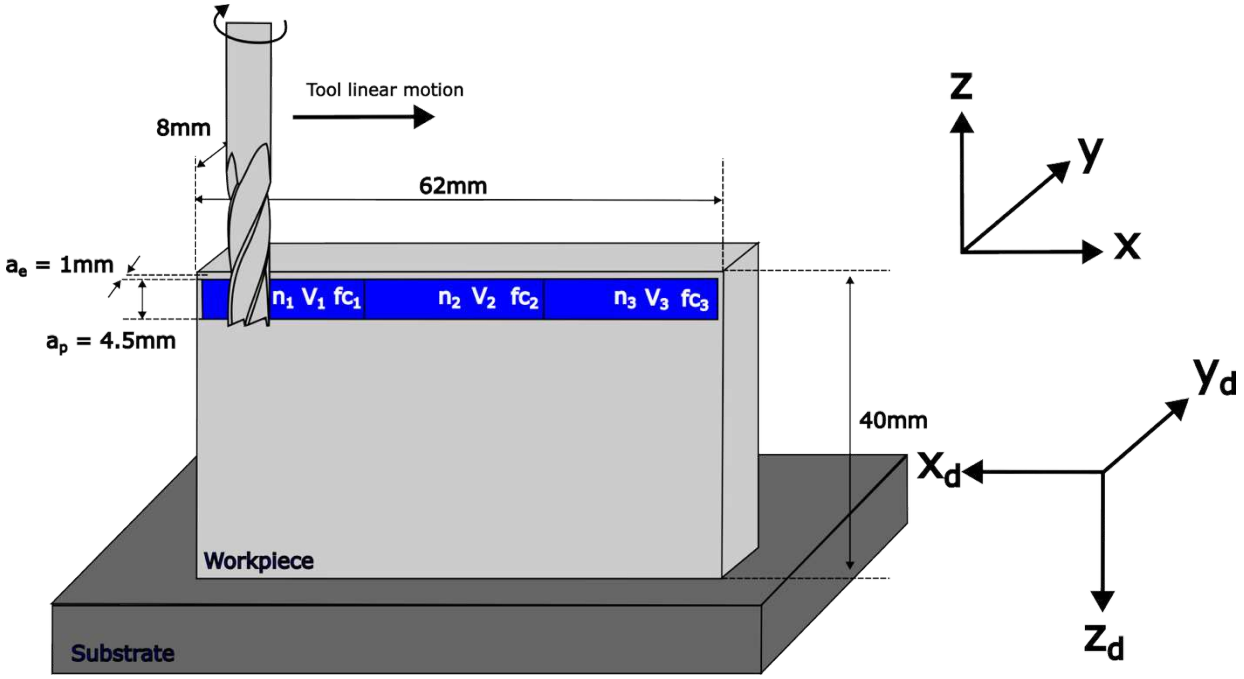


Figure 4.13 Illustration of the up-milling configuration of the milling tests

4.5 Results

In this section, the results of the microstructure analysis and cutting tests are presented.

4.5.1 Microstructure analysis

The cut samples of both AMed and wrought AISI 316L parts are analyzed though EBSD to measure their crystallographic orientations and to correlate the anisotropy with the experimental cutting force measurements and findings. The results of the EBSD analysis on the AMed and wrought samples are respectively shown in Figure 4.14 (a) and (b). Directional columnar grains are observed in the AMed sample as shown in Figure 4.14 (a). These elongated grains grow parallel to the BD with a length of several hundred of micrometers (some of them are larger than 200 μm, the height of the orientation map) and a width of 80 μm. Columnar grains grow vertically, following the steepest temperature gradient located at the bottom of the molten pool, which decreases nonlinearly toward the top surface [168]. The orientation map, colored according to the BD, reveals a predominant alignment of the crystals, with one of their ⟨100⟩ axes oriented parallel to the BD, which is characteristic of AMed metals [109, 112]. On the other hand, the wrought stainless steel (Figure 4.14 (b)) exhibits much smaller grains with an average equivalent circle diameter of 5.5 μm. The orientation map shows random orientation (homogenous) for each grain without specific grain morphology.

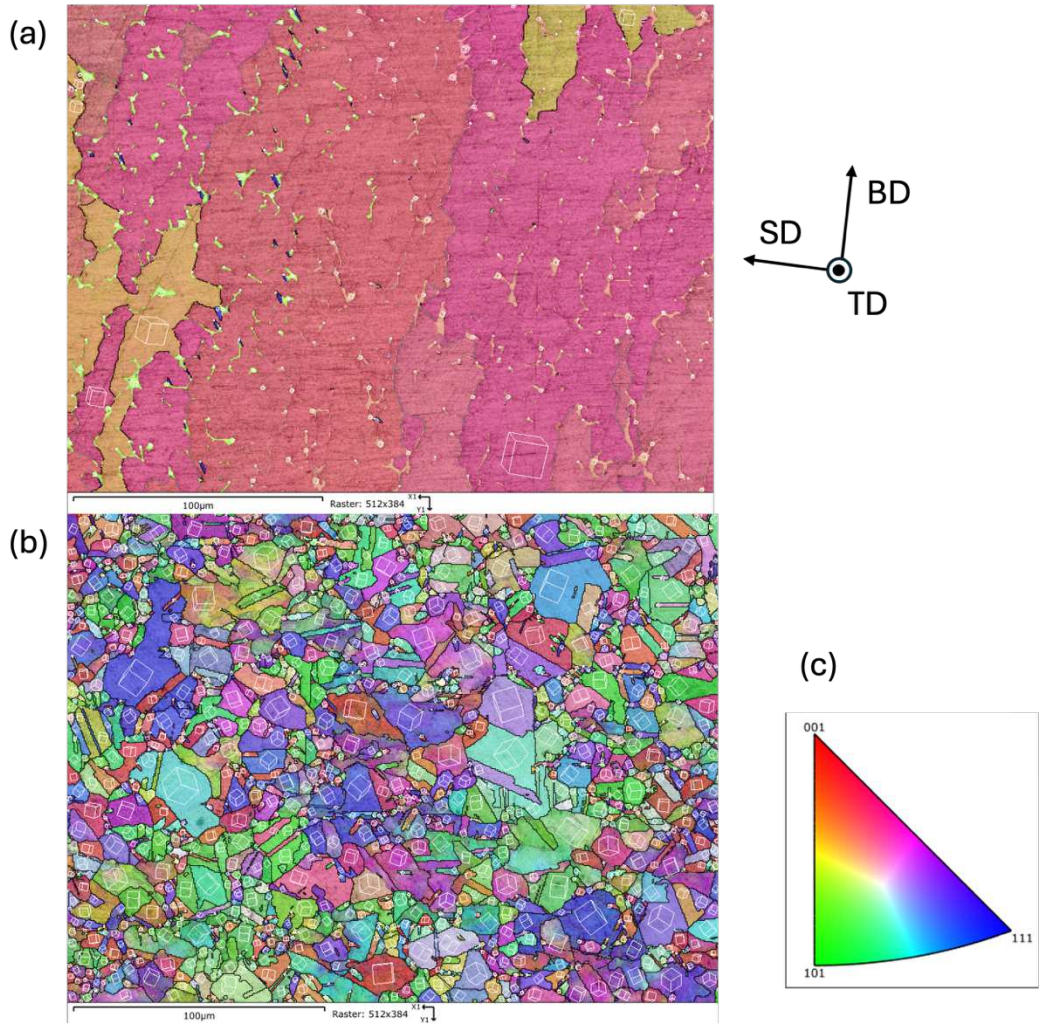


Figure 4.14 EBSD analysis of (a) the AMed thin-walled AISI 316L part, and (b) the wrought thin-walled AISI 316L part. (c) the crystallographic orientation IPF color legend. SD and TD respectively stand for scanning direction and transverse direction

The specimen built by WLAM shows a significant anisotropy in microstructure. A pronounced grain shape anisotropy is immediately apparent from microscopic observations, with the grains' long axes aligned with the BD. However, the mechanical anisotropy in AMed metals is primarily attributed to the material's texture, that is, its crystallographic preferred orientation, rather than to grain shape alone [110]. Therefore, the average crystallographic orientation of each grain, represented by the mean Euler angles between the crystal and sample frames, is used as input in the developed model to account for the microstructure-induced anisotropy in cutting force prediction. However, since a single EBSD analysis has been performed on each cut sample (Section

4.4.2) owing to low axial depth of cut ($a_p = 4.5$ mm) in the tests, a single orientation map has been produced for each material and used as an input for the cutting coefficient predictions. As a result, only one set of cutting force coefficients has been predicted for the whole axial engagement of the tool for each test.

4.5.2 Cutting forces

The experimental cutting forces F_x and F_y are compared with the predicted ones for both the AMed and wrought AISI 316L. The constants used in the proposed machining mechanics model for polycrystal AISI 316L steel are given in Table 4.6. The reference slip rate $\dot{\gamma}_0$ and the strain rate sensitivity exponent n in the flow rule are respectively set to 0.001/s and 15 as suggested in literature [140, 141, 148, 169, 170]. Three parameters of the Voce-type hardening law (h_0, τ_c^{sat} and E) are estimated by curve fitting [171, 172] and respectively set to 260 MPa, 380 MPa, and 5. The latent-to-self-hardening ratio q in the dependency matrix $\boldsymbol{X}_\beta^\alpha$ is assigned a value of 1.0 for coplanar slip systems ($\alpha = \beta$) and 1.4 for non-coplanar slip systems ($\alpha \neq \beta$) [173]. The Johnson-Cook coefficients in the hardening law are obtained from literature [145]. All components of the material's initial stress state $\boldsymbol{\sigma}_0$ are set to 0 MPa.

Table 4.6 Proposed crystal plasticity-based milling mechanics model parameters

	Symbol	**Description**	**Value**
Flow rule	$\dot{\gamma}_0$	Reference slip rate (s^{-1})	0.001
	n	Rate sensitivity	15
Hardening law (Voce-type law part) [172]	h_0	Strain hardening coefficient (MPa)	260
	τ_c^{sat}	Saturation value of CRSS (MPa)	380
	E	Hardening exponent	5
	τ_c^0	Initial critical resolved shear stress (MPa)	140
	C	Strain rate coefficient	0.0274

Hardening law (JC part) [145]	$\dot{\gamma}_0$	Reference shear strain rate (s^{-1})	10^3
	T_r	Reference temperature (K)	293
	T_m	Melting temperature (K)	1793
	m	Thermal softening exponent	1.0
Elasticity [174]	C_{11}	Single crystal elastic constants of austenitic FCC lattice (MPa)	204.6×10^3
	C_{12}		137.7×10^3
	C_{44}		126.6×10^3
Other material properties	ρ	Density (kg/m^3)	8
	c_s	Specific heat (Nm/kg°C)	500
	c_t	Thermal conductivity (W/m°C)	16

Figure 4.15 and Figure 4.16 respectively compare experimental and simulated cutting forces for both AMed and wrought AISI 316L in down-milling (T1, T2, T3) and up-milling (T4, T5) conditions for one full rotation of the tool for simplicity. The small radial engagement compared to the diameter of the tool (15% engagement) combined with a moderate axial depth of cut allows to clearly distinguish the effect of four flutes of the tool in the cutting force pattern. Overall, the predicted cutting forces (solid lines) align well with the experimental data both in terms of amplitude and periodicity. Force peaks and valleys are predicted with an error of 13% for the AMed thin-walled part and 16% for the wrought material, while the average prediction errors are 5% and 6%, respectively. This indicates that the proposed crystal plasticity-based machining mechanics model successfully captures the bulk cutting behavior under all tested cutting conditions. In general, the results show higher cutting force amplitudes (20%) for the AMed part than the wrought one, which are accurately predicted by the developed model. The observed increase in cutting forces when cutting the AMed part may be explained its crystallographic orientation with respect to the cutting edge of the milling tool. During the machining of the AMed thin-walled AISI 316L

in up- and down-milling, the angular deviation between the BD and the cutting edge of the tool is equal to the helix angle. In these conditions, the cutting tool almost cuts around the ⟨100⟩ crystallographic axis aligned with the BD. In Section 3.5.3, orthogonal machining simulations showed that cutting around the ⟨100⟩ crystallographic axes in FCC metals leads to the highest maximum and average specific cutting force coefficients (K_{tc} and K_{fc}), resulting in higher cutting forces and poor machinability. In addition, Bagherzadeh *et al.* [10] recently performed orthogonal cutting tests on AMed Inconel 718 (FCC metal) and showed that cutting along the scanning direction (90° angle from the BD) caused the highest cutting resistance. This is due to the preferred crystallographic orientation aligned with the BD of the AMed part, which results in the highest average cumulative slip ($\sum_\alpha|\gamma^\alpha|$) on the slip systems to accommodate the shear deformation in machining.

Tool runout contributes to the amplitude differences observed between successive force peaks (around 50 N difference is observed in T1 – Fx between the first and second peak). Moreover, the difference in force fluctuations between the AMed and wrought materials under identical cutting conditions are further influenced by the tool wear. Since the cutting tests for the AMed and wrought samples are not conducted sequentially for each set of cutting parameters, variations in tool wear between tests may have affected the measured forces.

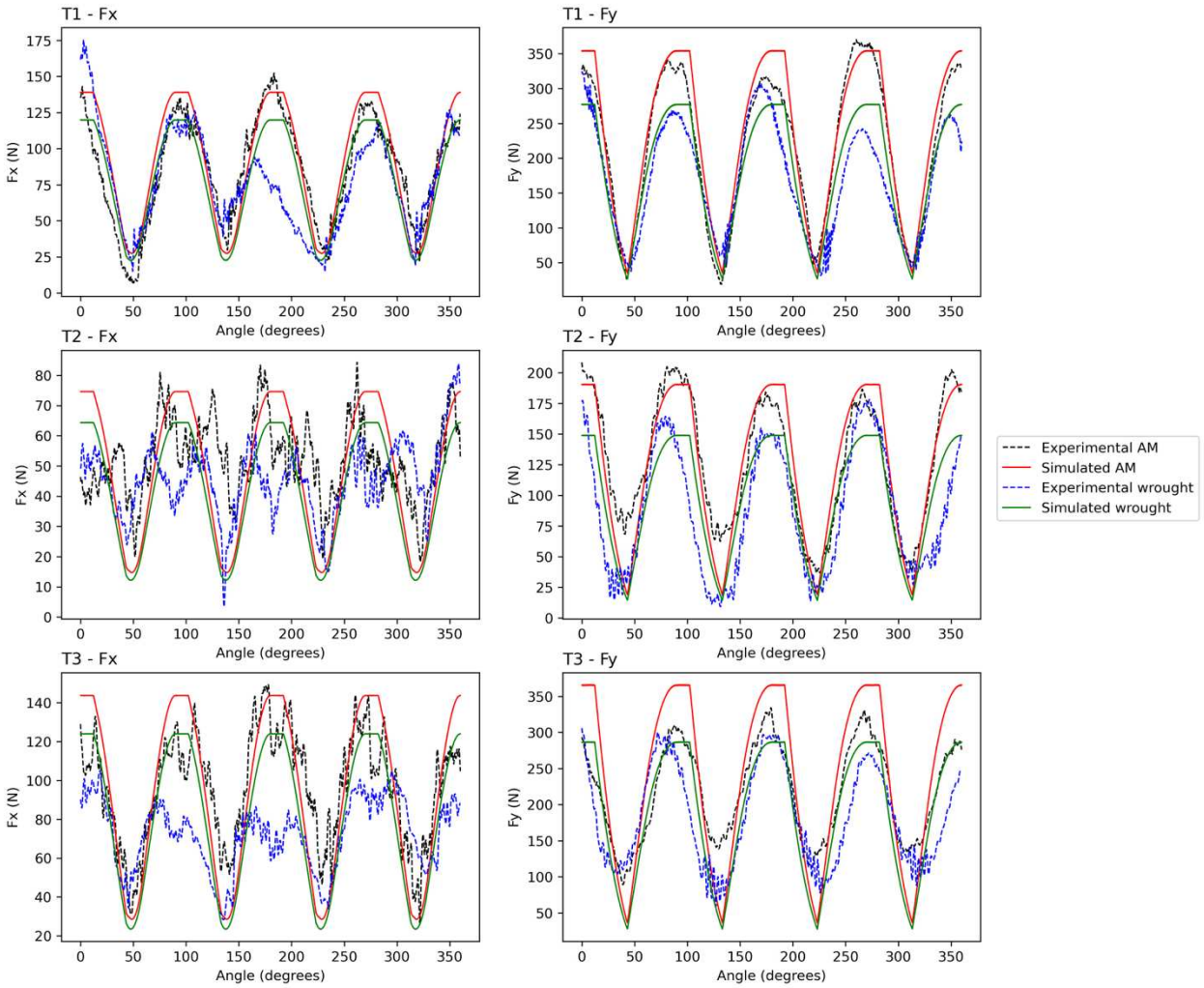


Figure 4.15 Comparison of the experimentally measured and predicted cutting forces for AMed and wrought AISI 316L in down-milling (T1-T3)

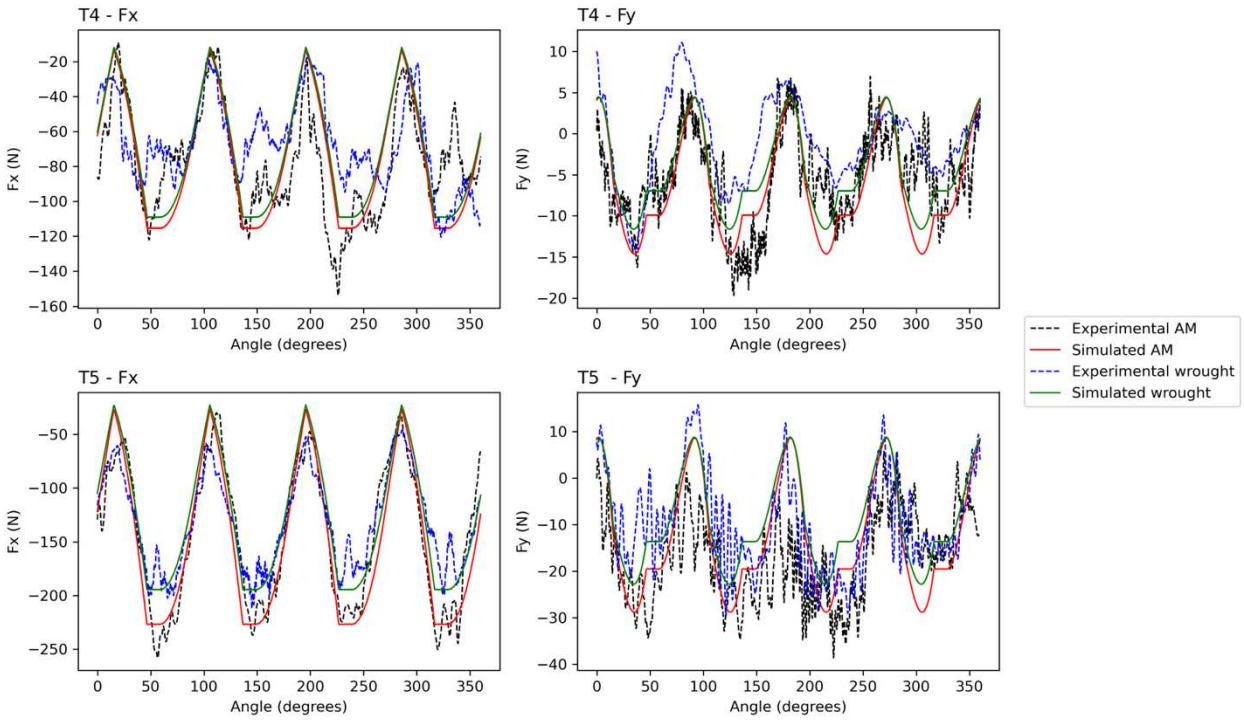


Figure 4.16 Comparison of the experimentally measured and predicted cutting forces for AMed and wrought AISI 316L in up-milling (T4 and T5)

The proposed model also captures the effect of the cutting speed and feed rate on the cutting forces. In accordance with the literature, variations in the cutting speed do not appear to significantly affect both the measured and predicted cutting forces [122, 175]. The average predicted F_y values for the AMed workpiece are 230 N and 237 N for T1 and T3, respectively, while for the wrought workpiece, they are 214 N and 202 N, despite the cutting speed being doubled. An increase of the cutting speed can lead to a decrease of the cutting force due to a higher workpiece temperature that intensifies the thermal softening effect [175]. However, the previous statement is not always observed in anisotropic materials. Careri *et al.* [175] measured slightly higher cutting forces in machining of Inconel 718 produced with DED at 120m/min than 70m/min, which confirms the proposed model's prediction for the AMed AISI 316L in this study. In contrast, the feed rate has a significant effect on the measured and predicted cutting forces. Between T2 and T3, the average F_x and F_y almost doubles with the feed rate. This is expected as the chip cross-section area in T3 is twice as big as in T2. The reason why the prediction in T3 does not show exactly twice the cutting force values in T2 is explained by the size effect, which causes the cutting coefficients in T2 to be

3.4% higher than in T3 because of a smaller uncut chip thickness. Table 4.7 details the values of the average predicted and experimental cutting forces for T2 and T3.

Table 4.7 Effect of the feed rate on the average cutting forces

		T2 ($f_c = 0.03$)		T3 ($f_c = 0.06$)	
		AM	Wrought	AM	Wrought
Prediction	Fx (N)	44.7	37.0	86.1	71.5
	Fy (N)	123	105	237	202
Experimental	Fx (N)	52.3	40.4	101	67.1
	Fy (N)	127	108	217	203

In order to analyze the effect of tool geometry on the predicted forces, machining test T1 is simulated with different helix and rake angles, and the results are presented in Figure 4.17. All other cutting and geometric parameters remain unchanged. Results show that helix (i) and rake (α_n) angles have a significant impact on the cutting force amplitudes, especially on F_y. In Figure 4.17 (a), three different helix angles i (30°, 36° and 40°) are used. The predicted maximum values for F_y increases by 30% when reducing the helix angle from 40° to 30°. When decreasing the helix angle, the axial component of the cutting force F_z becomes less pronounced and the resultant force is more aligned with the x-y plane until $i = 0°$ that represents the orthogonal (2D) cutting. However, the difference in cutting force amplitudes is much smaller for F_x, due to the chip thickness variation in down-milling. The chip is thickest at the entry of the engagement zone, where F_y is the dominant force component, and thinnest at the exit, where F_x becomes more prominent. The rake angle variation has a similar effect to the helix angle on the cutting forces. In Figure 4.17 (b), three values of α_n (2°, 3° and 4°) used in the simulations clearly show a decrease in F_y with higher rake angles. With a smaller rake angle, the chip experiences increased bending prior to evacuation. In contrast, a larger rake angle promotes easier sliding along the rake face, resulting in

more efficient chip evacuation and less forces. Such a model-based analysis is expected to help cutting tool manufacturers to virtually test the performance of different cutting tool geometries in terms of cutting mechanics and to decrease trial-and-error based physical trials.

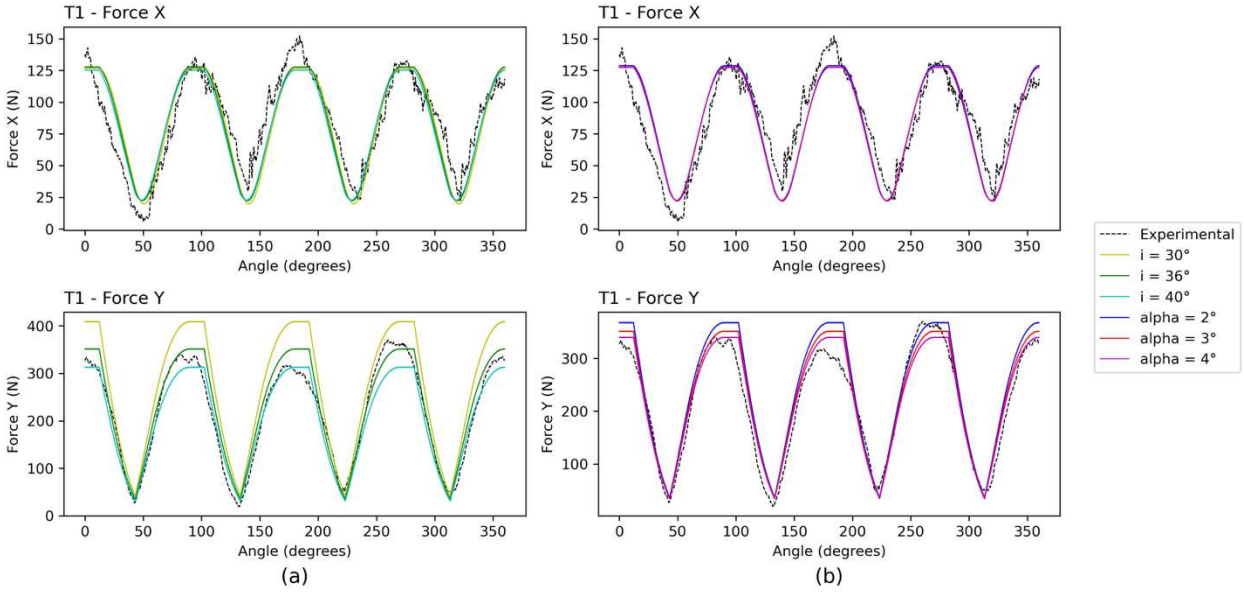


Figure 4.17 Effect of the helix and rake angles on the predicted cutting forces

4.6 Summary

This chapter presented a crystal plasticity-based milling model capable of predicting the effect of microstructure, particularly crystallographic orientation, on the cutting forces in machining of AMed AISI 316L. By incorporating orientation-sensitive constitutive laws and distinguishing between AMed and wrought microstructures, the model can successfully reproduce key differences observed experimentally in both down- and up-milling conditions.

The results show that the AMed material, with its columnar grain structure and texture along the BD, leads to 20% higher cutting force fluctuations as compared to the isotropic wrought material. The simulated cutting forces in x-y plane closely match the experimental results, highlighting the model's ability to account for microstructure-induced anisotropy in machining mechanics.

While the overall agreement between predictions and experiments is strong, the observed discrepancies suggest that further modeling refinements are needed. In particular, modeling of tool

wear, thermal effects of the secondary deformation zone, and grain boundary interactions may help improve prediction accuracy.

CHAPTER 5 CONCLUSION

5.1 Summary and contributions

In this research, a general cutting mechanics model based on crystal-plasticity for machining of AMed parts has been developed. The model considers the crystallographic orientations of the AMed part microstructure, utilizing phenomenological constitutive laws from the crystal plasticity theory to represent how slip systems activate to accommodate the shear strain in the shear deformation zone. The crystal plasticity framework incorporates both elastic and plastic deformation mechanisms to effectively capture the influence of crystallographic orientation, and thus anisotropy, on machining mechanics. The effect of the shear zone temperature and shear strain rate on the material hardening is addressed using a Johnson–Cook constitutive model adapted to crystal plasticity.

A detailed kinematics modeling for flat end-milling is introduced for the first time in crystal-based machining simulation. This includes a uniform shear strain rate geometrically defined using an approximated shear zone thickness [29], a complete description of the oblique cutting kinematics with normal ϕ_n and oblique ϕ_i shear angles derived via total power minimization, and a axially discretized tool approach.

To account for the heterogeneous nature of AMed polycrystalline materials, a homogenization method is implemented over representative regions of the microstructure. The model incorporates three distinct slip system families to represent FCC, BCC, and HCP lattice structures, enabling versatility across a wide range of AMed alloys.

The proposed model is capable of predicting the cutting force coefficients and the related cutting forces as well as shear angles of anisotropic materials such as single crystals and more importantly AMed parts. The developed model has been experimentally verified with 2D orthogonal plunge turning cutting forces [11] of copper and aluminum single crystals and with 3D flat end-milling tests of AMed and wrought AISI 316L for various cutting conditions and tool geometries.

The proposed model is pioneer in analytical milling modeling of AMed materials. Previous studies used finite element (FE) models to study the effect of microstructure induced anisotropy on milling mechanics [176] but most of the previous studies limit themselves to simple tool geometries with a single tooth, or to orthogonal cutting [177] because of the complexity and computational cost of

modeling the cutting process. In contrast, the present model offers a general, computationally efficient, and geometry-independent solution that can handle a wide range of tool geometries, materials, and cutting conditions. It can be directly applied to predict dimensional form errors due to tool or workpiece deflections and serve as a foundation for machining dynamics simulations by providing direction-dependent cutting force coefficients for vibrations and chatter stability analyses. This work lays the groundwork for the digitalization of machining operations in the context of Industry 4.0 by enabling physics-based simulation of AMed part machining at the microstructural level. By integrating this model into virtual machining systems, manufacturers can better predict the cutting forces, optimize tool paths, and ensure dimensional accuracy, thus accelerating the transition toward smart, adaptive, and cost-effective hybrid manufacturing systems.

The scholarly contributions of this thesis can be summarized as:

- Development of a crystal-based cutting mechanics model for anisotropic materials: A new analytical model for 2D and 3D machining mechanics prediction integrating crystal plasticity theory and Johnson–Cook based constitutive model as the hardening law was developed to simulate the machining of AMed parts with microstructure-induced anisotropy.
- The model incorporates full 3D oblique cutting kinematics, including shear zone geometry, tool axial discretization, and the iterative solution of normal and oblique shear angles as opposed to commonly used unjustified assumptions. This is the first time such an approach has been applied analytically in the context of AMed part machining.
- A homogenization method for polycrystalline AMed parts has been implemented to handle the variability of grains orientation. The introduced homogenization method allows to consider common lattice types (FCC, BCC or HCP) used in the aerospace industry and microstructure variations along the axis of the milling tool.

5.2 Model limitations

While this work proposes an accurate model for cutting force prediction in machining of anisotropic materials, there is still room for improvement to reduce the gap between the machining simulation and the physical machining system. First, the proposed model relies on the sharp tool

(cutting edge) assumption, which involves that the entire uncut chip is sheared and that ploughing of the material under the cutting edge on the machined surface is ignored due to a zero edge (hone) radius. Furthermore, the material deformation along the secondary shear zone, where chip slides over the rake face, is not considered. The addition of the secondary deformation zone by developing a crystal-based tool-chip contact model considering the average friction coefficient variation with crystallographic orientation will also improve prediction accuracy. In terms of microstructure, the extended model handles microstructure variations along the axis of the tool but not in the radial direction. Grain boundaries and their effect on the machining response are not considered in the current model but could become significant in micro-machining operations, where the cutting edge is comparable in size to the grain dimensions. However, micromachining was not within the scope of this work.

5.3 Future work

Although BCC and HCP lattice structures have been integrated into the proposed model, there are not model validations with the materials having these lattices. Milling tests on an AMed Ti-6Al-4V ($\alpha + \beta$) workpiece have been performed, but analysis of the microstructure to get the crystallographic orientation inputs for the model have not been carried out due to time constraint. EBSD analyses on titanium samples are much more difficult to perform both in terms of sample preparation and obtaining a good orientation map in the SEM compared to stainless steels. That will be a subject of the next phase in research.

The next step will be to consider the edge radius in the model by modeling the ploughing and compression deformations of the material beneath and ahead of the cutting edge using the crystal plasticity theory. Indeed, its impact is known to have a significant influence on the cutting forces and is one of the causes of size effect at small scale machining. Tool wear and runout could be included in this step.

A temperature prediction model taking into account the edge radius and tool wear has been developed in our research group [156]. It is capable of predicting the temperature not only in the shear zone but also in the tool/chip interface and in the ploughing zone, and it should be integrated into the proposed machining model to accurately model the thermo-mechanical material behavior during machining.

The developed model is currently computationally intense due to the homogenisation step, which considers each grain in the analyzed volume element. Implementing multithreading in the simulation model could drastically improve the computational efficiency as the main iterative computations are all independent.

REFERENCES

[1] B. Yan, Y. Hao, L. Zhu, and C. Liu, "Towards high milling accuracy of turbine blades: A review," *Mechanical Systems and Signal Processing,* Jour vol. 170, p. 108727, 2022, doi: https://doi.org/10.1016/j.ymssp.2021.108727.

[2] N. Tapoglou and J. Clulow, "Investigation of hybrid manufacturing of stainless steel 316L components using direct energy deposition," *Proceedings of the Institution of Mechanical Engineers, Part B: Journal of Engineering Manufacture,* Jour vol. 235, no. 10, pp. 1633-1643, 2021, doi: 10.1177/0954405420949360.

[3] A. Vafadar, F. Guzzomi, A. Rassau, and K. Hayward, "Advances in Metal Additive Manufacturing: A Review of Common Processes, Industrial Applications, and Current Challenges," *Applied Sciences,* Ejour vol. 11, no. 3, 2021, doi: 10.3390/app11031213.

[4] X. Jiang, J. Lu, N. Zhao, Z. Chen, and Z. Zhao, "A Review of Wear in Additive Manufacturing: Wear Mechanism, Materials, and Process," Ejour vol. 12, no. 9, 2024, doi: 10.3390/lubricants12090321.

[5] *Standard Terminology for Additive Manufacturing Technologies*, A. International, 2012.

[6] A. International, *Wohlers Report 2024 3D Printing and Additive Manufacturing State of the Industry*. Wohlers Associates, 2024.

[7] E. Maleki, S. Bagherifard, M. Bandini, and M. Guagliano, "Surface post-treatments for metal additive manufacturing: Progress, challenges, and opportunities," *Additive Manufacturing,* Jour vol. 37, p. 101619, 2021, doi: https://doi.org/10.1016/j.addma.2020.101619.

[8] S. S. Al-Bermani, M. L. Blackmore, W. Zhang, and I. Todd, "The Origin of Microstructural Diversity, Texture, and Mechanical Properties in Electron Beam Melted Ti-6Al-4V," *Metallurgical and Materials Transactions A,* Jour vol. 41, no. 13, pp. 3422-3434, 2010, doi: 10.1007/s11661-010-0397-x.

[9] M. E. Merchant, "Basic Mechanics of the Metal-Cutting Process.," *Journal of Applied Mechanics,* Jour vol. 11, no. 3, pp. A168-A175, 1945, doi: 10.1115/1.4009380.

[10] A. Bagherzadeh, O. Gokcekaya, and E. Budak, "Directional-adaptive approach in machining of additively manufactured Inconel 718," *CIRP Annals,* Jour 2025, doi: https://doi.org/10.1016/j.cirp.2025.04.023.

[11] P. H. Cohen, "The orthogonal in-situ machining of single and polycrystalline aluminum and copper," Ohio State University, 1982.

[12] X. Pu, J. Xu, P. Huang, H. Du, and Z. Zhu, "Fast tool servo-based ultra-precision diamond sculpturing for fabricating micro-structured surfaces," *International Journal of Mechanical Sciences,* Jour vol. 263, p. 108790, 2024, doi: https://doi.org/10.1016/j.ijmecsci.2023.108790.

[13] S. Zhang, Y. Zhou, H. Zhang, Z. Xiong, and S. To, "Advances in ultra-precision machining of micro-structured functional surfaces and their typical applications," *International Journal of Machine Tools and Manufacture,* Jour vol. 142, pp. 16-41, 2019, doi: https://doi.org/10.1016/j.ijmachtools.2019.04.009.

[14] Z. Xu *et al.*, "A review: Insight into smart and sustainable ultra-precision machining augmented by intelligent IoT," *Journal of Manufacturing Systems,* Jour vol. 74, pp. 233-251, 2024, doi: https://doi.org/10.1016/j.jmsy.2024.03.008.

[15] D. Samantaraya, S. Lakade, and A. Keche, "An Alternate Machining Method for Hardened Automotive Gears," *Procedia Manufacturing,* Jour vol. 20, pp. 517-522, 2018, doi: https://doi.org/10.1016/j.promfg.2018.02.077.

[16] S. Pradhan, S. Singh, C. Prakash, G. Królczyk, A. Pramanik, and C. I. Pruncu, "Investigation of machining characteristics of hard-to-machine Ti-6Al-4V-ELI alloy for biomedical applications," *Journal of Materials Research and Technology,* Jour vol. 8, no. 5, pp. 4849-4862, 2019, doi: https://doi.org/10.1016/j.jmrt.2019.08.033.

[17] J. Artozoul *et al.*, *Usinage des pièces mécaniques. Théorie et pratique* (Blanche BTP). 2021, p. 252.

[18] M. E. Merchant, "An interpretive look at 20th century research on modeling of machining.," *Machining Science and Technology,* Jour vol. 2, no. 2, pp. 157-163, 1998, doi: 10.1080/10940349808945666.

[19] H. Soons and S. Yaniv, "Precision in machining: research challenges," (in en), Gen 1995, doi: https://doi.org/10.6028/NIST.IR.5628.

[20] F. W. Taylor, "On the Art of Cutting Metals," *Transactions of the American Society of Mechanical Engineers,* Jour vol. 28, pp. 31-279, 2024, doi: 10.1115/1.4060388.

[21] H. Ernst and M. E. Merchant, *Chip formation, friction and finish*. Cincinnati: Cincinnati Milling Machine Company, 1941.

[22] H. Ernst, *Physics of Metal Cutting*. Cincinnati: Cincinnati Milling Machine Company, 1938.

[23] V. Piispanen, "Lastunmuodostumisen teoriaa," *Teknillinen aikakauslehti,* vol. 27, no. 9, pp. 315-322, 1937.

[24] E. H. Lee and B. W. Shaffer, "The Theory of Plasticity Applied to a Problem of Machining," *Journal of Applied Mechanics,* Jour vol. 18, no. 4, pp. 405-413, 1951, doi: 10.1115/1.4010357.

[25] J. Krystof, *Berichte über betriebswissenschaftliche Arbeiten*. Berlin: VDI Verlag, 1939.

[26] T. Childs, Butterworth-Heinemann, Ed. *Metal Machining: Theory and Applications* (Science Direct e-books). 2000, p. 408.

[27] N. N. Zorev, *Metal Cutting Mechanics*. Oxford: Pergamon Press, 1966, p. 526.

[28] W. B. Palmer and P. L. B. Oxley, "Mechanics of Orthogonal Machining," *Proceedings of the Institution of Mechanical Engineers,* Jour vol. 173, no. 1, pp. 623-654, 1959, doi: 10.1243/pime_proc_1959_173_053_02.

[29] Y. Altintas, "Manufacturing automation : metal cutting mechanics, machine tool vibrations, and CNC design," (in English), Book 2012.

[30] E. Shamoto and Y. Altintas, "Prediction of Shear Angle in Oblique Cutting with Maximum Shear Stress and Minimum Energy Principles," *Journal of Manufacturing Science and Engineering,* Jour vol. 121, no. 3, pp. 399-407, 1999, doi: 10.1115/1.2832695.

[31] G. V. Stabler, "The chip flow and its consequences," presented at the 5th Machine Tool Design and Research Conference, 1964.

[32] E. J. A. Armarego and R. C. Whitfield, "Computer Based Modelling of Popular Machining Operations for Force and Power Prediction," *CIRP Annals,* Jour vol. 34, no. 1, pp. 65-69, 1985, doi: https://doi.org/10.1016/S0007-8506(07)61725-9.

[33] E. Budak, Y. Altintas, and E. J. A. Armarego, "Prediction of Milling Force Coefficients From Orthogonal Cutting Data," *Journal of Manufacturing Science and Engineering-transactions of The Asme - J MANUF SCI ENG,* Jour vol. 118, 1996, doi: 10.1115/1.2831014.

[34] J. S. Strenkowski and J. T. Carrol, "A Finite Element Model of Orthogonal Metal Cutting," *Journal of Engineering for Industry,* Jour vol. 107, no. 4, pp. 349-354, 1985, doi: 10.1115/1.3186008.

[35] J. T. Carroll and J. S. Strenkowski, "Finite element models of orthogonal cutting with application to single point diamond turning," *International Journal of Mechanical Sciences,* Jour vol. 30, no. 12, pp. 899-920, 1988, doi: https://doi.org/10.1016/0020-7403(88)90073-2.

[36] T. H. C. Childs and K. Maekawa, "Computer-aided simulation and experimental studies of chip flow and tool wear in the turning of low alloy steels by cemented carbide tools," *Wear,* Jour vol. 139, no. 2, pp. 235-250, 1990, doi: https://doi.org/10.1016/0043-1648(90)90048-F.

[37] E. Usui, T. Ihara, and T. Shirakashi, "Analytical Prediction of Cutting Edge Chipping in Interrupted Turning Operation (3rd Report)

Distributions of Impact Stress and Fracture Probability within Cutting Edge," *Journal of the Japan Society of Precision Engineering,* Jour vol. 46, no. 8, pp. 983-989, 1980, doi: 10.2493/jjspe1933.46.983.

[38] Y. Altintas, D. Montgomery, and E. Budak, "Dynamic Peripheral Milling of Flexible Structures," *Journal of Engineering for Industry,* Jour vol. 114, no. 2, pp. 137-145, 1992, doi: 10.1115/1.2899766.

[39] G. Bianchi, F. Paolucci, P. Van den Braembussche, H. Van Brussel, and F. Jovane, "Towards Virtual Engineering in MachineTool Design," *CIRP Annals,* Jour vol. 45, no. 1, pp. 381-384, 1996, doi: https://doi.org/10.1016/S0007-8506(07)63085-6.

[40] S. K. Choudhury and J. Mathew, "Investigations of the effect of non-uniform insert pitch on vibration during face milling," *International Journal of Machine Tools and Manufacture,* Jour vol. 35, no. 10, pp. 1435-1444, 1995, doi: https://doi.org/10.1016/0890-6955(94)00131-3.

[41] C. Kiliçaslan, "Modelling and Simulation of Metal Cutting by Finite Element Method," Master of Science, Graduate School of Engineering and Science, Izmir Institute of Technology, Izmir, 2009.

[42] M. Bäker, "The influence of plastic properties on chip formation," *Computational Materials Science,* Jour vol. 28, no. 3, pp. 556-562, 2003, doi: https://doi.org/10.1016/j.commatsci.2003.08.013.

[43] Y. Yen, A. Jain, and T. Altan, "A finite element analysis of orthogonal machining using different tool edge geometries," *Journal of Materials Processing Technology,* Jour vol. 146, no. 1, pp. 72-81, 2004, doi: https://doi.org/10.1016/S0924-0136(03)00846-X.

[44] M. Bäker, "Finite element simulation of high-speed cutting forces," *Journal of Materials Processing Technology,* Jour vol. 176, no. 1, pp. 117-126, 2006, doi: https://doi.org/10.1016/j.jmatprotec.2006.02.019.

[45] C. Shet and X. Deng, "Finite element analysis of the orthogonal metal cutting process," *Journal of Materials Processing Technology,* Jour vol. 105, no. 1, pp. 95-109, 2000, doi: https://doi.org/10.1016/S0924-0136(00)00595-1.

[46] Z. C. Lin and S. P. Lo, "2-D discontinuous chip cutting model by using strain energy density theory and elastic-plastic finite element method," *International Journal of Mechanical Sciences,* Jour vol. 43, no. 2, pp. 381-398, 2001, doi: https://doi.org/10.1016/S0020-7403(00)00015-1.

[47] A. J. Shih and H. T. Y. Yang, "Experimental and finite element predictions of residual stresses due to orthogonal metal cutting," *International Journal for Numerical Methods in Engineering,* Jour vol. 36, no. 9, pp. 1487-1507, 1993, doi: https://doi.org/10.1002/nme.1620360905.

[48] A. Raczy, M. Elmadagli, W. J. Altenhof, and A. T. Alpas, "An eulerian finite-element model for determination of deformation state of a copper subjected to orthogonal cutting," *Metallurgical and Materials Transactions A,* Jour vol. 35, no. 8, pp. 2393-2400, 2004, doi: 10.1007/s11661-006-0219-3.

[49] L. Olovsson, L. Nilsson, and K. Simonsson, "An ALE formulation for the solution of two-dimensional metal cutting problems," *Computers & Structures,* Jour vol. 72, no. 4, pp. 497-507, 1999, doi: https://doi.org/10.1016/S0045-7949(98)00332-0.

[50] M. Movahhedy, M. S. Gadalá, and Y. Altintas, "Simulation of the orthogonal metal cutting process using an arbitrary Lagrangian–Eulerian finite-element method," *Journal of Materials Processing Technology,* Jour vol. 103, no. 2, pp. 267-275, 2000, doi: https://doi.org/10.1016/S0924-0136(00)00480-5.

[51] T. Özel and E. Zeren, "Finite element modeling the influence of edge roundness on the stress and temperature fields induced by high-speed machining," *The International Journal of Advanced Manufacturing Technology,* Jour vol. 35, no. 3, pp. 255-267, 2007, doi: 10.1007/s00170-006-0720-2.

[52] J.-P. Baïlon and J.-M. Dorlot, *Des matériaux*, 3 ed. Montréal: Presses Internationales Polytechnique, 2000.

[53] L. V. Azaroff, *Introduction to solids*. McGraw-Hill Company Inc., 1984, p. 469.

[54] R. Zallen, *The Physics of Amorphous Solids*. Hoboken, NJ: John Wiley & Sons, 2008.

[55] W. D. J. Callister, *Materials Science and Engineering, An Introduction*, 4 ed. New York: John Wiley & Sons, 1997.

[56] J. M. Ziman, "Principles of the Theory of Solids," Book 1972, doi: Doi: 10.1017/cbo9781139644075.

[57] M. C. Flemings, "Solidification processing," *Metallurgical transactions,* Jour vol. 5, no. 10, pp. 2121-2134, 1974, doi: 10.1007/bf02643923.

[58] J. C. Brice and R. A. Laudise, "The Growth of Crystals from Liquids," *Physics Today,* Jour vol. 27, no. 4, pp. 96-97, 1974, doi: 10.1063/1.3128545.

[59] R. A. Brown, "Theory of transport processes in single crystal growth from the melt.," *AIChE Journal,* Jour vol. 34, no. 6, pp. 881-911, 1988, doi: https://doi.org/10.1002/aic.690340602.

[60] B. F. Von Turkovich and J. T. Black, "Micro-Machining of Copper and Aluminum Crystals.," *Journal of Engineering for Industry,* Jour vol. 92, no. 1, pp. 130-134, 1970, doi: 10.1115/1.3427697.

[61] S. Ramalingam and J. Hazra, "Dynamic Shear Stress—Analysis of Single Crystal Machining Studies.," *Journal of Engineering for Industry,* Jour vol. 95, no. 4, pp. 939-944, 1973, doi: 10.1115/1.3438272.

[62] B. F. Von Turkovich, "Shear Stress in letal Cutting," *Transactions of the American Society of Mechanical Engineers,* vol. 92, no. 1, pp. 151-156, 1970.

[63] J. A. Williams and N. Gane, "Some observations on the flow stress of metals during metal cutting," *Wear,* Jour vol. 42, no. 2, pp. 341-353, 1977, doi: https://doi.org/10.1016/0043-1648(77)90062-X.

[64] T. Masuzawa and H. K. Tönshoff, "Three-Dimensional Micromachining by Machine Tools," *CIRP Annals,* Jour vol. 46, no. 2, pp. 621-628, 1997, doi: https://doi.org/10.1016/S0007-8506(07)60882-8.

[65] N. Ikawa, S. Shimada, and H. Tanaka, "Minimum thickness of cut in micromachining," *Nanotechnology,* Jour vol. 3, no. 1, p. 6, 1992, doi: 10.1088/0957-4484/3/1/002.

[66] I. F. Stowers *et al.*, "Molecular Dynamics Simulation of the Chip Formation Process in Single Crystal Copper and Comparison With Experimental Data," *Proceedings of the ASPE Annual Meeting,* pp. 100-104, 1991.

[67] D. Dornfeld, S. Min, and Y. Takeuchi, "Recent Advances in Mechanical Micromachining," *CIRP Annals,* Jour vol. 55, no. 2, pp. 745-768, 2006, doi: https://doi.org/10.1016/j.cirp.2006.10.006.

[68] M. P. Vogler, R. E. DeVor, and S. G. Kapoor, "On the Modeling and Analysis of Machining Performance in Micro-Endmilling, Part I: Surface Generation," *Journal of Manufacturing Science and Engineering,* Jour vol. 126, no. 4, pp. 685-694, 2005, doi: 10.1115/1.1813470.

[69] M. P. Vogler, S. G. Kapoor, and R. E. DeVor, "On the Modeling and Analysis of Machining Performance in Micro-Endmilling, Part II: Cutting Force Prediction," *Journal of Manufacturing Science and Engineering,* Jour vol. 126, no. 4, pp. 695-705, 2005, doi: 10.1115/1.1813471.

[70] D. A. Lucca, R. L. Rhorer, and R. Komanduri, "Energy Dissipation in the Ultraprecision Machining of Copper," *CIRP Annals,* Jour vol. 40, no. 1, pp. 69-72, 1991, doi: https://doi.org/10.1016/S0007-8506(07)61936-2.

[71] D. A. Lucca, Y. W. Seo, and R. Komanduri, "Effect of Tool Edge Geometry on Energy Dissipation in Ultraprecision Machining," *CIRP Annals,* Jour vol. 42, no. 1, pp. 83-86, 1993, doi: https://doi.org/10.1016/S0007-8506(07)62397-X.

[72] Y. Furukawa and N. Moronuki, "Effect of Material Properties on Ultra Precise Cutting Processes," *CIRP Annals,* Jour vol. 37, no. 1, pp. 113-116, 1988, doi: https://doi.org/10.1016/S0007-8506(07)61598-4.

[73] E. Demir and C. Mercan, "A physics-based single crystal plasticity model for crystal orientation and length scale dependence of machining response," *Modelling and Simulation in Materials Science and Engineering,* Jour vol. 25, no. 1, 2017, doi: 10.1088/1361-651x/25/1/015009.

[74] K. Ueda, K. Iwata, and K. Nakayama, "Chip Formation Mechanism in Single Crystal Cutting of β-Brass," *CIRP Annals,* Jour vol. 29, no. 1, pp. 41-46, 1980, doi: https://doi.org/10.1016/S0007-8506(07)61292-X.

[75] J. T. Black, "On the Fundamental Mechanism of Large Strain Plastic Deformation: Electron Microscopy of Metal Cutting Chips," *Journal of Engineering for Industry,* Jour vol. 93, no. 2, pp. 507-526, 1971, doi: 10.1115/1.3427958.

[76] M. Sato, Y. Kato, and K. Tsutiya, "Effects of crystal orientation on the flow mechanism in cutting aluminum single crystal," *Transactions of the Japan Institute of Metals,* Jour vol. 20, no. 8, pp. 414-22, 1979.

[77] M. Sato, T. Yamazaki, Y. Shimizu, and T. Takabayashi, "A Study on the Microcutting of Aluminum Single Crystals," *JSME international journal. Ser. 3, Vibration, control engineering, engineering for industry,* Jour vol. 34, no. 4, pp. 540-545, 1991, doi: 10.1299/jsmec1988.34.540.

[78] S. To, W. B. Lee, and C. Y. Chan, "Ultraprecision Diamond Turning of Aluminium Single Crystals," *Journal of Materials Processing Technology,* Jour vol. 63, no. 1, pp. 157-162, 1997, doi: https://doi.org/10.1016/S0924-0136(96)02617-9.

[79] B. L. Lawson, N. Kota, and O. B. Ozdoganlar, "Effects of Crystallographic Anistropy on Orthogonal Micromachining of Single-Crystal Aluminum," *Journal of Manufacturing Science and Engineering,* Jour vol. 130, no. 3, 2008, doi: 10.1115/1.2917268.

[80] Z. J. Yuan, W. B. Lee, Y. X. Yao, and M. Zhou, "Effect of crystallographic orientation on cutting forces and surface quality in diamond cutting of single crystal.," *CIRP Annals,* Jour vol. 43, no. 1, pp. 39-42, 1994, doi: https://doi.org/10.1016/S0007-8506(07)62159-3.

[81] G. I. Taylor, "Plastic strain in metals," *Journal of the Institute of Metals,* vol. 62, pp. 307-324, 1938.

[82] A. Needleman, R. J. Asaro, J. Lemonds, and D. Peirce, "Finite element analysis of crystalline solids," *Computer Methods in Applied Mechanics and Engineering,* Jour vol. 52, no. 1, pp. 689-708, 1985, doi: https://doi.org/10.1016/0045-7825(85)90014-3.

[83] S. R. Kalidindi, C. A. Bronkhorst, and L. Anand, "Crystallographic texture evolution in bulk deformation processing of FCC metals," *Journal of the Mechanics and Physics of Solids,* Jour vol. 40, no. 3, 1992, doi: info:doi/10.1016/0022-5096(92)80003-9.

[84] A. M. Maniatty, P. R. Dawson, and Y.-.-S. Lee, "A time integration algorithm for elasto-viscoplastic cubic crystals applied to modelling polycrystalline deformation," *International Journal for Numerical Methods in Engineering,* Jour vol. 35, no. 8, pp. 1565-1588, 1992, doi: https://doi.org/10.1002/nme.1620350803.

[85] P. R. Dawson, "Computational crystal plasticity," *International Journal of Solids and Structures,* Jour vol. 37, no. 1, pp. 115-130, 2000, doi: https://doi.org/10.1016/S0020-7683(99)00083-9.

[86] L. Chuzhoy, R. E. DeVor, S. G. Kapoor, A. J. Beaudoin, and D. J. Bammann, "Machining Simulation of Ductile Iron and Its Constituents, Part 1: Estimation of Material Model Parameters and Their Validation," *Journal of Manufacturing Science and Engineering,* Jour vol. 125, no. 2, pp. 181-191, 2003, doi: 10.1115/1.1557294.

[87] L. Chuzhoy, R. E. DeVor, and S. G. Kapoor, "Machining Simulation of Ductile Iron and Its Constituents, Part 2: Numerical Simulation and Experimental Validation of Machining," *Journal of Manufacturing Science and Engineering,* Jour vol. 125, no. 2, pp. 192-201, 2003, doi: 10.1115/1.1557295.

[88] T. Obikawa, Y. Takemura, Y. Akiyama, J. Shinozuka, and H. Sasahara, "Microscopic phase-dependent residual stresses in the machined surface layer of two-phase alloy," *Journal of Materials Processing Technology,* Jour vol. 209, no. 9, pp. 4496-4501, 2009, doi: https://doi.org/10.1016/j.jmatprotec.2008.10.039.

[89] A. Simoneau, E. Ng, and M. A. Elbestawi, "Chip formation during microscale cutting of a medium carbon steel," *International Journal of Machine Tools and Manufacture,* Jour vol. 46, no. 5, pp. 467-481, 2006, doi: https://doi.org/10.1016/j.ijmachtools.2005.07.019.

[90] A. Simoneau, E. Ng, and M. A. Elbestawi, "Surface defects during microcutting," *International Journal of Machine Tools and Manufacture,* Jour vol. 46, no. 12, pp. 1378-1387, 2006, doi: https://doi.org/10.1016/j.ijmachtools.2005.10.001.

[91] M. Sato, Y. Kato, K. Tsutiya, and S. Aoki, "Effects of Crystal Orientation on the Cutting Mechanism of Aluninum Single Crystal," *Bulletin of JSME,* Jour vol. 24, no. 196, pp. 1864-1870, 1981, doi: 10.1299/jsme1958.24.1864.

[92] M. Sato, Y. Kato, S. Aoki, and A. Ikoma, "Effects of Crystal Orientation on the Cutting Mechanism of the Aluminum Single Crystal : 2nd Report : On the (111) plane and the (112) end Cutting," *Bulletin of JSME,* Jour vol. 26, no. 215, pp. 890-896, 1983, doi: 10.1299/jsme1958.26.890.

[93] W. B. Lee and M. Zhou, "A theoretical analysis of the effect of crystallographic orientation on chip formation in micromachining," *International Journal of Machine Tools and Manufacture,* Jour vol. 33, no. 3, pp. 439-447, 1993, doi: https://doi.org/10.1016/0890-6955(93)90050-5.

[94] W. B. Lee and W. Yang, "Methodology and applications of mesoplasticity in manufacturing sciences," *International Journal of Mechanical Sciences,* Jour vol. 35, no. 12, pp. 1079-1095, 1993, doi: https://doi.org/10.1016/0020-7403(93)90057-2.

[95] M. Zhou and B. K. A. Ngoi, "Effect of tool and workpiece anisotropy on microcutting processes," *Proceedings of the Institution of Mechanical Engineers, Part B: Journal of*

Engineering Manufacture, Jour vol. 215, no. 1, pp. 13-19, 2001, doi: 10.1243/0954405011515091.

[96] W. B. Lee, S. To, K. Y. Sze, and C. F. Cheung, "Effect of material anisotropy on shear angle prediction in metal cutting—a mesoplasticity approach," *International Journal of Mechanical Sciences,* Jour vol. 45, no. 10, pp. 1739-1749, 2003, doi: https://doi.org/10.1016/j.ijmecsci.2003.09.024.

[97] E. Demir, "A Taylor-based plasticity model for orthogonal machining of single-crystal FCC materials including frictional effects," *The International Journal of Advanced Manufacturing Technology,* Jour vol. 40, no. 9, pp. 847-856, 2009, doi: 10.1007/s00170-008-1409-5.

[98] E. Demir, "A method to include plastic anisotropy to orthogonal micromachining of fcc single crystals," *The International Journal of Advanced Manufacturing Technology,* Jour vol. 43, no. 5, pp. 474-481, 2009, doi: 10.1007/s00170-008-1738-4.

[99] J. F. W. Bishop and R. Hill, "XLVI. A theory of the plastic distortion of a polycrystalline aggregate under combined stresses," *The London, Edinburgh, and Dublin Philosophical Magazine and Journal of Science,* Jour vol. 42, no. 327, pp. 414-427, 1951, doi: 10.1080/14786445108561065.

[100] A. Arsenlis and D. M. Parks, "Modeling the evolution of crystallographic dislocation density in crystal plasticity," *Journal of the Mechanics and Physics of Solids,* Jour vol. 50, no. 9, pp. 1979-2009, 2002, doi: https://doi.org/10.1016/S0022-5096(01)00134-X.

[101] A. Ma and F. Roters, "A constitutive model for fcc single crystals based on dislocation densities and its application to uniaxial compression of aluminium single crystals," *Acta Materialia,* Jour vol. 52, no. 12, pp. 3603-3612, 2004, doi: https://doi.org/10.1016/j.actamat.2004.04.012.

[102] J. W. Hutchinson, "Bounds and self-consistent estimates for creep of polycrystalline materials.," *Proc. R. Soc. Lond. A,* vol. 348, pp. 101-127, 1976.

[103] H. Ben Boubaker, K. S. Djaka, A. Moufki, M. Nouari, P. Laheurte, and A. Tidu, "Thermomechanical modeling of crystallographic anisotropy effect on machining forces based on crystal plasticity framework," *Machining Science and Technology,* Jour vol. 25, no. 6, pp. 930-956, 2021, doi: 10.1080/10910344.2021.1971708.

[104] Y. Ayed, C. Robert, G. Germain, and A. Ammar, "Orthogonal micro-cutting modeling of the Ti17 titanium alloy using the crystal plasticity theory," *Finite Elements in Analysis and Design,* Jour vol. 137, pp. 43-55, 2017, doi: https://doi.org/10.1016/j.finel.2017.08.002.

[105] D. Deka, D. S. Joseph, S. Ghosh, and M. J. Mills, "Crystal plasticity modeling of deformation and creep in polycrystalline Ti-6242," *Metallurgical and Materials Transactions A,* Jour vol. 37, no. 5, pp. 1371-1388, 2006, doi: 10.1007/s11661-006-0082-2.

[106] A. Venkatraman, D. L. McDowell, and S. R. Kalidindi, "Bayesian analysis of parametric uncertainties and model form probabilities for two different crystal plasticity models of lamellar grains in α+β Titanium alloys," *International Journal of Plasticity,* Jour vol. 154, p. 103289, 2022, doi: https://doi.org/10.1016/j.ijplas.2022.103289.

[107] *Terminology for Additive Manufacturing Technologies*, A. International, 2012.

[108] K. N. Amato *et al.*, "Microstructures and mechanical behavior of Inconel 718 fabricated by selective laser melting," *Acta Materialia,* Jour vol. 60, no. 5, pp. 2229-2239, 2012, doi: https://doi.org/10.1016/j.actamat.2011.12.032.

[109] X. Zhou *et al.*, "Textures formed in a CoCrMo alloy by selective laser melting," *Journal of Alloys and Compounds,* Jour vol. 631, pp. 153-164, 2015, doi: https://doi.org/10.1016/j.jallcom.2015.01.096.

[110] K. Kunze, T. Etter, J. Grässlin, and V. Shklover, "Texture, anisotropy in microstructure and mechanical properties of IN738LC alloy processed by selective laser melting (SLM)," *Materials Science and Engineering: A,* Jour vol. 620, pp. 213-222, 2015, doi: https://doi.org/10.1016/j.msea.2014.10.003.

[111] F. Geiger, K. Kunze, and T. Etter, "Tailoring the texture of IN738LC processed by selective laser melting (SLM) by specific scanning strategies," *Materials Science and Engineering: A,* Jour vol. 661, pp. 240-246, 2016, doi: 10.1016/j.msea.2016.03.036.

[112] L. Thijs, K. Kempen, J. P. Kruth, and J. V. Humbeeck, "Fine-structured aluminium products with controllable texture by selective laser melting of pre-alloyed AlSi10Mg powder," *Acta Materialia,* Jour vol. 61, no. 5, pp. 1809-1819, 2013, doi: https://doi.org/10.1016/j.actamat.2012.11.052.

[113] G. P. Dinda, A. K. Dasgupta, and J. Mazumber, "Evolution of microstructure in laser deposited Al–11.28%Si alloy," *Surface and Coatings Technology,* Jour vol. 206, no. 8, pp. 2152-2160, 2012, doi: https://doi.org/10.1016/j.surfcoat.2011.09.051.

[114] X. Xu, G. Mi, Y. Luo, P. Jiang, X. Shao, and C. Wang, "Morphologies, microstructures, and mechanical properties of samples produced using laser metal deposition with 316 L stainless steel wire," *Optics and Lasers in Engineering,* Jour vol. 94, pp. 1-11, 2017, doi: https://doi.org/10.1016/j.optlaseng.2017.02.008.

[115] C. Wang, P. Zhu, F. Wang, Y. H. Lu, and T. Shoji, "Anisotropy of microstructure and corrosion resistance of 316L stainless steel fabricated by wire and arc additive manufacturing," *Corrosion Science,* Jour vol. 206, p. 110549, 2022, doi: https://doi.org/10.1016/j.corsci.2022.110549.

[116] X. Chen, J. Li, X. Cheng, H. Wang, and Z. Huang, "Effect of heat treatment on microstructure, mechanical and corrosion properties of austenitic stainless steel 316L using arc additive manufacturing," *Materials Science and Engineering: A,* Jour vol. 715, pp. 307-314, 2018, doi: https://doi.org/10.1016/j.msea.2017.10.002.

[117] L. Wang, J. Xue, and Q. Wang, "Correlation between arc mode, microstructure, and mechanical properties during wire arc additive manufacturing of 316L stainless steel," *Materials Science and Engineering: A,* Jour vol. 751, pp. 183-190, 2019, doi: https://doi.org/10.1016/j.msea.2019.02.078.

[118] M. Goland, "Comportement en corrosion et en corrosion sous contrainte en milieu primaire REP d'un acier inoxydable 316L par fabrication additive WAAM et WLAM," Sorbonne Université, 2024.

[119] A. Calleja, G. Urbikain, and H. Gonzalez, "Inconel®718 superalloy machinability evaluation after laser cladding additive manufacturing process," *The International Journal of Advanced Manufacturing Technology,* Jour vol. 97, no. 5, pp. 2873-2885, 2018, doi: 10.1007/s00170-018-2169-5.

[120] L. Chen, Q. Xu, Y. Liu, G. Cai, and J. Liu, "Machinability of the laser additively manufactured Inconel 718 superalloy in turning," *International Journal of Advanced Manufacturing Technology,* Jour vol. 114, no. 3-4, pp. 871-882, 2021, doi: 10.1007/s00170-021-06940-8.

[121] N. Chernovol, A. Sharma, T. Tjahjowidodo, B. Lauwers, and P. Van Rymenant, "Machinability of wire and arc additive manufactured components," *CIRP Journal of Manufacturing Science and Technology,* Jour vol. 35, pp. 379-389, 2021, doi: 10.1016/j.cirpj.2021.06.022.

[122] P. P. Fonseca *et al.*, "Orthogonal cutting of Wire and Arc Additive Manufactured parts," *International Journal of Advanced Manufacturing Technology,* Jour vol. 119, no. 7-8, pp. 4439-4459, 2022, doi: 10.1007/s00170-022-08678-3.

[123] A. Polishetty, J. Nomani, and G. Littlefair, "Evaluating and comparing secondary machining characteristics of wrought and additive manufactured 316L stainless steel," *Materials Today: Proceedings,* Jour 2023, doi: https://doi.org/10.1016/j.matpr.2023.05.404.

[124] G. Le Coz, M. Fischer, R. Piquard, A. D'Acunto, P. Laheurte, and D. Dudzinski, "Micro cutting of Ti-6Al-4V parts produced by SLM Process," *Procedia CIRP,* Jour vol. 58, pp. 228-232, 2017, doi: https://doi.org/10.1016/j.procir.2017.03.326.

[125] K. S. Al-Rubaie, S. Melotti, A. Rabelo, J. M. Paiva, M. A. Elbestawi, and S. C. Veldhuis, "Machinability of SLM-produced Ti6Al4V titanium alloy parts," *Journal of Manufacturing Processes,* Jour vol. 57, pp. 768-786, 2020, doi: https://doi.org/10.1016/j.jmapro.2020.07.035.

[126] A. Kallel, A. Duchosal, H. Hamdi, G. Altmeyer, A. Morandeau, and S. Méo, "Analysis of the surface integrity induced by face milling of Laser Metal Deposited Ti-6Al-4V," *Procedia CIRP,* Jour vol. 87, pp. 345-350, 2020, doi: https://doi.org/10.1016/j.procir.2020.02.030.

[127] F. Montevecchi, N. Grossi, H. Takagi, A. Scippa, H. Sasahara, and G. Campatelli, "Cutting Forces Analysis in Additive Manufactured AISI H13 Alloy," *Procedia CIRP,* Jour vol. 46, pp. 476-479, 2016, doi: https://doi.org/10.1016/j.procir.2016.04.034.

[128] H. A. Kishawy, N. Nguyen, A. Hosseini, and M. Elbastawi, "Machining characteristics of additively manufactured titanium, cutting mechanics and chip morphology," *CIRP Annals,* Jour vol. 72, no. 1, pp. 49-52, 2023, doi: https://doi.org/10.1016/j.cirp.2023.04.056.

[129] L. Lizzul, M. Sorgato, R. Bertolini, A. Ghiotti, and S. Bruschi, "Influence of additive manufacturing-induced anisotropy on tool wear in end milling of Ti6Al4V," *Tribology International,* Jour vol. 146, p. 106200, 2020, doi: https://doi.org/10.1016/j.triboint.2020.106200.

[130] E. Kim, H. Park, C. Lee, J. Park, S. Yang, and Y. Jung, "Single crystal casting of gas turbine blades using superior ceramic core," *Journal of Materials Research and Technology,* Jour vol. 9, no. 3, pp. 3348-3356, 2020, doi: https://doi.org/10.1016/j.jmrt.2020.01.029.

[131] S. Rong, B. Faheem, and Y. Li, "Perovskite single crystals: Synthesis, properties, and applications," *Journal of Electronic Science and Technology,* Jour vol. 19, no. 2, p. 100081, 2021, doi: https://doi.org/10.1016/j.jnlest.2021.100081.

[132] E. Hosseini and V. A. Popovich, "A review of mechanical properties of additively manufactured Inconel 718," *Additive Manufacturing,* Jour vol. 30, 2019, doi: 10.1016/j.addma.2019.100877.

[133] S. Kieren-Ehses *et al.*, "The influence of the crystallographic orientation when micro machining commercially pure titanium: A size effect," *Precision Engineering,* Jour vol. 72, pp. 158-171, 2021, doi: 10.1016/j.precisioneng.2021.04.007.

[134] N. Kota and O. Burak Ozdoganlar, "A model-based analysis of orthogonal cutting for singlecrystal fcc metals including crystallographic anisotropy," *Machining Science and Technology,* Jour vol. 14, no. 1, pp. 102-127, 2010, doi: 10.1080/10910340903586517.

[135] Y. Zhang, T. Mabrouki, D. Nelias, J. Rech, and Y. Gong, "Cutting simulation capabilities based on crystal plasticity theory and discrete cohesive elements," *Journal of Materials Processing Technology,* Jour vol. 212, no. 4, pp. 936-953, 2012, doi: https://doi.org/10.1016/j.jmatprotec.2011.12.001.

[136] Z. Wang *et al.*, "Crystal plasticity finite element modeling and simulation of diamond cutting of polycrystalline copper," *Journal of Manufacturing Processes,* Jour vol. 38, pp. 187-195, 2019, doi: 10.1016/j.jmapro.2019.01.007.

[137] P. L. B. Oxley and M. C. Shaw, "Mechanics of Machining: An Analytical Approach to Assessing Machinability," *Journal of Applied Mechanics,* Jour vol. 57, no. 1, pp. 253-253, 1990, doi: 10.1115/1.2888318.

[138] P. S. Follansbee and U. F. Kocks, "Constitutive Description of the Deformation of Copper Based on the Use of the Mechanical Threshold Stress as an Internal State Variable," *Acta Metallurgica,* Jour vol. 36, no. 1, pp. 81-93, 1988, doi: 10.1016/0001-6160(88)90030-2.

[139] G. R. Johnson and W. H. Cook, "A constitutive model and data for metals subjected to large strains, high strain rates and high temperatures," pp. 541–547, 1983.

[140] W. Wang and J. Liu, "Crystal plasticity modeling of strain rate and temperature sensitivities in magnesium," *Acta Mechanica,* Jour vol. 230, no. 6, pp. 2071-2086, 2019, doi: 10.1007/s00707-019-2374-9.

[141] R. Chakrabarty and J. Song, "Crystal plasticity finite element investigation of deformation of single crystal copper during cold spray," *Additive Manufacturing,* Jour vol. 49, p. 102484, 2022, doi: https://doi.org/10.1016/j.addma.2021.102484.

[142] M. E. Merchant, "Mechanics of the metal cutting process, and type 2 chip," *Journal of Applied Physics,* Jour vol. 16, no. 6, pp. 267-275, 1945, doi: 10.1063/1.1707596.

[143] D. Peirce, R. J. Asaro, and A. Needleman, "An analysis of nonuniform and localized deformation in ductile single crystals," *Acta Metallurgica,* Jour vol. 30, no. 6, pp. 1087-1119, 1982, doi: https://doi.org/10.1016/0001-6160(82)90005-0.

[144] J. L. Bassini and T.-Y. Wu, "Latent hardening in single crystals. II. Analytical characterization and predictions," *Proc. R. Soc. Lond. A,* vol. 435, pp. 21-41, 1991.

[145] G. Bae, Y. Xiong, S. Kumar, K. Kang, and C. Lee, "General aspects of interface bonding in kinetic sprayed coatings," *Acta Materialia,* Jour vol. 56, no. 17, pp. 4858-4868, 2008, doi: https://doi.org/10.1016/j.actamat.2008.06.003.

[146] Y. Wang, D. Raabe, C. Klüber, and F. Roters, "Orientation dependence of nanoindentation pile-up patterns and of nanoindentation microtextures in copper single crystals," *Acta Materialia,* Jour vol. 52, no. 8, pp. 2229-2238, 2004, doi: https://doi.org/10.1016/j.actamat.2004.01.016.

[147] C. Wang, X. Wang, C. Wang, G. Wu, and Y. Lai, "A comparative study of plastic deformation behaviors of OFHC copper based on crystal plasticity models in conjunction with phenomenological and dislocation density-based hardening laws," *Journal of Materials Science,* Jour vol. 56, no. 14, pp. 8789-8814, 2021, doi: 10.1007/s10853-021-05816-2.

[148] E. Demir, F. Roters, and D. Raabe, "Bending of single crystal microcantilever beams of cube orientation: Finite element model and experiments," *Journal of the Mechanics and Physics of Solids,* Jour vol. 58, no. 10, pp. 1599-1612, 2010, doi: 10.1016/j.jmps.2010.07.007.

[149] F. Roters *et al.*, "DAMASK – The Düsseldorf Advanced Material Simulation Kit for modeling multi-physics crystal plasticity, thermal, and damage phenomena from the single crystal up to the component scale," *Computational Materials Science,* Jour vol. 158, pp. 420-478, 2019, doi: https://doi.org/10.1016/j.commatsci.2018.04.030.

[150] R. Dadhich and A. Alankar, "A modular spectral solver for crystal plasticity," *International Journal of Plasticity,* Jour vol. 156, p. 103328, 2022, doi: 10.1016/j.ijplas.2022.103328.

[151] K. Nakayama and K. Tamura, "Size Effect in Metal-Cutting Force.," *Journal of Engineering for Industry,* Jour vol. 90, no. 1, pp. 119-126, 1968, doi: 10.1115/1.3604585.

[152] M. Masuko, "Fundamental Research on the Metal Cutting, Second Report," *Bulletin of Japan Society of Mechanical Engineers,* vol. 22, no. 118, pp. 371-377, 1956.

[153] S. N. Melkote and S. Subbiah, "Size Effects in Machining Tribology," in *Encyclopedia of Tribology*: Springer US, 2013, pp. 3108-3114.

[154] J. Larsen-Basse and P. L. B. Oxley, "Effect of Strain-Rate Sensitivity on Scale Phenomena in Chip Formation," Macmillan Education UK, 1973, pp. 209-216.

[155] M. F. Ashby, H. Shercliff, and D. Cebon, *Materials: Engineering, Science, Processing and Design*. Cambridge: Cambridge University Press.

[156] J. Theraroz, O. Tuysuz, and J. Schoop, "An improved machining temperature prediction model for aerospace alloys: Effect of cutting edge radius and tool wear," *Journal of Manufacturing Processes,* Jour vol. 133, pp. 1100-1110, 2025, doi: https://doi.org/10.1016/j.jmapro.2024.11.092.

[157] D. Hull, *Introduction to dislocations*. Oxford; New York: Pergamon Press, 1975.

[158] J. P. Hirth, J. Lothe, and T. Mura, "Theory of Dislocations," *Journal of Applied Mechanics,* vol. 50, no. 2, pp. 476-477, 1983.

[159] M. Kothari and L. Anand, "Elasto-viscoplastic constitutive equations for polycrystalline metals: Application to tantalum," *Journal of the Mechanics and Physics of Solids,* Jour vol. 46, no. 1, pp. 51-83, 1998, doi: https://doi.org/10.1016/S0022-5096(97)00037-9.

[160] Y. J. Lee, G. Subhash, and G. Ravichandran, "Constitutive modeling of textured body-centered-cubic (bcc) polycrystals," *International Journal of Plasticity,* Jour vol. 15, no. 6, pp. 625-645, 1999, doi: https://doi.org/10.1016/S0749-6419(99)00004-2.

[161] C. R. Krenn, D. Roundy, J. W. Morris Jr, and L. C. Marvin, "Ideal strengths of bcc metals," *Materials Science and Engineering: A,* Jour vol. 319, pp. 111-114, 2001, doi: 10.1016/s0921-5093(01)00998-4.

[162] J. Gong and A. J. Wilkinson, "Anisotropy in the plastic flow properties of single-crystal α titanium determined from micro-cantilever beams," *Acta Materialia,* Jour vol. 57, no. 19, pp. 5693-5705, 2009, doi: https://doi.org/10.1016/j.actamat.2009.07.064.

[163] S. Nemat-Nasser, W. G. Guo, and J. Y. Cheng, "Mechanical properties and deformation mechanisms of a commercially pure titanium," *Acta Materialia,* Jour vol. 47, no. 13, pp. 3705-3720, 1999, doi: https://doi.org/10.1016/S1359-6454(99)00203-7.

[164] J. R. Mayeur and D. L. McDowell, "A three-dimensional crystal plasticity model for duplex Ti–6Al–4V," *International Journal of Plasticity,* Jour vol. 23, no. 9, pp. 1457-1485, 2007, doi: https://doi.org/10.1016/j.ijplas.2006.11.006.

[165] H. Ben Boubaker, A. Moufki, M. Nouari, P. Laheurte, and A. Tidu, "A crystal plasticity-based model for oblique cutting of face-centered cubic single crystals," *International Journal of Advanced Manufacturing Technology,* Jour vol. 121, no. 1-2, pp. 429-448, 2022, doi: 10.1007/s00170-022-09238-5.

[166] Y. Sun and X. Chen, "Testing and design of wire-laser additively manufactured (WLAM) stainless steel angle section stub columns," *Thin-Walled Structures,* Jour vol. 214, p. 113351, 2025, doi: https://doi.org/10.1016/j.tws.2025.113351.

[167] *RCC-M: Règles de conception et de construction des matériels mécaniques des îlots nucléaires REP*. AFCEN, 2022.

[168] I. Yadroitsev, P. Krakhmalev, I. Yadroitsava, S. Johansson, and I. Smurov, "Energy input effect on morphology and microstructure of selective laser melting single track from metallic powder," *Journal of Materials Processing Technology,* Jour vol. 213, no. 4, pp. 606-613, 2013, doi: https://doi.org/10.1016/j.jmatprotec.2012.11.014.

[169] A. F. Bower, *Applied Mechanics of Solids*, 1st ed. CRC Press, 2009.

[170] H. Chowdhury, K. Naumenko, and H. Altenbach, "Aspects of power law flow rules in crystal plasticity with glide-climb driven hardening and recovery," *International Journal of Mechanical Sciences,* Jour vol. 146-147, pp. 486-496, 2018, doi: 10.1016/j.ijmecsci.2017.06.019.

[171] J. A. Grogan, S. B. Leen, and P. McHugh, "Influence of statistical size effects on the plastic deformation of coronary stents," *Journal of the Mechanical Behavior of Biomedical Materials,* Jour vol. 20, pp. 61-76, 2013, doi: https://doi.org/10.1016/j.jmbbm.2012.12.008.

[172] M. Kavousi, P. McGarry, P. McHugh, and S. Leen, "Geometrical and crystal plasticity modelling: Towards the establishment of a process-structure-property relationship for

additively manufactured 316L struts," *European Journal of Mechanics - A/Solids,* Jour 2023, doi: 10.1016/j.euromechsol.2023.105115.

[173] S. Mahmoody, "Micromechanical modeling of dual-phase steel using a rate-dependent crystal plasticity model," Master of Engineering, Department of Mechanical Engineering, McGill University, 2007.

[174] J. M. Scherer *et al.*, "Tensile and micro-compression behaviour of AISI 316L austenitic stainless steel single crystals at 20 °C and 300 °C: Experiments, modelling and simulations," *Materials Science and Engineering: A,* Jour vol. 900, p. 146471, 2024, doi: https://doi.org/10.1016/j.msea.2024.146471.

[175] F. Careri, S. Imbrogno, D. Umbrello, M. M. Attallah, J. Outeiro, and A. C. Batista, "Machining and heat treatment as post-processing strategies for Ni-superalloys structures fabricated using direct energy deposition," *Journal of Manufacturing Processes,* Jour vol. 61, pp. 236-244, 2021, doi: 10.1016/j.jmapro.2020.11.024.

[176] Y. S. Narayanan, N. Nguyen, and A. Hosseini, "Milling of additively manufactured AlSi10Mg with microstructural porosity defects, finite element modeling and experimental analysis," *Journal of Manufacturing Processes,* Jour vol. 118, pp. 242-260, 2024, doi: https://doi.org/10.1016/j.jmapro.2024.03.051.

[177] H. Ben Boubaker, G. Le-Coz, and A. Moufki, "Experimental and numerical investigations of cutting forces and chip formation during precision cutting of Ti42Nb titanium alloy produced by laser-based powder bed fusion," *The International Journal of Advanced Manufacturing Technology,* Jour 2023, doi: 10.1007/s00170-023-11511-0.